Aalto University
School of Chemical
Engineering

MODERN APPROACHES TO CONTROL OF A MULTIPLE HEARTH FURNACE IN KAOLIN PRODUCTION

José Valentín Gómez Fuentes

Licentiate thesis

Aalto Doctoral Programme in Chemical Engineering

Date: 30.09.2019

Supervisor: Professor Sirkka-Liisa Jämsä-Jounela

Aalto University
School of Chemical Engineering
Chemical and Metallurgical Engineering
Research Group of Process Control and Automation

Aalto University
School of Chemical
Engineering

Aalto University, P.O. BOX 11000, 00076
AALTO
www.aalto.fi

Abstract of licentiate thesis

Author: José Valentín Gómez Fuentes

Title of thesis: Modern Approaches to Control of a Multiple Hearth Furnace in Kaolin Production

Department: Chemical and Metallurgical Engineering

Field of research: Process control

Supervising professor: Professor Sirkka-Liisa Jämsä-Jounela

Thesis advisor(s):

Thesis examiner(s): Emeritus Professor Kauko Leiviskä; Professor Ian K. Craig

Number of pages: 129
Language English

Date of submission for examination: 30.09.2019

Abstract

The aim of this thesis is to improve the overall efficiency of the multiple hearth furnace (MHF) in kaolin calcination by developing control strategies which incorporate machine learning based soft sensors to estimate mineralogy related constraints in the control strategy. The objective of the control strategy is to maximize the capacity of the furnace and minimize energy consumption while maintaining the product quality of the calcined kaolin.

First, the description of the process of interest is given, highlighting the control strategy currently implemented at the calciner studied in this work. Next, the state of the art on control of calcination furnaces is presented and discussed. Then, the description of the mechanistic model of the MHF, which plays a key role in the testing environment, is provided and an analysis of the MHF dynamic behavior based on the industrial and simulated data is presented. The design of the mineralogy-driven control strategy for the multiple hearth furnace and its implementation in the simulation environment are also outlined. The analysis of the results is then presented. Furthermore, the extensive sampling campaign for testing the soft sensors and the control strategy logic of the industrial MHF is reported, and the results are analyzed and discussed. Finally, an introduction to Model Predictive Control (MPC) is presented, the design of the Linear MPC framework for the MHF in kaolin calcination is described and discussed, and future research is outlined.

Keywords: kaolin, calcination, multiple hearth furnace, process control, dynamic modeling, MPC

Acknowledgments

This Licentiate thesis has been written in the Research Group of Process Control and Automation, at Aalto University School of Chemical Engineering during the years 2016 – 2019. This work was part of the STOICISM (The Sustainable Technologies for Calcined Industrial Minerals) supported by the European Commission under the 7th Framework Programme through the grant number 310645, for the "New environmentally friendly approaches to mineral processing". This thesis was also part of and the EIT Raw Materials KAVA project, "Integrated System for Monitoring and Control of Product Quality and Flexible Energy Delivery in Calcination" (MONICALC), grant 15045.

I would like to thank professor Sirkka-Liisa Jämsä-Jounela for the opportunity to work on this thesis in the research group, and particularly in this project. Her supervision and guidance are appreciated. Also, I would like to thank Ph.D. Alexey Zakharov, Ph.D. Alexander Smirnov, and Ph.D. Jukka Kortela for their expertise and support during the course of this work. Gratitude to my coworkers James, Maryam, Teemu, and Hossein for creating an amicable work environment where one could interact and work peacefully.

I very much value the help received from the personnel of IMERYS during this work. Especially to D. Moseley, T. Skuse, and the late J. Hearle.

Sincerely, I would like to express my gratitude to my Family, to my parents Maritza and José Valentín, and my sisters Mari and Mónica, for their never-ending love and support through the years. To my brother in heaven, thank you from the bottom of my heart. To my family and friends, whom I value and keep close to my heart.

"Felicitas est in cordibus nostris"

Otaniemi, 24 September 2019

José Valentín Gómez Fuentes

Table of Contents

List of Symbols

$\mathbb{I}_{\geq a}$	set of integer numbers greater than or equal to $a \in \mathbb{R}$
e_t	White noise
r_t	System setpoint(s) at sampling instant t
u_t	System input(s) at sampling instant t
x_t	System states(s) at sampling instant t
u_t^{mv}	Manipulated variables at sampling instant t
y_t^{sp}	Controlled variable set-point trajectory at sampling instant t
y_t^{cv}	Controlled variables at sampling instant t
$\hat{x}(t+i\|t)$ $\hat{x}_{t+i}$	expected value of $x(t+i)$ with available information at instant t
y_t	System output(s) at sampling instant t
$\mathcal{K}$	A function $\alpha: \mathbb{R}_{\geq 0} \to \mathbb{R}_{\geq 0}$ is a class $\mathcal{K}$ function (or $\alpha \in \mathcal{K}$ for short), if it is continuous, strictly increasing, and $\alpha(0) = 0$
$\mathcal{K}_\infty$	A function $\alpha: \mathbb{R}_{\geq 0} \to \mathbb{R}_{\geq 0}$ is a class $\mathcal{K}_\infty$ function (or $\alpha \in \mathcal{K}_\infty$ for short), if $\alpha \in \mathcal{K}$ and $\alpha(r) \to \infty$ for $r \to \infty$
c_{fm}	Free moisture content, [wt.%]
c_{H2O}	Water content, [wt.%]
F_K	feed rate of kaolin, [%]
F_C	feed rate calcined kaolin, [%]
F_{H4}	Gas flow to the hearth 4, [m^3/h]

F_{H6}	Gas flow to the hearth 6, [m³/h]
F_g	Total gas flow, [m³/h]
m	Mullite content, [wt.%]
p_c	Selling price of calcined kaolin, [€]
p_g	Price of methane gas, [€]
S	Soluble alumina, [wt.%]
T_{Hi}	Temperature of the hearth i, [°C]
Vio	brightness measured as the percentage of light reflected in the violet spectrum

List of Abbreviations

ANN	Artificial Neural Network
ARIMA	Autoregressive Integrated Moving Average
ARMAX	Autoregressive Moving Average Exogenous
ARX	Autoregressive Exogenous
BGFS	Broyden–Fletcher–Goldfarb–Shanno
BR	Bayesian regularization
BtoB	Burner-to-Burner
CV	Controlled variables
DCS	Distributed Control System
DCOM	Distributed Component Object Model
DSC	Differential Scanning Calorimetry
EMPC	Economic Model Predictive Control
FNWMPC	Finite Number of Weights Model Predictive Control
HWM	Hammerstein-Wiener model
ICP-AES	Inductively Coupled Plasma Atomic Emission Spectroscopy
LIMS	Laboratory Information Management System
LM	Levenberg–Marquardt
MHF	Multiple Hearth Furnace
MIMO	Multi input/multi output
MISO	Multi input/single output
MPC	Model Predictive Control
MSE	Mean Squared Error

MV	Manipulated variables
NMPC	Nonlinear Model Predictive Control
OPC	Open Platform Communications
PI	Proportional Integral
PID	Proportional Integral Differential
QDMC	Quadratic Dynamic Matrix Control
QP	Quadratic Programming
RTDB	Real-time database
RTO	Real-time Optimization
SISO	Single Input/Single Output
SOM	Self-Organizing Map
TGA	Thermogravimetric Analysis
XRD	X-Ray Diffraction
XRF	X-Ray Fluorescence

1. Introduction

1.1 Background

The growing complexity of modern processes and factories, increasing global competition, environmental regulation, and decreasing ore quality present important challenges to the operation and control of mineral processing plants. The plants must run efficiently and safely with minimal disturbances to the quality of their products, and operations must respond to constant demand to decrease costs and optimize production.

Currently, mineral processing plants present major challenges with the refinement of ore with a reduced quality. Therefore, improving operations is of utmost importance in the mineral industry, which has shown a remarkable transformation with the incorporation of more automated processes in recent years (World Economic Forum, 2017).

The mineral processing industry is a frontrunner in the notorious advancement of Industry 4.0. This evolution of industry unites advanced technologies such as automation, cyber-physical systems, big data, and robotics to develop smart systems and accomplish improved levels of process optimization (Olivier and Craig, 2017). It is a complete modernization of the way that minerals and metals are produced.

Industrial minerals are naturally formed rocks or minerals that are economically valuable, excluding metallic ores and mineral fuels. Industrial minerals are a specialty submarket of the mining industry. The industrial minerals business face similar challenges as the mineral processing industry. Therefore, automation, use of production “big data”

and the Industry 4.0 concept play a key role in this sector as well, to reach better levels of optimization and efficiency of production.

Clays are one of the most important industrial minerals as they are extensively used in numerous aspects of our society. An important clay is kaolin; it is used in multiple industrial applications including paint, paper, rubber, and refractory items. Some applications require the temperature of kaolin to be raised above 900 °C (Ptáček *et al.*, 2010b), also known as calcination, to enhance its properties and increment the value of the raw material. Calciner furnaces such as rotary kilns and multiple hearth furnaces (MHF) are broadly employed in the industry to calcine kaolin. Generally, the furnaces are highly instrumented and are excellent candidates for efficient control strategy development using Industry 4.0 tools. The calciner control system has a vital role in ensuring uniform product quality while optimizing the furnace capacity and enhancing the furnace energy efficiency for optimal operation.

An essential aspect to improve the mineral processing operations is the incorporation of mineralogy information into the control strategy of the plant. Machine learning methods offer great opportunities to utilize the production "big data" and mineralogy knowledge to be integrated as soft sensors to the plant control strategy (Hodouin, 2011; Leiviskä, 2001). Great improvements have been achieved in the past; researchers have developed expert systems based on the online categorization of ore types using cluster analysis and neural networks (Jämsä-Jounela *et al.*, 1998; Laine *et al.*, 1995).

The multiple hearth furnace is a nonlinear multivariable system that requires an advanced control strategy such as Model Predictive Control (MPC). Several research groups have worked on the design and implementation of model predictive control for rotary kilns and MHF. Stadler et al. (2011) presented a first principle model of a cement kiln and used MPC to stabilize the temperature profile and maximize the production of the kiln. Gouveia et al. (2009) implemented MPC to a

multi-hearth nickel reduction roaster to reduce the variability of the roaster conditions and minimize the energy use.

No advanced controls have been implemented for an MHF in kaolin calcination, however.

1.2 Research problem and the asserted hypothesis

Calciners are complex processes that require precise temperature profile control. Additionally, the operators need mineralogy information to run the calciner efficiently to attain a product with the desired properties. There is a need to develop a mineralogy-driven control strategy to optimize the efficiency of the furnace operation. Mineralogy assays, however, are laborious and require extended time; the number of assays per day is also often limited to minimize costs. Soft sensors have proven to be reliable tools to estimate mineralogy-related information given by the process data, which is otherwise unavailable through direct measurements.

The main motivation for this thesis is to improve the overall efficiency of calcination by developing the advanced control strategy, which incorporates machine learning-based soft sensors and the production mineralogy data.

The main benefits of a mineralogy-driven control strategy are more stable production, improved product quality, and minimization in energy use. In addition, the strategy reduces the need for operators to handle the changes in operating regions and to react to disturbances.

The hypothesis of this thesis is:

The mineralogy-driven control strategy provides an opportunity to improve the operation and performance of the calciner by integrating soft sensors based on mineralogy and process data into the optimization control strategy of the furnace.

To prove the claims of the hypothesis presented above, the following tasks were performed during the research:

Task 1. The mineralogy-driven control strategy for the industrial MHF in kaolin calcination is created. The aim of the strategy is to optimize the capacity and use of energy consumption. The strategy is implemented and tested in the simulation environment with the industrial data.

Task 2. The optimization control strategy is enhanced with the soft sensors. The testing environment (which includes the dynamic model of the MHF, soft sensors for reaction rate, mullite content and soluble alumina, and the control strategy) is programmed and implemented. The testing and data collection campaign are planned and performed at the factory. The impact of the strategy results on the process operation is analyzed.

Task 3. The MPC framework for the MHF in kaolin calcination is designed and tested in the simulation environment. Finally, its performance is evaluated, and further developments are discussed.

1.3 Scope and significance of the thesis

This thesis focuses on the improvement of the overall efficiency of an MHF by incorporating mineralogy information into the control strategy. The enhanced control strategy of the furnace addresses the maximization of the capacity as well as the minimization of energy consumption. The main objective is the development of the advanced control strategy supported by the mullite content and soluble alumina soft sensors based on machine learning algorithms and to be used as constraints for the control strategy. The novelty comes from incorporating the mineralogy-driven soft sensors into the control strategy of the furnace.

The development of the mullite content soft sensor consisted of creating a steady-state mechanistic model based on the information from the

physicochemical phenomena of the kaolin calcination reactions. Additionally, a second mullite content model was designed based on artificial neural networks (ANN). Both models were validated using measurements obtained from the calciner laboratory data. Furthermore, an ANN-based soft sensor to estimate the soluble alumina content in the product was also engineered. This soft sensor was validated using soluble alumina measurements from the final product.

To test the control strategy, a simulation environment was created that includes the mechanistic model of the MHF and soft sensors in conjunction with the control strategy. The testing of the enhanced control strategy was performed and compared with the control strategy of the plant. The simulation results of the enhanced control strategy were analyzed and discussed.

An advanced control strategy such as MPC was conceived and implemented in the simulation environment. The MPC framework would consider the mullite content and soluble alumina estimations as constraints to drive the process and optimize the capacity and energy consumption of the furnace. The results of Linear MPC simulation are presented and discussed. The Nonlinear MPC (NMPC) and Economic MPC (EMPC) frameworks are left outside of the thesis, however, the NMPC and EMPC control strategies and further developments are discussed in the final chapter of the thesis.

1.4 Outline of the thesis

Chapter 2 gives a detailed description of the process of a multiple hearth furnace and its control strategy. The state of the art in the control of calcination furnaces is presented in Chapter 3. Chapter 4 describes the dynamic model of the multiple hearth furnace. Chapter 5 presents the analysis of multiple hearth furnace dynamic behaviors using various data analytics methods. Chapter 6 presents the advanced control strategy designed for the multiple hearth furnace to integrate the mineralogy information of the kaolin calcination process. Furthermore, Chapter 6

discusses the simulation results of the mineralogy-based control strategy, and Chapter 7 presents the testing performed at the plant. Chapter 8 presents the model predictive control strategy for the multiple hearth furnace, and Chapter 9 concludes this work.

1.5 Author's Contribution

The thesis is part of the European FP7 project, "Sustainable Technologies for Calcined Industrial Minerals in Europe" (STOICISM), grant 310645, and the EIT Raw Materials KAVA project, "Integrated System for Monitoring and Control of Product Quality and Flexible Energy Delivery in Calcination" (MONICALC), grant 15045. Professor S.-L. Jämsä-Jounela initially outlined the design of the overall control strategy. J. V. Gomez Fuentes developed, implemented, and validated the mullite content and reaction rate soft sensors for the strategy. J. V. Gomez Fuentes also developed and validated the soft sensors based on Artificial Neural Networks. He also implemented and tested the controllers, performed the simulation tests, and analyzed the results. Dr. A. Smirnov implemented the mechanistic model of the multiple hearth furnace into the simulation environment and provided advice to facilitate the simulations. J. Hearle from IMERYS Ltd. provided in-depth knowledge about the furnace and the data of the real process. Professor S.-L. Jämsä-Jounela made the testing plan at the factory with the help of Dr. B. Sun and J. V. Gomez Fuentes. Dr. B. Sun designed the industrial testing environment with the advice of J. Kortela, who also inspected the instruments at the factory. J. V. Gomez Fuentes analyzed and documented the behavior of the furnace during the testing period. D. Moseley and Dr. T. Skuse from IMERYS Ltd. provided practical knowledge and guidance during the whole testing period. J. V. Gómez Fuentes designed, implemented and tested the Linear MPC for the MHF in kaolin calcination. Finally, J. V. Gómez Fuentes outlined the future research of advanced MPC methods for the MHF in kaolin calcination.

Summary

The objective of this introductory chapter has been to provide the motivation for the study and to present the hypothesis and the main contributions of this research. Initially, an overview of the mineral processing plants and their challenges has been discussed, including the growing interest in incorporating the advancement of Industry 4.0 and big data into the mineral processing industry, focusing on the calcination of Kaolin. Furthermore, the research problem and hypothesis have been outlined while providing the fundamental tasks: (1) the design of the mineralogy-driven control strategy for the MHF; (2) the integration of the mineralogy-based soft sensors into the control strategy and (3) the design, implementation and testing of the MPC framework for the MHF. Finally, the scope and significance of this work have been presented along with the contribution of the author. The following chapters will present the description of the MHF and its control, a brief literature review on the control of calcination furnaces, an analysis of the MHF's dynamic behavior, the design of the control strategy including simulation results and plant testing, and finally, the MPC framework and conclusions.

2. Process description of a multiple hearth furnace

This chapter delivers a general outlook of the kaolin processing, and subsequently it focuses on the calcination process which is the interest of this work.

2.1 Kaolin processing

Kaolin clays are usually mined from open pits since underground mining requires added costs of production that may not be optimal or, in some instances, prohibitive for stable operation. Ore extracted from the deposits needs to be refined because the mineral contains numerous impurities, and the kaolin calcining phase requires high-quality kaolin as raw material for processing. The kaolin is obtained from the pits with the wet processing method, which allows for a more effective extraction compared to dry processing (Thurlow, 2005). Wet processing produces improved color and higher uniformity, and the mineral is fairly free of impurities. The processing of the clay produces sizeable quantities of by-product, including mica, rock, and sand. In Figure 2.1, a basic view of the kaolin extraction, refining, and processing is presented.

The flow of kaolin from the pit to the calcining stage is classified into three main stages:

I. Pit operations
II. Refining processes
III. Drying processes

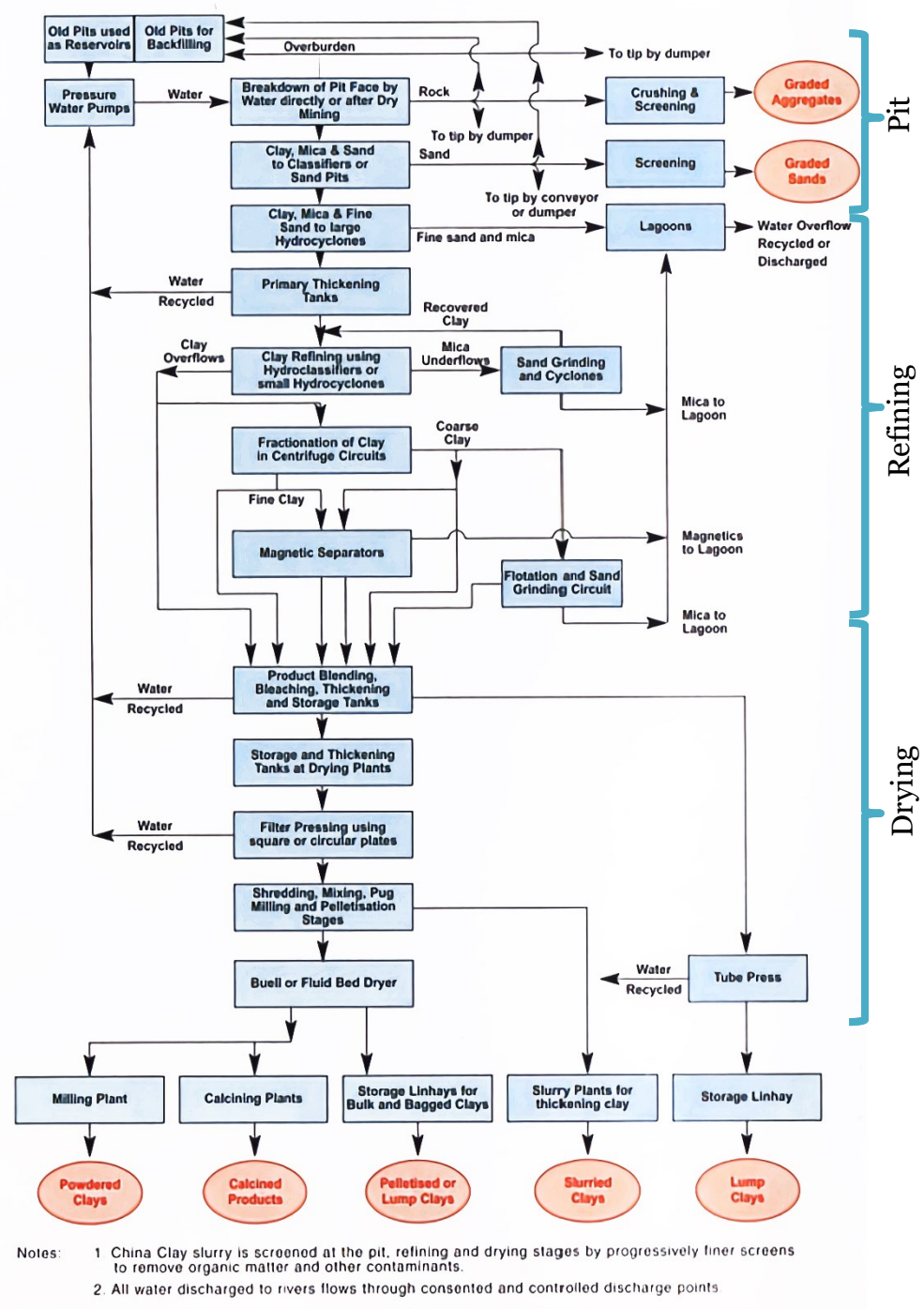

Figure 2.1 Simplified flow diagram of kaolin production (Thurlow, 2005).

2.1.1 Pit operations

Pit operations in an open pit can be separated into five different unit operations:

1. Before the kaolin clay can be extracted from the soil, the overburden is removed.

2. The hard ground is broken down by drilling and blasting. Next, the kaolinized granite can be processed.
3. The kaolinized granite is washed, and stones and sand are removed.
4. The sand removal is done either with bucket wheel classifiers or in large settling pits.
5. Fine sand and coarse mica are separated from the clay. The separation is done by hydrocyclones, which divide the feed roughly into two grades: a particle size of over 50 microns and particles with a diameter of less than 50 microns.

2.1.2 Refining processes

At the refineries, mica, sand, and other impurities contained in the clay suspension are removed to get a pure clay product. The refineries usually feature the following unit operations:

1. Thickening. The clay suspension is pumped continuously to the middle of the tanks, where it settles and is shifted toward the underflow pipe.
2. Mica separation. The material is separated using hydroclassifiers or hydrocyclones. In the hydroclassifiers, a deflocculant is added and a deflocculation process is used. With hydrocyclones, to achieve reasonable tonnage, the clay feed is divided by the number of hydrocyclones.
3. Grinding. The underflow is led through a sand grinding stage to be ground for a short period of time to break the clay stacks but not to break the mica particles.
4. Magnetic separation. Impurities in the refined kaolin such as mica, iron oxides, and tourmaline contain some iron. They can be removed with a powerful electromagnet.
5. Bleaching. This process is used to convert the insoluble iron oxides to iron sulphates using sodium hydrosulphite. The clay first passes through a tall column to remove trapped air and then flows through a pipeline, where the sodium hydrosulphite is added.

2.1.3 Drying process

The refined clay slurry is transported via pipes to a drying plant, where it is initially thickened and then filter pressed to create a cake. The cakes are sliced and fed into a mechanical dryer. The typical mechanical dryers used in the process comprise circular and square filter presses and tube presses.

1. The clay is thickened by sedimentation and then flocculated.
2. The dewatering is continued by filter presses, where the clay is pumped into chambers lined with a tightly woven nylon cloth that passes the water but not the clay particles.
3. The clay can be milled with a pug mill to round the clay particles if necessary.
4. Pelleting. The clay is mixed with paddles, which break down any lumps, and then it is conveyed to a drum. This forms the clay into pellets about 1.3 centimeters long.
5. Drying. In the fluidized bed dryer, slightly pressurized hot air is introduced through a perforated floor in a cylindrical chamber. The fluidized bed combined with cooling provides lower dust levels outside by minimizing steam emissions from the dried product.

After drying, the kaolin can be pulverized to acquire the required particle size. At this stage, the kaolin has been treated until it is ready for particular applications, and it can be sold. However, if higher-quality products are desired, the clay must be calcined to get greater brightness and to lessen the soluble aluminum content.

2.2 Kaolin calcination

Calcination is the process of heating a material below its melting point, thus removing the water contained. This process is one of the most notable ways of enriching the properties, and worth of kaolin. Calcination increases the brightness of the clay, but also intensifies the coarse properties of the material, which can produce handling complications

owing to the abrasiveness of the particles. The range on the variations of the properties is reliant on the duration of calcination, temperature, and the impurities present in the clay. Therefore, depending on the origin of the kaolin, varied qualities of calcined clay will be produced.

The most common methods of kaolin calcination are soak, soft and flash. Soak calcination comprises the exposure of kaolin high temperatures for extended amounts of time to assure that the calcination is fulfilled. Similar to the previous method, soft calcination subjects the clay to high temperatures but only for a limited time in order to minimize the quantity of abrasive particles generated. Finally, flash calcination involves a swift temperature rise, typically between 900 and 1000 °C within a fraction of a second. Calciner furnaces such as rotary kilns and MHF are widely used in industry for the calcination of kaolin and one the general methods used is the soft calcination (Thomas, 2010).

The multiple hearth furnace operated for kaolin calcination, has counter-current gas and solid currents. The furnace studied in this thesis, comprises eight hearths, and eight burners situated in hearths 4 and 6, which burn natural gas to provide the heat necessary to commence the calcination reactions. The amount of airflow, injected to the burners for gas combustion, is calculated based on the stoichiometric ratio. The burners are positioned in a tangential alignment.

Kaolin is delivered to the first hearth placed at the top of the furnace. In the calciner, the material is moved by the metal edges, called blades, which are connected to the rotating rabble arms. The blades are designed to carry the material inward on odd-numbered hearths and outward on even-numbered hearths. The kaolin traveling the odd-numbered hearths falls to the next hearth through a single annulus located around the shaft carrying the rabble arms, while the kaolin in the even-numbered hearths travels outward to descend through the openings at the outside border of the hearth. Figure 2.2 illustrates the internal design of the calciner.

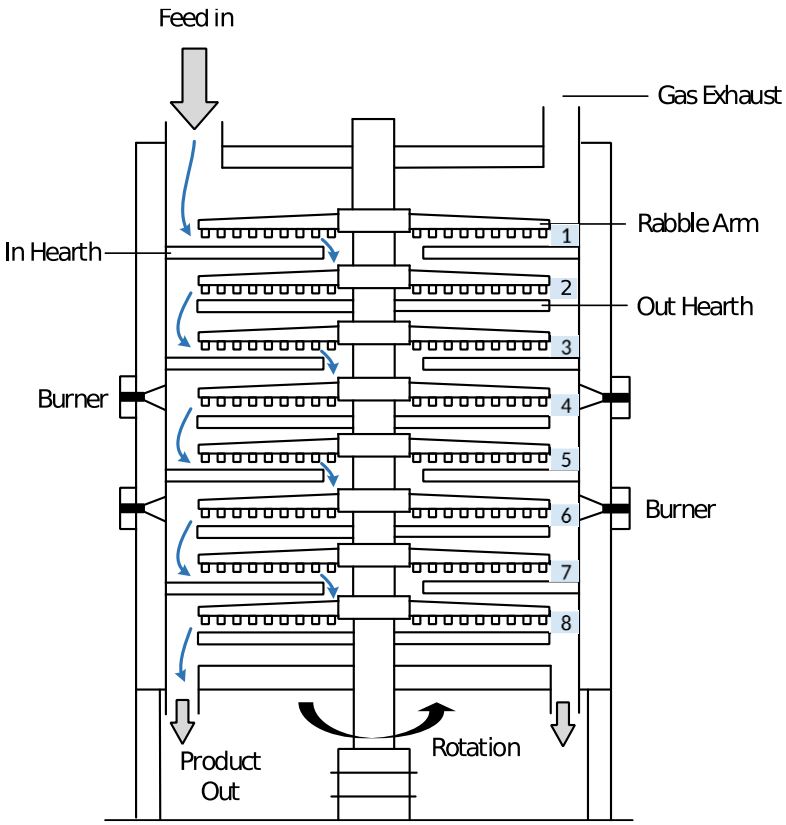

Figure 2.2 Cross-sectional picture of the Herreschoff calciner with direct fire burners. (provided by IMERYS, Ltd).

The temperature of the solid rises as it goes down through the furnace and achieves its maximum in the hearth 6. Initially, kaolinite transforms into metakaolin in the hearths 3, 4, and 5 at a temperature between 400–700 °C (Ptáček *et al.*, 2010a). The metakaolin leaves from the hearth 5 at a temperature of approximately 800 °C, which surges to 1000 °C in the hearth 6, where the reaction of metakaolin to the Al–Si "spinel phase" ensues (Ptáček *et al.*, 2010c). Thus, the main objective of the hearth 6 is to increase the temperature to enable the absorption of aluminum into the silica phase. The temperature control in the hearth 6 is critical to circumvent overheating, which may cause undesired growth of a crystalline material that generates some abrasion problems. The temperature of the solids commences to decline in the hearths 7 and 8, and the product exits from the hearth 8 via two discharge holes at a temperature of 750 °C.

Kaolin consists mainly of the mineral kaolinite; whose chemical formula is $Al_2Si_2O_5(OH)_4$. During calcination, kaolin faces four physicochemical transformations (Ptáček *et al.*, 2011).

1) The vaporization of free moisture occurs (T≤100 °C)

$$H_2O(l) \rightarrow H_2O(g) \qquad (2.1)$$

2) The dehydroxylation reaction ensues, where chemically bound water is separated, and amorphous metakaolin is generated at 450–700 °C (Ptáček *et al.*, 2013).

$$Al_2O_3 \cdot 2SiO_2 \cdot 2H_2O \rightarrow Al_2O_3 \cdot 2SiO_2 + 2H_2O(g) \qquad (2.2)$$

3) The third process is the exothermic re-crystallization of metakaolin to the "spinel phase" product at 925–1050 °C (Ptáček *et al.*, 2010b).

$$2(Al_2O_3 \cdot 2SiO_2) \rightarrow 2Al_2O_3 \cdot 3SiO_2 + SiO_2(amorphous) \qquad (2.3)$$

4) In the fourth physicochemical reaction, the nucleation of the "spinel phase" follows and the solid transforms into mullite at temperatures above 1050 °C (Ptáček *et al.*, 2010b):

$$3(2Al_2O_3 \cdot 3SiO_2) \rightarrow 2(3Al_2O_3 \cdot 2SiO_2) + 5SiO_2 \qquad (2.4)$$

Mullite is a hard solid that can be abrasive to the processing equipment. The desired final product contains minimal mullite and metakaolin. Figure 2.3 illustrates the thermogravimetric analysis (TGA) and differential scanning calorimetry (DSC) graphs of the kaolin calcination reactions.

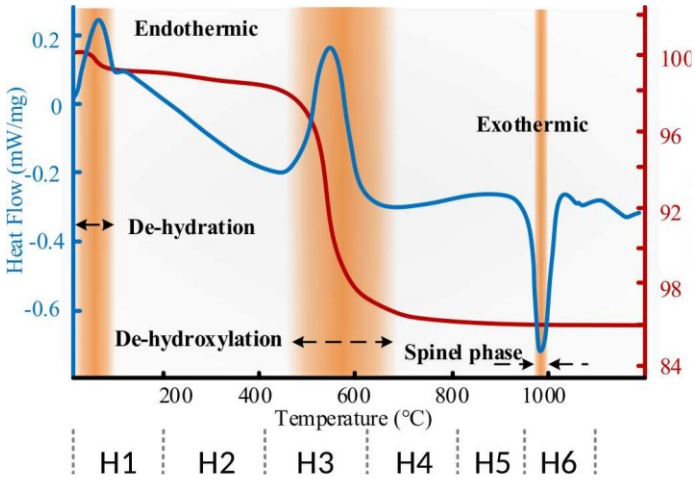

Figure 2.3 Thermogravimetric analysis and differential scanning calorimetry curves for kaolin calcination (provided by IMERYS, Ltd). The corresponding locations in the furnace are indicated.

Equation (2.1) presents the first reaction, which marches forward in the hearths 1 and 2. From the hearth 3 onward, the temperature is suitably high to initiate the second reaction, Equation (2.2), where metakaolin is generated through the dehydroxylation process. The loss of weight due to the dehydroxylation process is shown, between 450 °C and 700 °C, in the TGA red curve of Figure 2.3. The DSC results denote that the dehydroxylation reaction is endothermic, as indicated by the blue line in Figure 2.3. The product of interest, which is the “spinel phase”, is produced in the hearth 6. The spinel formation process is exothermic, which is shown in the temperature range of 925–1050 °C.

2.3 Control strategy of the MHF studied in this thesis

The MHF is a highly instrumented and automated equipment due to the complicated nature of calcination dynamics and its safety requirements. The feed material is conveyed to the furnace by a weigh feeder using a rotary valve. The feed control programmable logic controller manages the feed operation via the rotary valve. The instruments installed at the calciner comprise orifice plate flow meters to measure the gas and air flows, and thermocouples are situated in every hearth of the furnace to monitor the temperature. The hearths 4 and 6 have additional thermocouples positioned in every burner quadrant to accurately monitor the gas temperatures. Two pressure sensors are situated in the central exhaust duct of the calciner.

The control objectives of the MHF in this study are:

1. **The quality**: for a product with added value.
2. **The capacity**: for mass production.

Figure 2.4 illustrates the simplified control logic of the industrial MHF studied in this thesis. The main objective of the control is to increase production and satisfy the quality requirements of the product based on the mineralogy information of the feed material (iron content, brightness, particle size, etc.). In more detail, a Proportional-Integral (PI) system controls the temperatures of the hearths 4 and 6 by regulating the gas flows to the burners and keeping the temperatures within safety limits. The feed rate delimits the maximum gas flow allowed in hearth 4; this constraint avoids the excessive use of gas. An appropriate quantity of air is required to ensure complete gas combustion, which is determined by separate PI controllers. The setpoint for the combustion air flow is computed based on the stoichiometric ratio between oxygen and methane in the combustion reaction.

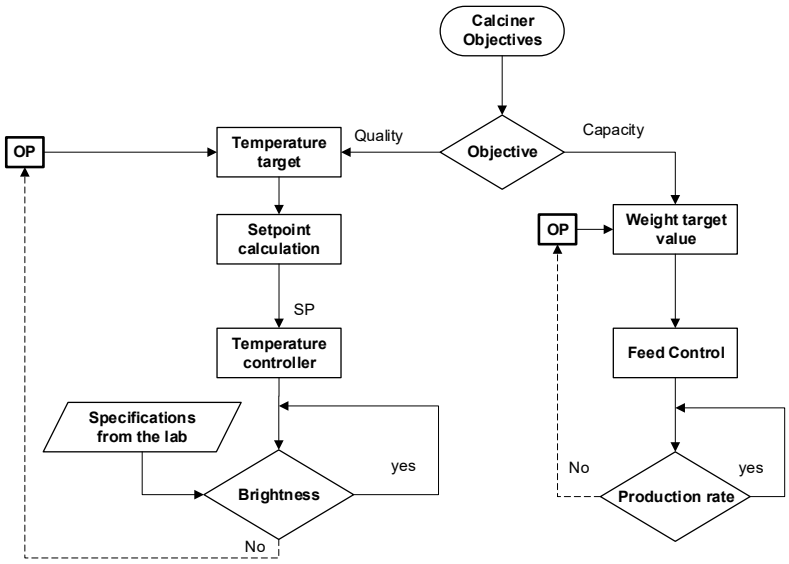

Figure 2.4 Control strategy of the MHF (OP=operator).

Summary

This chapter has introduced a brief description of the processing stages of kaolin, going from its extraction and pit operations to the refining, drying and, finally, the calcination, which is the main process of interest. Additionally, a detailed description of the calcination stages of kaolin occurring in the multiple hearth furnace has been provided, including the vaporization of moisture, dehydroxilation, the “spinel phase” reaction and the formation of mullite. Finally, conventional control of the MHF has been described, emphasizing the main control objectives: (1) the quality and (2) the capacity. The next chapter will deliver a brief literature review on the control of calcination furnaces.

3. State of the art on control of calcination furnaces

This chapter presents the state-of-the-art on the control of calciners. A survey on advanced control methods of rotary kilns and multiple hearth furnaces is presented.

3.1 Control strategies for rotary kilns

3.1.1 Control strategies based on PID controllers

In the study of Ciftci and Kim (1999), the authors designed and tested several control strategies for an industrial rotary calciner with a heat shield around the combustion zone. The calciner is utilized for the endothermic decomposition of trona ore (sodium sesquicarbonate) into crude soda ash (sodium carbonate). Trona ore is fed to the high end of the kiln and advances toward the lower discharge end because of the inclination and rotation of the shell. The heat of the reaction is provided by burning a natural gas and air mixture using a single centerline burner. The mathematical model for the calciner is a set of heat and mass balance equations based on first principles. The model predicts the dynamic response of the calciner with unreacted sodium sesquicarbonate content, and also matches qualitatively with the detected system behavior of the step and sinusoidal disturbances. Kim and Srivastava (1990) presented the necessary details of the mathematical model for this calciner.

In this study, the authors (Ciftci and Kim, 1999) simulated three different Proportional Integral Differential (PID) control schemes to improve calciner product quality. The basic aim behind these schemes was to search for appropriate controlled variables in the calciner/product through which the product quality can be improved by handling the deviations of the input variables. In the first PID closed loop structure, the unreacted sesquicarbonate content of the product is the direct controlled variable and the natural gas flow to the burner is the manipulated variable. The simulations of Ciftci and Kim (1999) revealed that this scheme had several shortcomings, such as long dead and settling times, as well as high initial deviations from the steady-state values. Increasing the sodium sesquicarbonate content of the feed and increasing the feed rate both increase the quantity of reactants entering the calciner. Therefore, more energy should be supplied to the system in both cases. However, increasing the feed rate means that more insoluble material is also entering the system along with the reactants, and that they also should be heated up to the reaction temperature.

In the second PID control scheme, the kiln off-gas temperature is chosen as the controlled variable to increase the product quality and the natural gas flow rate to the burner is the manipulated variable. Taking this controlled variable offers two advantages: (1) The kiln gas has a much smaller retention time compared to the solid; hence, there is less dead time observed in the response of the system, and (2) The gas temperature may easily be measured online with the help of thermocouples. This scheme failed to control the sodium sesquicarbonate concentration of the product satisfactorily. In particular, positive disturbances result in under calcination, whereas over calcination is observed for negative disturbances.

In the last PID scheme, the product temperature is chosen as the controlled variable and the natural gas flow rate to the burner is the manipulated variable. With this controlled variable, the closed loop will exhibit a long dead time because of the long retention time of solids. However, this control scheme was successful in eliminating the problem

of over and under calcination. Moreover, this scheme has an economical advantage over the first scheme as the product temperature can be easily measured online with the help of thermocouples.

The first and last PID schemes are quite successful in maintaining the specific product quality. However, both these schemes have a long dead time because these schemes rely on product output. It is worth noticing that the third scheme is a more cost-effective scheme than the first one. Subsequent to the above experiments, the authors of the study (Ciftci and Kim, 1999) simulated a feedforward control strategy by deriving a first order input/output model of the calciner, with the controlled variable chosen as the sodium sesquicarbonate content of the product and the natural gas flow rate to the burner as the manipulated variable. The reported results confirm that the feedforward control scheme was successful in handling disturbances in the feed ore rate.

3.1.2 Advanced Control of a Rotary Dryer

In a study by Yliniemi et al. (1998), two types of hybrid intelligent control systems were designed for a rotary dryer. The process was a pilot rotary dryer with direct air-heated and concurrent flows, which was designed and constructed at the University of Oulu. A screw conveyor transports the calcite (more than 98% $CaCO_3$) from a silo to a rotating drum to be dried. The drum length is 3 m with a diameter of 0.5 m. A blower supplies the drying air which is later heated in the burning chamber using propane gas as fuel. Finally, the dried calcite is transported back to the silo via a belt conveyor where it is wetted once more.

The authors' first control approach was the development of a fuzzy logic controller for the rotary dryer. The aim was to combine the controller with a PI controller and to facilitate the rotary dryer control by applying the operator's expert knowledge. The controlled variable is the solid material output moisture. The main manipulated variable is the drying air input temperature, which is correlated to the fuel flow. An auxiliary

manipulated variable is the solids velocity, which correlates to the rotation speed of the screw conveyor. The solids input moisture and the feed flow are the main disturbances. The fuzzy logic controller provides the setpoint information of the drying air input temperature to the PI controller. The fuzzy logic controller used trapezoidal membership functions for the three input and one output variables. The controller operates for the conditions when the solids input moisture is in the range 2.5–4 wt.% and the desired quantity of the solids output moisture is 0.1 wt.%. The fuzzy logic controller regulates the solids output moisture quite well when the input moisture disturbances are introduced to the system.

The second control approach involves the development of a neural network controller. The purpose of the controller is to provide the setpoint values of the feed flow and the drying air input temperature to the PI controllers which control the fuel flow valve and the screw conveyor rotation speed. The primary manipulated variable is the drying air input temperature. The feed flow is the secondary manipulated variable while the main disturbance variable is the solids input moisture. The neural network controller uses an inverse process model, which makes it a direct inverse controller. The architecture of the neural network includes: the input layer with 17 variables, two hidden layers, and one output layer. The input variables of the neural network controller were the present and four past values of the solids input moisture, present and five past values of the solids output moisture, present and three past values of the solid's velocity, and present and past value of the drying air input temperature. The simulation results of the neural network controller were promising for controlling the drying process. The neural network controller was implemented to control the pilot plant dryer due to its promising performance.

3.1.3 Intelligent systems control of rotary kilns

Järvensivu et al. (2001) developed an intelligent control system for the industrial lime kiln at the Wisaforest pulp mill. The lime kiln is a large cylindrical oven divided into four zones based on the temperature profile of the flue gas and the solid materials in the kiln. These four zones are: wet mud drying, mud powder heating to the reaction temperature,

calcium carbonate calcination into calcium oxide, and fine powder agglomeration into granules.

The control system is divided into three hierarchically organized levels. The aim of the highest level in the hierarchy is to optimize the kiln process operation based on the kiln energy efficiency, lime quality, and environmental safety by determining the best target values for the stabilizing level controllers. The next level in the control structure has been designed to guarantee steady operation of the kiln process. In practice, this is accomplished by proper adjustments made in the setpoints of the basic-level control loops, which are implemented in the distributed control system (DCS). The lowest level of the system includes a bi-directional interface to the low-level systems via a connection to the real-time database (RTDB) of the information system.

The high-level control of the kiln process is executed by the inter-related units of the feedforward control models, stabilizing controllers and constraints handling. The controlled variables of the high-level control system are excess oxygen, cold-end temperature and hot-end temperature. The manipulated variables are the draft fan speed, sawdust feed rate and kiln rotational speed. The constraint variables are lime mud drier temperature, cold-end pressure, and total reduced sulfur emissions. The models used for the feedforward control include a multiple linear regression (MLR) and several backpropagation neural network models. The stabilizing control features fuzzy logic principles in its design, and structured natural language rules jointly with procedural reasoning are used to detect the lime mud drier temperature for each new measurement. Also, the controller based on a PI-type linguistic equation provides improved elements for managing nonlinearity and disturbances (Juuso and Leiviskä, 1992).

The main measurable advantage of the intelligent control system was the near 7% decrease in energy consumption contrasted with the manual operation. Furthermore, the control system improved the burnt lime quality. From the environmental viewpoint, the main benefits were a

decrease of 10% in total reduced sulfur emissions and a decrease of near 50% in the number of high emission events.

Shah et al. (2019) developed conventional and artificial intelligence models for operational guidance and control for a rotary kiln in sponge iron production The aim was to benchmark the predictive capabilities of a combination of artificial intelligence and conventional models and pressure control in the real-life plant environment with a focus on minimizing accretion and improving quality control. The rotary kiln is a counter current furnace. The feed material (iron ore, coal, and dolomite) is introduced from one side of the rotary kiln, and the combustion coal is burned from the other side. The kiln is moderately inclined to allow the flow of material in a forward direction. Incomplete combustion of coal is backed by the air propelled through the primary air blower and root blower from the burning side. Additionally, a few secondary air blowers are appropriately located along the entire perimeter of the kiln.

The models of the kiln were developed using MLR, ANN and extreme learning machine methods. Extreme learning machine is a learning algorithm for single-hidden layer feedforward neural networks which selects hidden nodes at random while analytically determining the output weights of the network (Huang *et al.*, 2006). The variables used to develop the conventional and artificial intelligence models were the inlet and outlet pressures, primary and secondary air flow rates, ore and coal flow rate from the feed side, coal burning rate from the burning side, and temperature measured by ten thermocouples through the length of the furnace. The authors recommended utilizing extreme learning machine, in preference to ANN and MLR when the size of data is suitable; otherwise MLR is should be used for short time intervals (over 10 days). The models developed by the authors have been implemented and have shown improvements in accretion control and quality control.

3.1.4 Model predictive control schemes for rotary kilns

In Zanovello and Budman's lime kiln application, it was desired to control the cold and front end temperatures at specific values while

allowing the oxygen level to vary between two pre-specified limits (Zanovello and Budman, 1999). The two manipulated variables were the flow of air through the kiln induced by a pump located at the cold end and the flowrate of natural gas used for combustion. The principal disturbance to the process was the change of the lime feed located at the cold end section of the kiln. The transfer functions used for model prediction were identified from a pulp mill located in Prince George, BC, Canada.

In the control system, infeasibilities in the presence of constraints and issues of sensitivity to model mismatch occurred during normal operation of the kiln and had a clear impact on the performance of the control system. Constraints were imposed on manipulated, controlled or associated variables. When dealing with softening of constraints, a basic question to answer was: what degree of deviation outside the constraints could be allowed for each one of the controlled or constrained variables during process operation?

A predictive control algorithm with soft constraints is presented by the authors for the lime kiln. The technique, finite number of weights model predictive control (FNWMPC) is based on the calculation of suitable weights in the objective function of the predictive control problem when the constraints are disobeyed. In their results, the calculation time is found to be minimal and the convergence to a global optimum is assured. Finally, FNWMPC was benchmarked to the FE (Feher and Erickson, 1993) and the quadratic dynamic matrix control (QDMC) algorithms. In both benchmarks, the FNWMPC was evidenced to be more effective in allocating the amount of error among the output variables.

In Allison and Ball, a cascaded MPC strategy was implemented on a rotary lime kiln to meet the following objectives (Allison and Ball, 2004):

- Regulate the product temperature to maximize capacity while maintaining the quality of the lime.

- Minimize the use of excess oxygen to reduce combustion gas velocity and dust recycle.
- Minimize the cold-end temperature to reduce energy consumption.
- Maintain the stability of the process over a wide range of conditions while responding to disturbances.

The cascaded MPC consisted of two loops. The internal loop is a 2×2 MPC that controls the cold-end temperature and excess oxygen with manipulated variables: fuel flow rate and the induction draft fan speed. The external loop is a 2×1 MPC that controls the hot-end temperature while minimizing the excess oxygen using the following manipulated variables: the cold-end temperature and excess oxygen setpoints. Both the excess oxygen and the cold-end temperature setpoints are instantly manipulated after a setpoint change or disturbance in the hot-end temperature. Finally, the oxygen setpoint is directed back to its target value after a change in the cold end temperature setpoint. To determine the model of the plant, a preliminary internal loop model was identified from bump test data. The external loop model was identified with a similar procedure. Finally, the preliminary models were refined by closed-loop experiments to improve the performance. The cascaded MPC can attain improved control and better economic performance than conventional methods.

In a cement plant the production of clinker is one of the key processes to optimize in order to produce high quality cement. Stadler et al. (2011) presented an MPC controller for a rotary cement kiln, which was installed on *cpmPlus Expert Optimizer* a commercial platform for advanced process control and optimization developed by ABB. The clinker production process can be generally divided into four consecutive zones: preheating, calcining, sintering, and cooling. These zones were modeled and integrated into the platform as separate submodels. Each submodel of the cement kiln was designed as a mixed logic dynamic system (Bemporad and Morari, 1999). The main objective of the controller was to maximize the capacity of the kiln; therefore, the authors considered

the linearization of the nonlinear expressions to implement the model in the controller platform. The main controlled variables were the temperature in the burning zone, temperature at the back end, and oxygen after combustion. The main manipulated variables were the feed rate and specific energy input. The controller was implemented on a cement plant located in Switzerland (Holcim Ltd., Plant Siggenthal) and it has shown highly satisfactory performance. The MPC presented by the authors has reduced the variability of the controlled and manipulated variables.

A generalized predictive controller was designed by Hernandez, et al. to control the clinkerization temperature in a cement rotary kiln. The process studied by the authors was a cement rotary kiln located in Peru (Cementos Lima) (Salcedo Hernandez *et al.*, 2018). This furnace consists of a cylindrical steel tube lined with refractory material, with a length of 120 m, a diameter of 4 m, a slope with respect to the horizontal plane of 5%, and rotation at a speed of up to 3 RPM. To obtain the mathematical model that describes the dynamics of the clinkerization temperature in the combustion zone of the rotary kiln, an experiment with a step signal was initially developed to determine the order and parameters of the model of said process. Next, these results were used in the design of a more informative experiment, where the flow of fuel follows a binary signal. Evaluation work was completed on different model structures, such as autoregressive moving average exogenous (ARMAX), autoregressive exogenous (ARX), output-error and Box-Jenkins were used, and the parameters of these structures were estimated to determine the model that best fits the data obtained experimentally. The ARMAX model presented the minimum prediction error compared to the other models. Next, the ARMAX model was converted into an autoregressive integrated moving average exogenous model, which was used to predict the dynamics of clinkerization temperature. For the generalized predictive controller, the burner fuel flow was considered the manipulated variable and the temperature in the oven combustion zone was considered the controlled variable. In addition, the furnace is affected by different disturbances, including the variation in the feed

material, the flow and the temperature of the air. The generalized predictive controller was compared to a PID control scheme. The comparative results of the simulations showed that the best performance in the control of clinkerization temperature is obtained when the GPC controller is implemented, which guarantees the production of consistent high-quality cement with lower fuel consumption.

3.2 Control of the multiple hearth furnace

One of the areas where the MHF has been employed is the selective reduction of nickel. The MHF considered by Ramírez, et al. is installed at the Nicaro plant in Cuba (Ramírez *et al.*, 2004). Wet concentrates are charged into the upper hearth. A central rotating shaft drives the rabble arms, guides the concentrates charge, and transfers it via drop holes to the following lower hearth. The gas phase moves from lower to upper hearths, while the solid phase moves in the opposite direction. The dried ore is combined with fuel oil as a reductant, before being introduced to the roaster, where it is cooked under reducing conditions at 700–800 °C. The feed material is likewise heated by the hot reducing gas ($CO + H_2$) generated by the combustion of the fuel oil in an undersupplied air environment in nine combustion chambers located along each roaster. Both CO and H_2 are completely burned by the addition of air at the hearths 4 and 6 to recover the maximum of the chemical heat value of the reducing gases before being released to the atmosphere. This postcombustion process decreases fuel intake by 50%.

To achieve the control objectives, a fuzzy logic controller was designed and implemented (Ramírez *et al.*, 2004). The basic motivation for using this advanced controller in comparison to the tradition PID controllers came from the existing nonlinear relationship between the temperature in the hearth 4 and the air flow at a steady-state. In their approach, a controller is designed by considering the process as a multi input/multi output (MIMO) system, which controls the temperature in the combustion process.

The fuzzy controller to optimize nickel recovery in the MHF is composed of five input variables: the error and change of the error of temperatures in the hearths 4 and 6, and the specific fuel consumption while the output variables were the change in airflow to the hearths 4 and 6, fuel oil flow to combustion chambers, and ore flow fed to the roaster. A number of field tests were performed at the plant. During the tests the process was subjected to different disturbances and in all the cases, the controller maintained the temperature of the hearths 4 and 6 in the prescribed range.

Rotary kilns or multiple hearth roasters are commonly used for the extraction of vanadium from steelworks slag. The slag is roasted under alkaline conditions, usually using $NaCl$ and/or Na_2CO_3 as additives. Assuming homogenous gas and bulk layers in every floor, a first principles model of the vanadium roast process in a multiple hearth furnace was derived in Voglauer and Jörgl (2004). This development yielded a nonlinear state-space model for calculating the mean values for mass, temperature and concentrations. In the study, the process model order was observed to be quite high due to several decisive states on every floor of the MHF. Model order reduction was then carried out by assuming a lower order transfer function structure.

From the control-theoretic viewpoint, the maintenance of an oxidizing atmosphere during roasting is essential for maximum efficiency in the conversion of the vanadium. Furthermore, accurate temperature control in the roasting units is a necessity for reasonable recovery of the vanadium and to avoid any undesirable process behavior, such as hearth buildup (Geyrhofer *et al.*, 2003). To achieve the aforementioned objectives, the overall controller design is divided into four parts (Voglauer *et al.*, 2004). The main control loops were the following:

1. pH-control: The pH value of the roasted bulk is controlled by the mass flows of $NaCl$ and/or Na_2CO_3.
2. c- control: Stationary control of a key component concentration.

3. T-control: The temperature of the individual floors is controlled by burner gas flow.
4. $Overhead$-control: The overhead controller provides the reference values to the above control loops.

The main aim of designing the temperature controllers is to maintain a desired temperature profile over the furnace by regulating the temperatures of the individual furnace floors. This usually gives a strongly coupled multivariable system. In the preliminary work of Geyrhofer et al., (2003), the parameters of the controllers were chosen by optimizing a quadratic cost function, plus the tracking error and the efforts of the weighted control.

For the pH-control, the time delay caused by the process itself and consecutive offline analysis of the pH level increased significantly the time lag, causing a total dead time, therefore a smith predictor control design was implemented. In this predictive control framework, the information of the process model and precise data of the total dead time are needed to obtain an estimate of the pH value. The sampled and delayed pH variables are used to minimize modeling errors and the effect of unaccounted disturbances. Further enhancements in the controlled behavior can be attained by feedforward controllers.

An MPC technique was used as an advanced process control method to control and optimize a set of nickel reduction roasters located at Votarantim Metais Niquel (VMN) in Niquelandia, Gioas State, Brazil (Gouveia *et al.*, 2009). The physical structural properties of the Herreschoff roaster include 12 hearths. The reported total transit time of the roaster is approximately three hours. Each of the lower hearths has a pair of burners (12 in total) in which heavy fuel oil is burned with sub-stochiometric conditions. This generates an atmosphere rich in carbon monoxide which, together with temperatures in the range 600 to 800 °C, causes the reduction of the oxide ore to the metalized form.

The main control objectives are (1) improve the stability of roaster temperatures; (2) reduce fuel oil consumption per ton of feed; (3) increase nickel metallization levels in the roaster product stream. Indeed, the regulation of a hearth temperature is achieved by adjustment of the firing rate (oil flow) of the associated burner. However, each hearth temperature is also strongly affected by the firing rate of the adjacent burners, by the ore feed rate, and the secondary air flow.

The basic automation of the VMN roasters is provided by a network of Allen-Bradley PLCs, with a supervisory SCADA layer from Wonderware InTouch software. The predictive model used in the Connoisseur multi-variable controller has a straightforward linear time-series format. In order to achieve the control in real-time, the dynamic process model is deployed within a constrained model-predictive control structure, where the control moves are calculated such that the value of a quadratic cost function is minimized subject to linear inequality constraints. This is known as the Quadratic Program (QP) algorithm. The cost function is composed of the following variables: square of the predicted controlled variables (CV) errors over the prediction horizon, square of the incremental manipulated variables (MV) moves over the control horizon, and the square of the predicted MV deviations from target over the control horizon. The results reported in Gouveia et al., (2009) confirm the superiority of the QP controller increases nickel recovery and reduces oil consumption compared with the conventional control.

Summary

A brief literature review of the calcination processes has been presented in this chapter. The most significant control strategies of rotary kilns have been described, focusing on PID, artificial intelligence and MPC. Additionally, several control strategies for multiple hearth furnaces have been summarized; these strategies have used different methods such as fuzzy logic and MPC. The following chapter will thoroughly describe the dynamic model of the MHF, which is the main focus of this research.

4. Dynamic model of the multiple hearth furnace

This Chapter presents the dynamic model of the MHF considered in this research for control testing, for more details of the model please refer to (Eskelinen *et al.*, 2015, 2016). In the research of Eskelinen, a first principles model of the MHF was created. In the work, the MHF was separated in six parts: the solid bed, gas phase, walls, central shaft, cooling air, and the rabble arms. The MHF modeled by Eskelinen, consists of eight hearths and it is designed with a counter-current solid and gas flows as described in Chapter 2. The calcination process needs vast amounts of heat, which is provided to the furnace through eight methane burners allocated in the hearths 4 and 6.

A few assumptions have been considered to develop the model. First, the solid bed on the hearths are divided into five (hearths 1 and 2) or four (hearths 3 to 8) annular volumes based on the furnace rabble arm configuration. Second, these volumes are designed to be identical in magnitude regarding the mass content and the radial direction. As a third consideration, the mixing model assumes that one rotation of the shaft scatters the contents of a volume between the initial and its neighbor volumes (one is the subsequent and the other is the previous). Finally, after one rotation, the following equation defines the solid mass distribution:

$$m_{t+1}^{j} = D_j \cdot \left(m_t^j - R_{r,t}^j\right) + m_{feed,t}^j \tag{4.1}$$

where $m_{feed,t}^{j}$ and $R_{r,t}^{j}$ represent the hearth feed and the solid phase mass loss in the hearth j. D is the mass movement matrix, which defines the distribution of each partition m_t^j after one rotation of the central shaft in the hearth j. Additionally, the column i of the matrix designates the distribution of volume i among the volumes of the hearth.

The feed to the hearth is calculated as the exiting volume from the previous hearth as follows:

$$m_{feed,t}^{j} = \left(1 - \sum D_{j-1}^{K}\right)\left(m_t^{j-1,K} - R_{r,t}^{j-1,K}\right) \tag{4.2}$$

where K is the exiting volume of hearth $j-1$ and D_{j-1}^{K} is the Kth column of matrix D_{j-1} . Then, the definition of the solid bed movement matrix for the hearth 1 is as follows:

$$D_1 = \begin{bmatrix} 1-a_1 & a_1 & 0 & 0 & 0 \\ a_1-\alpha & 1-2\,a_1+\alpha & a_1 & 0 & 0 \\ 0 & a_1-\alpha & 1-2\,a_1+\alpha & a_1 & 0 \\ 0 & 0 & a_1-\alpha & 1-2\,a_1 & a_1 \\ 0 & 0 & 0 & a_1 & 1-a_1 \end{bmatrix} \tag{4.3}$$

The parameter α defines the net advancing flow through a hearth, this corresponds to the feed rate minus the mass loss due to the dehydroxylation reactions and evaporation. a_1 represents the upper diagonal matrix elements and indicates the flow from the current to the next volume. Therefore, the lower diagonal matrix elements $(a_1 - \alpha)$ denotes the difference of the full forward and the net forward flows.

The mass balance of the gas phase is determined as:

$$\dot{n}_{i,in} - \dot{n}_{i,out} - R_i = 0 \tag{4.4}$$

where $n_{i,out}$ indicates the number of moles of component i exiting a volume, R_i is the component i mass difference due to the reactions, and $n_{i,in}$, denotes the arriving moles of component i, calculated as follows:

$$n_{i,in}^{j} = c_i^{j+1} F^j \tag{4.5}$$

F_j is the gas flow circulating through the hearth, c_i^{j+1} is the component i concentration in the preceding volume, and the volume number is j.

For each hearth with different temperature, the real volumetric gas flow F_{real}, can be obtained based on the ideal gas law as:

$$F_{real} = F_{NTP} \frac{T_{real}}{T_{NTP}} \tag{4.6}$$

where F_{NTP} is the volumetric flow estimated from the atmospheric pressure and temperature.

The model also considers energy balances for the walls, the central shaft, gas phase, cooling air, solid bed, and for the rabble arms:

$$\dot{Q}_{gas,in} - \dot{Q}_{gas,out} + \dot{Q}_{combustion} + \dot{Q}_{gs} + \dot{Q}_{gw} + \dot{Q}_{gshaft} + \dot{Q}_{garms} = 0 \tag{4.7}$$

where $Q_{gas,in}$ and $Q_{gas,out}$ symbolize the heat of the inward and the outward gas flows, $Q_{combustion}$ is the heat liberated by the combustion, and the final four terms in the left side of the equation, designate the heat exchange of the gas phase with the solid, walls, central shaft and the arms.

The combustion energy is calculated as follows:

$$\dot{Q}_{combustion} = b_i \dot{n}_{methane} \Delta H_{combust} \tag{4.8}$$

where b_i denotes the combustion ratio, $n_{methane}$ signifies the methane flow rate, and $\Delta H_{combust}$ represents the combustion enthalpy of methane.

Between the gas and solid phases there is heat transfer, denoted as $\dot{Q}_{gs}$, which presents itself through radiation and convection as shown in the following equation:

$$\dot{Q}_{gs} = \sigma X_s A_{gs} \varepsilon_s \varepsilon_g \left(T_g^4 - T_s^4\right) + h_{cgs} X_s A_{gs} \left(T_g - T_s\right) \tag{4.9}$$

where A_{gs} denotes the area of the hearth floor, σ represents the Stefan-Boltzmann constant. The solid and gas emissivities are represented as ε_s and ε_g respectively, and the heat transfer coefficient as h_{cgs}. T_g and T_s symbolize the temperatures of the gas and the solid phases respectively. X_s indicates a surface view factor.

Heat transfer among the inner walls and the gas phase $\dot{Q}_{gw}$ takes place by convection and radiation:

$$\dot{Q}_{gw} = \sigma A_{gw} \frac{(\varepsilon_w + 1)}{2} \varepsilon_g \left(T_g^4 - T_w^4\right) + h_{cgw} A_{gw} \left(T_g - T_w\right) \tag{4.10}$$

where A_{gw} signifies the walls area, ε_w and ε_g represent the emissivities of the walls and the gas phase, T_g and T_w indicate the temperatures of the gas and walls respectively, and h_{cgw} designate the heat transfer coefficient.

The heat flux between the central shaft and the gas phase is denoted as $\dot{Q}_{gshaft}$, and the flux between the rabble arms and the gas phase is symbolized as $\dot{Q}_{garms}$. These terms comprise the radiative and the convective heat transfer terms respectively, which are described as follows:

$$\begin{aligned} \dot{Q}_{gshaft} = {} & \sigma Z A_{gshaft} \varepsilon_{shaft} \varepsilon_g \left(T_{gas}^4 - T_{shaft}^4\right) \\ & + h_{cgshaft} Z A_{gshaft} \left(T_{gas} - T_{shaft}\right) \end{aligned} \tag{4.11}$$

$$\begin{aligned} \dot{Q}_{garms} = {} & \sigma A_{garms} \varepsilon_{arms} \varepsilon_g \left(T_{gas}^4 - T_{arms}^4\right) \\ & + h_{cgarms} A_{garms} \left(T_{gas} - T_{arms}\right) \end{aligned} \tag{4.12}$$

where A_{gshaft} and A_{garms} signify the areas of the central shaft and the arms respectively, ε_{shaft}, ε_{arms} and ε_g represent the respective emissivities of the shaft, the arms and the gas. T_{shaft}, T_{arms} and T_g

symbolize the temperatures of the model sections respectively with the heat transfer coefficients h_{gshaft} and h_{arms}. Finally, Z is a constant which defines the insulation of the central shaft.

The energy balance equation for the walls is shown as follows:

$$\frac{\partial Q_w}{\partial t} = \dot{Q}_{wg} - \dot{Q}_{ws} - \dot{Q}_{wa} \tag{4.13}$$

where Q_w denotes the heat accumulated in the walls, and $\dot{Q}_{wg}$ and $\dot{Q}_{wa}$ represent the heat transfer between the walls and the gas, and the walls and the ambient air.

The radiative heat flux is obtained as follows:

$$\dot{Q}_{ws} = \sigma X_s A_{sw} \varepsilon_{sw} \left(T_w^4 - T_s^4\right) \tag{4.14}$$

where X_s and A_{sw} indicate the shape factor of the solid surface and the area of the hearth floor respectively. The emissivity among the solid bed and the walls is represented as ε_{sw}.

The next equation calculates the heat transfer between the outer wall and the ambient air:

$$\dot{Q}_{wa} = h_{cwa} A_{wa} (T_{ambient} - T_{outer\ wall}) \tag{4.15}$$

where A_{wa} denotes the surface of the external layer of the furnace wall. $T_{outer\ wall}$ and $T_{ambient}$ represent the respective temperatures of the external wall layer and the ambient air. Finally, h_{cwa} indicates the heat transfer coefficient. In order to calculate the temperature profile, the furnace wall is partitioned into eight segments corresponding to the distribution of the hearths.

The equations which describe the heat transfer in the central shaft and the rabble arms are respectively as follows:

$$\frac{\partial Q_{shaft}}{\partial t} = \dot{Q}_{gshaft} - \dot{Q}_{shaft,cool} \tag{4.16}$$

$$\frac{\partial Q_{arms}}{\partial t} = \dot{Q}_{garms} - \dot{Q}_{arms,cool} \tag{4.17}$$

where Q_{gshaft} and Q_{garms} denote the heat exchange among the central shaft and gas phase, and the arms and gas phase respectively.

The heat transfer between cooling air and the central shaft and the rabble arms correspondingly are obtained:

$$\begin{aligned}\dot{Q}_{shaft,cool} = \sigma A_{shaft,cool}\varepsilon_{shaft}\ \ (T_{shaft}^4 - T_{cool}^4) \\ + h_{Cshaft,cool}A_{shaft,cool}(T_{shaft} - T_{cool})\end{aligned} \tag{4.18}$$

$$\begin{aligned}\dot{Q}_{arms,cool} = \sigma A_{arms,cool}\varepsilon_{arms}(T_{arms}^4 - T_{cool}^4) \\ + h_{Carms,cool}A_{Carms,cool}(T_{arms} - T_{cool})\end{aligned} \tag{4.19}$$

where $A_{shaft,cool}$ and $A_{arms,cool}$ denote the external areas of the central shaft and the arms, $\varepsilon_{shaft}$and ε_{arms} represent the emissivities of the shaft and the arms, while T_{shaft}, T_{arms} and T_{cool} indicate the temperatures of the model sections respectively. Finally, $h_{Cshaft,cool}$ and $h_{Carms,cool}$ symbolize the heat transfer coefficients.

The energy balance of the cooling air is represented as follows:

$$\frac{\partial Q_{cooling\ air}}{\partial t} = \dot{Q}_{cooling\ air,in} + \dot{Q}_{arms,cool} + \dot{Q}_{shaft,cool} - \dot{Q}_{cooling\ air,out} \tag{4.20}$$

where $\dot{Q}_{cooling\ air,in}$ and $\dot{Q}_{cooling\ air,out}$ denote the heat of the inward and outward cooling air, while $\dot{Q}_{shaft,cool}$ and $\dot{Q}_{arms,cool}$ signify the respective heat exchange regarding the cooling area with the central shaft and with the arms.

The final heat equation of the solid phase energy balance is obtained as follows:

$$\frac{\partial Q}{\partial t} = \dot{Q}_{mass,in} - \dot{Q}_{mass,out} - \dot{Q}_{reactions} - \dot{Q}_{evaporation} + \dot{Q}_{sw} + \dot{Q}_{sg} \qquad (4.21)$$

where Q represents the solid phase heat of a volume, $\dot{Q}_{mass,in}$ and $\dot{Q}_{mass,out}$ designate the inward and outward solid phase heat flow of the volume. $\dot{Q}_{reactions}$ describes the heat of the chemical reactions ensuing in the solid phase and $\dot{Q}_{evaporation}$ is the free water evaporation, while the final two terms denote the heat exchange regarding the solid bed and the walls, and the solid bed and the gas phase. Finally, the heat in each solid bed partition can be calculated as follows:

$$Q_{t+1}^{j,k} = D_j \cdot Q_t^{j,k} + Q_{feed,t} \qquad (4.22)$$

The solution for the MHF model consists of the following steps. Initially, the reaction rates are determined using the reaction kinetics retrieved from experimental data and previous studies. Next, the solid mass distribution is computed according to the mixing model. Then, the mass and energy balances of the gas phase are solved using the temperature-dependent model parameters. In the next step, the energy balance calculations for the central shaft, walls, cooling air, and the rabble arms are performed. Finally, the mixing model is applied to solve the energy balance of the solid phase, which requires the heat fluxes estimated in the previous steps. A summary of the model solution cycle is presented in Figure 4.1, which illustrates how the model states and computable parameters are used (Eskelinen *et al.*, 2015). The solving algorithms are implemented in a MATLAB environment.

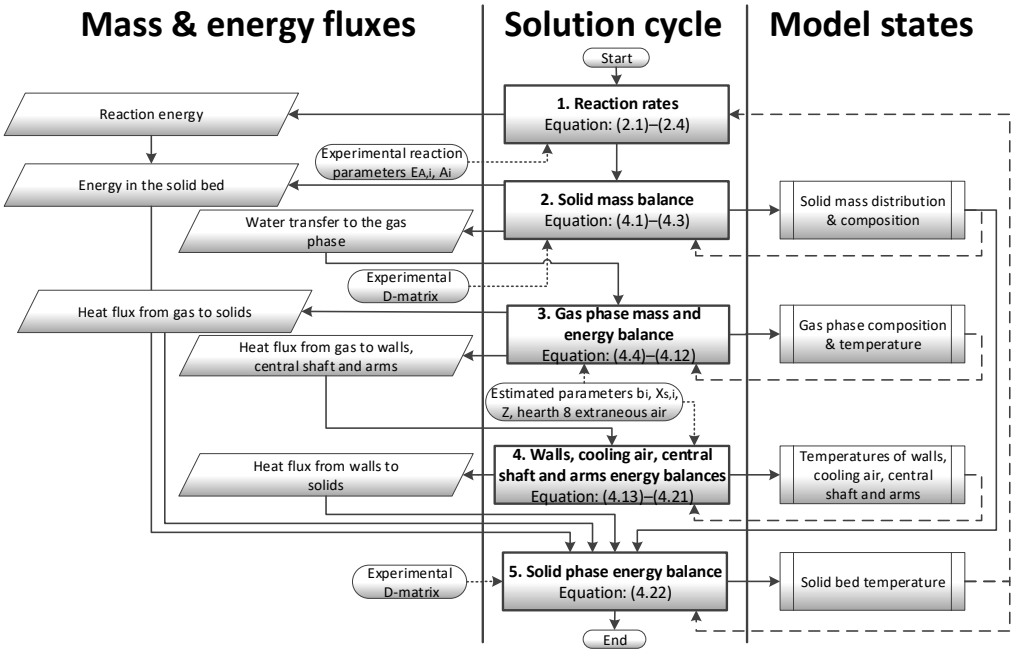

Figure 4.1 Scheme of the solution for the MHF model (Eskelinen *et al.*, 2015).

The simulation studies in Eskelinen et al., (2015) show that the results of the designed model are qualitatively good and its performance can be reported to follow the dynamic behavior of the industrial testing furnace. Therefore, the model can be utilized in the study of the physicochemical phenomena arising in the interior the furnace and to predict temperature profile of the furnace.

Summary

This chapter has outlined a detailed description of the dynamic model used in this study, which has been based on first principles with counter-current flows of the gas and solid phases. The main heat transfer mechanisms considered by the model have been the radiation and convection between the phases. The model has been reported to follow the dynamic behavior of the MHF with good accuracy. In Chapter 6, the model will be used in the simulation of the control strategy proposed in this work.

5. Analysis of the MHF dynamic behavior

This Chapter presents the analysis of the MHF dynamic behavior to provide understanding of the operating conditions and physicochemical phenomena taking place in the furnace. Different machine learning algorithms and the physicochemical equations of the kaolin calcination reactions are used for the analysis. First, the setpoints for the temperature profile of the MHF are determined using artificial intelligence. Next, the "spinel phase" reaction rate is studied and analyzed to detect the occurrence of this phenomenon inside the furnace. Then, the mullite content soft sensor is developed based on first principles and next based on artificial intelligence. Subsequently, the soluble alumina soft sensor based on artificial intelligence is developed. Finally, the Burner-to-Burner interaction phenomenon inside the hearth 4 is studied and analyzed.

5.1 Description of the feed material and product mineralogy

Natural kaolin deposits vary in quality and quantity. Therefore, in order to produce uniform and specific engineered kaolin products, the physical, chemical, and mineralogical properties of the raw kaolin ore are evaluated. Iron content, brightness, particle size and shape, are the most important properties to be measured. The physical and optical properties of kaolin such as particle size and shape, the particle size distribution, brightness, color, opacity, viscosity, surface area, dispersability, and hardness relate to their suitability for use as a pigment for coating paper.

These properties can be altered by selective processing (Murray and Kogel, 2005).

The iron present in the feed material becomes a particularly significant variable if the clay is calcined. Increasing the temperature of the clay up to high levels activates the iron present in the clay to be oxidized from the green/blue form to the red form and this causes the clay to turn slightly pink (Thomas, 2010). A process called beneficiation is utilized to eliminate iron (and other impurities) accompanying the kaolin ore before calcination. Beneficiation produces a kaolin comparable, in terms of brightness, with kaolin that naturally included low values of iron content once both clays had been calcined. This is a key discovery for the china clay industry as deposits of high-quality ore are depleting (Chandrasekhar and Ramaswamy, 2002).

The brightness, opacity and abrasiveness of crude kaolin can be increased by thermal treatment. These products are utilized as coating pigments and functional fillers by the paper industry. The heat treated kaolin can be divided roughly into two grades. The first grade has increased brightness and improved opacity. At the temperature range of 450 °C to 700 °C kaolinite dehydroxylates (Equation (2.2)), which breaks down the crystal structure of kaolinite leaving an amorphous mixture of alumina and silica which is called metakaolin (Murray and Kogel, 2005). This is a bulky product that is used as a paper coating additive to enhance resiliency and opacity in low basis weight sheets (Murray, 2005).

Heating kaolin further up to around 980 °C the amorphous mixture of alumina and silica reorganizes to form the so-called 'spinel phase' (Equation (2.3)). Heating the material even more, the spinel phase's crystal structure changes again, forming small crystals of mullite and high temperature quartz (cristobalite). The "spinel phase" and the mullite form the second grade, in which the relict plates aggregate to form particles with an open structure that have a relatively high light scattering coefficient. This standard calcined kaolin product has a brightness ranging between 92 and 94 % (Murray and Kogel, 2005). This grade's

surface chemistry and physical properties are completely changed, and it is whiter and more abrasive than the original kaolin. The abrasiveness of the calcined product is caused by the mullite and the objective is to reduce it to acceptable levels by selecting the feed kaolin properly and carefully controlling the calcination and the final processing after calcination. This product can be used as an extender for titanium dioxide in paper coating and filling and in paint and plastic formulations (Murray, 2005).

Pharmaceutical applications of kaolin require it to be calcined at temperatures around 1100 °C to make an intermediary product between the amorphous and crystalline "spinel phase". This stage indicates the equilibrium point between low reactivity and abrasiveness, which is necessary for calcined kaolin products (Thomas, 2010). For the industrial calcination of kaolin, the indicator to determine the progress of the calcination reaction is the quantity of soluble alumina (Al_2O_3). Therefore, the quantification of soluble alumina is used as the standard method to control the quality of the calcined kaolin.

5.2 Classification of process conditions based on the furnace feed and product type

An analysis of the historical data of the calciner was performed to identify the process operating conditions for different feed materials and products, using the self-organizing map (SOM) method (Kohonen, 1982). The theory of the SOM method is shortly described, and the subsection ends with the determination of the optimal setpoints for the temperature profile of the MHF.

5.2.1 The self-organizing map

Kohonen's SOM belongs to the category of unsupervised learning networks, which signifies that the network updates the weight parameters without a performance feedback from a trainer. One key

characteristic of this network is that it uses a method known as competitive learning, in which the nodes self-distribute over the input domain to identify clusters of the related input vectors, while the output nodes compete between each other to be excited in sequence in response to a specific input vector. After suitable training, the network generates a representation with low dimensionality of the input domain that upholds the organization of the main architecture of the network. This entails that input vectors with comparable features stimulate the near-layer nodes. Therefore, the nodes of the SOM may identify clusters of similar input vectors. Furthermore, this creates a topographic plotting of the input domain to the output layer, which is based mainly on the pattern of the input domain and causes dimensionality reduction of the input space. A diagram of a SOM with a 2-D output configuration is shown in Figure 5.1.

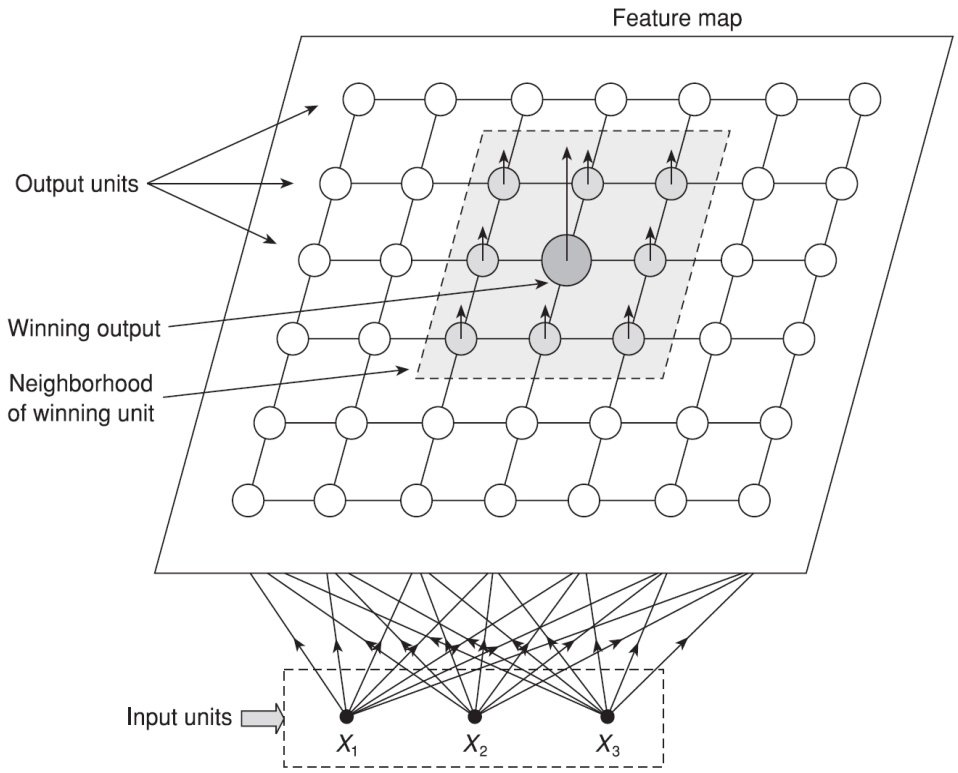

Figure 5.1 Kohonen's self-organizing map (Karray and De Silva, 2004).

The learning algorithm allows the clustering of the input data into a reduced set of components with interconnected characteristics. The basis of the algorithm is the competitive learning technique. Initially, there is the assumption that the input data are given by vector x and the weight vector linking the input components to an output node is denoted by w_{ij}.

The weight vector has coordinates given by subscripts i and j. In general, the weight vectors are standardized to a unitary measure. N_c represents the neighborhood nearby the selected output candidate, where its size decreases after every iteration of the algorithm until convergence is achieved. The sequence of the learning algorithm is presented as follows:

1. Assign small random values to all weights. Establish a value for the neighborhood N_c and a value for the starting learning rate α.
2. Select an input pattern x from the input data set.
3. Choose the unit c (the matching output unit index) so that the performance index I minimizes the Euclidian distance from x to w_{ij}:

$$I = \|x - w_c\| = \min_{ij} \|x - w_{ij}\| \tag{5.1}$$

4. Update the weights based on the global network from iteration k to iteration $k + 1$ as:

$$w_{ij}(k+1) = \begin{cases} w_{ij}(k) + \alpha(k)\left[x - w_{ij}(k)\right], & if\ (i,j) \in N_c(K) \\ w_{ij}(k) & if\ (i,j) \notin N_c(K) \end{cases} \tag{5.2}$$

   where $\alpha(k)$ is the adaptive learning rate (positive value less than unity) and $N_c(k)$ is the neighborhood of c at iteration k.
5. The α and N_c are reduced after each iteration based on the appropriate scheme. For example, Kohonen recommended a reducing function in the form of $\alpha(k) = \alpha(0)(1 - k/T)$, where T is the number of training iterations and $\alpha(0)$ the initial learning rate limited to a value of one. For the neighborhood, several researchers suggested a starting region with a half size of the output grid, which is reducing based on exponentially decaying behavior.
6. The learning algorithm endures until a satisfactory number of iterations has been achieved or until all outputs attain a threshold of sensitivity based on a portion of the input space.

5.2.2 Determination of the setpoints for the temperature profile of the MHF

The temperature profile of the MHF plays a key role in the efficient control of the calciner. The main aim of the process condition classification based on the feed and product types is to determine the optimal temperature setpoints for hearths 4 and 6 versus the different capacity levels.

The variables used to train the SOM algorithm were the feed rate, iron content, gas flows, temperatures of hearths 4 and 6, mullite content, soluble alumina of the product, and brightness of the feed and product. The so-called U-matrix was then used, as depicted in Figure 5.2. The U-matrix, resulting from the SOM method for the data for June 2017, associates a point (hexagon) to a product and its corresponding operating conditions. During this period, two different products were produced (P1 and P2). The difference between the products and their respective

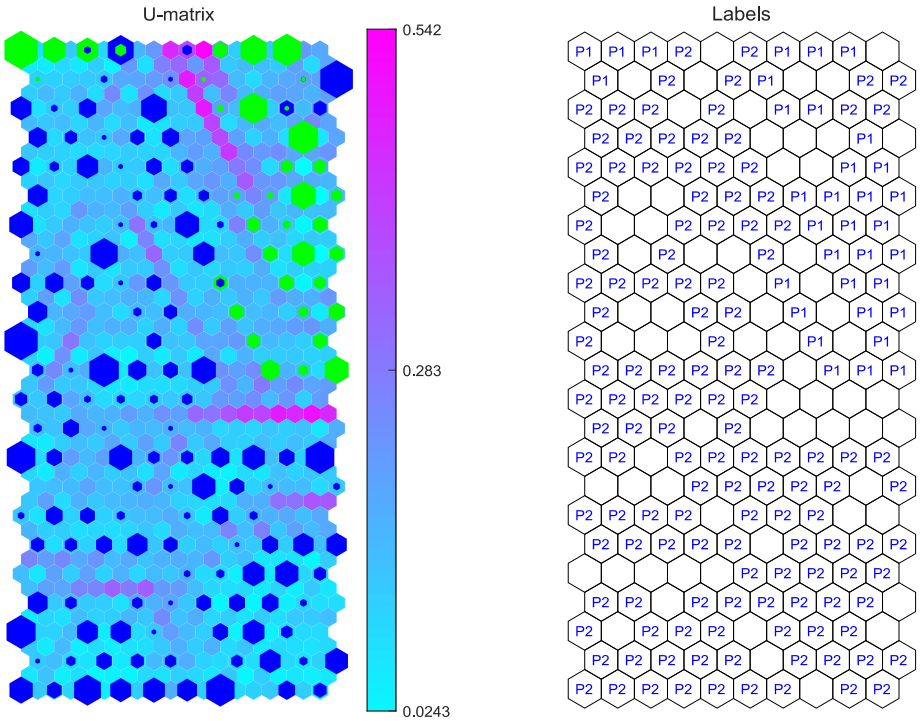

Figure 5.2 U-Matrix obtained using the SOM method for the process data, June 2017.

process conditions were noticeable, as shown in Figure 5.2, where P1 and P2 are represented by the green and dark blue hexagons, respectively.

The SOM technique enabled the finding of the optimal process operating conditions for different kinds of products based on the feed material and product data. The feed rate, iron content, and brightness of the feed and product were used to construct look-up tables to identify the best temperature setpoints for the hearths 4 and 6 depending on the product type (Figure 5.3). The temperature and capacity setpoints of the table were verified by the mass and energy balance equations.

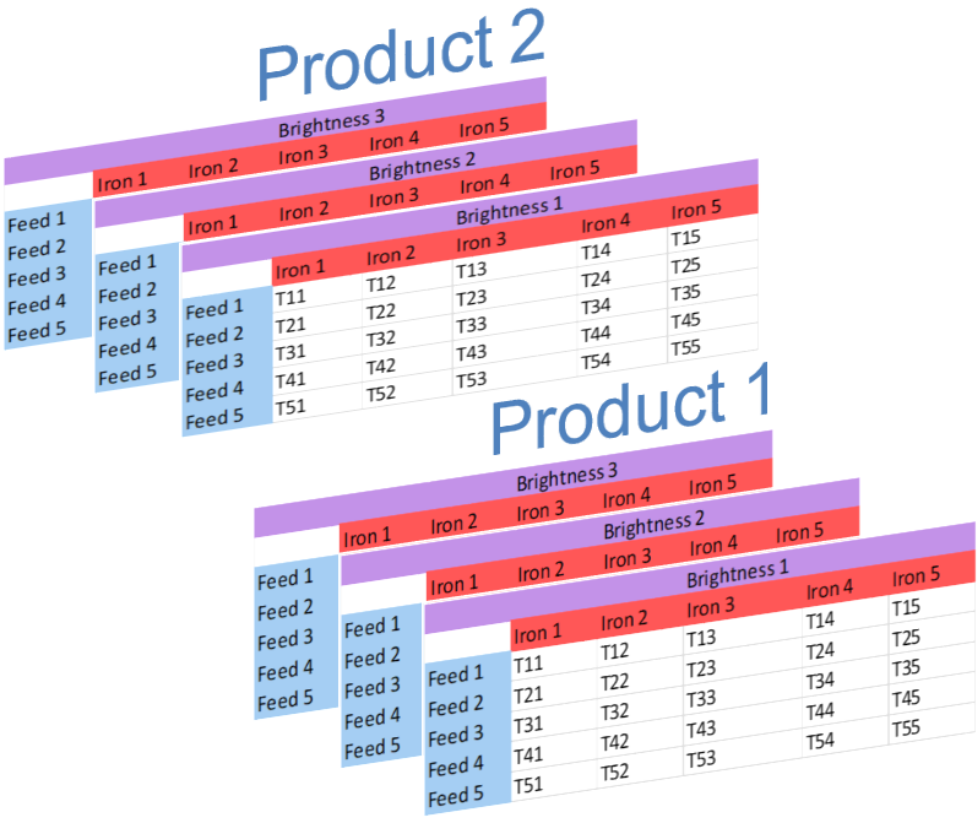

Figure 5.3 Examples of the look-up tables obtained from the SOM.

5.3 Soft sensor 1: Spinel phase reaction rate monitoring for energy savings

The kaolin calcination in an MHF is a process that depends on the temperature, and the temperature profile control guarantees the quality of the product. The kaolin that is calcined to the “spinel phase” is the product of interest and is generated by a reaction that produces a massive amount of heat (Equation (2.3)), which normally occurs in the hearth 6.

The relocation of this reaction to a different hearth disturbs the product quality and, therefore, the temperature profiles of the MHF have to be monitored and controlled. However, the required measurements to determine the instances when the kaolin transforms to the “spinel phase” are not present. To solve this problem, a soft sensor was developed to estimate the rate of the exothermic reaction occurring in the hearth 4, which is an alternative practical approach.

Several occurrences when the hearth 4 gas flow fluctuated together with the temperature measurements in the hearth 5 were demonstrated through data analysis. Several ore properties (e.g. particle size, ore impurities), and the temperature of the solid material greatly affect the beginning of the reaction in Equation (2.3). The “spinel phase” exothermic reaction (Equation (2.3)) may take place at the hearth 4 if the temperature of the solid phase is suitably high (925–1050 °C). For these cases, a feedforward control based on the reaction indicator of the “spinel phase” would provide an excellent solution to maximize the energy savings in the furnace by sensing the reaction in the top part of the furnace and then controlling the temperature in the bottom part of the furnace. A data analysis was performed, for the cases obtained from the industrial data for the period of May to October 2013, to validate the energy savings possibilities. The results of the analysis confirmed the increased reaction rate events. A few examples of these occurrences are presented in Figure 5.4. The variation of the temperature in the hearth 5 can be determined through the initiation and termination of the exothermic reaction in the hearths 4 and 5. The volumetric flow of gas needed to regulate the temperature in the hearth 4 lowers after the exothermic reaction is initiated. Near the termination of the exothermic reaction, a larger volumetric flow of gas is required to control the desired temperature. To summarize, the events of increased reaction rate are observed when the gas flow to the hearth 4 declines suddenly while the hearth 5 temperature rises.

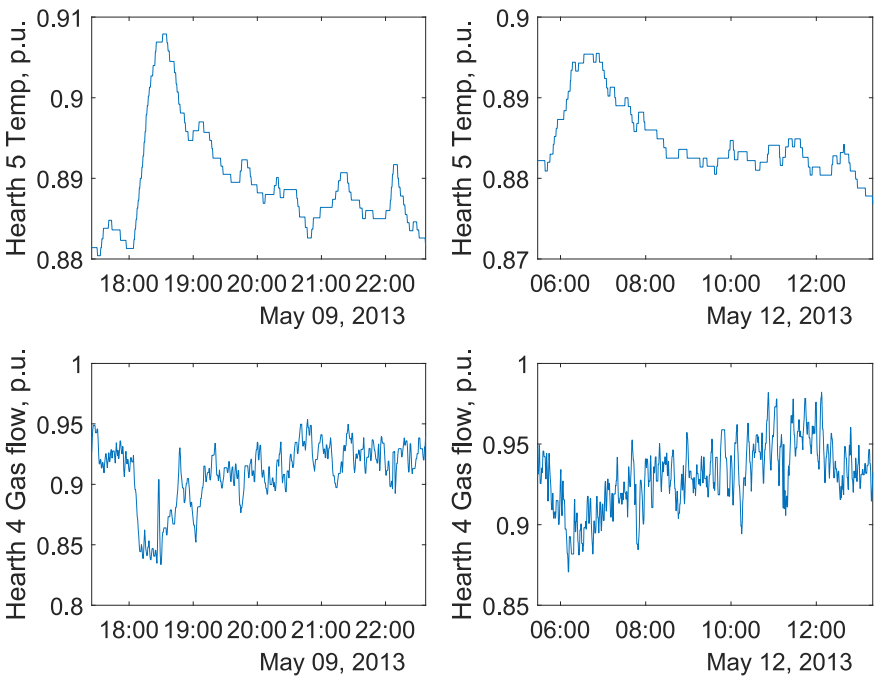

Figure 5.4 Examples of the initiation and termination of the exothermic reactions in hearths 4 and 5 (Jämsä-Jounela, et al., 2018).

A soft sensor that measures the exothermic reaction rate occurring in the hearth 4 is required to maximize the energy savings of the furnace. The law of energy conservation is used to develop the energy balances of the first four hearths of the furnace (Jenkins and Mullinger, 2008). The heat of the methane combustion occurring in the hearth 4, and the hearth 5 cooling air flow are used as inputs. The stoichiometric ratio of the fuel gas and air is used to determine the quantity of air needed for complete combustion. The energy exits the furnace through the solid material, exhaust gases, and heat dissipation, which comprise the cooling air and heat exchange with the environment.

The equations defining the energy balance for the gas and solid phases are presented as follows.

$$\frac{\partial Q}{\partial t} = Q_{\mathrm{s,in}} - Q_{\mathrm{s,out}} - Q_{\mathrm{evap}} + Q_{\mathrm{dehyd}} + Q_{\mathrm{spin}} + Q_{\mathrm{sg}}, \tag{5.3}$$

$$Q_{\mathrm{g,in}} - Q_{\mathrm{g,out}} + Q_{\mathrm{comb}} - Q_{\mathrm{gs}} = 0 \tag{5.4}$$

where $\frac{\partial Q}{\partial t}$ represents the rate of energy variation with respect to time; the enthalpies of the entering and exiting kaolin are represented as $Q_{\text{s,in}}$ and $Q_{\text{s,out}}$, respectively; Q_{evap} symbolizes the enthalpy of evaporated water; Q_{dehyd} represents the heat consumed as a consequence of the dehydroxylation reaction; Q_{spin} denotes the heat discharged during the "spinel phase" formation in the hearth 4; and Q_{sg} signifies the heat transfer between the solid phase and the gas phase. The enthalpies of the incoming and outgoing gases are designated as $Q_{\text{g,in}}$ and $Q_{\text{g,out}}$ respectively; Q_{comb} denotes the heat generated by the methane combustion occurring in the burners of the hearth 4, and Q_{gs} represents the heat transferred between the gas phase and the solid phases. Assuming steady-state conditions, the rate of energy change is zero and the heat discharged by the spinel formation reaction is defined as follows:

$$Q_{\text{spin}} = -Q_{\text{s,in}} + Q_{\text{s,out}} + Q_{\text{evap}} + Q_{\text{dehyd}} + Q_{\text{g,in}} - Q_{\text{g,out}} + Q_{\text{comb}} \qquad (5.5)$$

Next, the rate of reaction (r) is calculated as the fraction of kaolin transformed into the "spinel phase" in the hearth 4, as shown in the following equation:

$$r = \frac{Q_{\text{spin}}}{H_{\text{S}} F_K} \qquad (5.6)$$

where H_{S} is the product formation heat and F_K is the current feed rate.

Finally, the data available from May to October 2013 was used to calculate the reaction rate (r). The initiation, termination, and duration of the spinel formation reaction was studied using the soft sensor. The average extent of the reactions for the data analyzed was 118 minutes with a maximum of 232 minutes and a minimum of 22 minutes. The reaction in Equation (2.3) affects the total gas burned, mostly diminishing it by nearly 1.5% per hour (Jämsä-Jounela *et al.*, 2018).

5.4 Soft sensor 2: Mullite content indicator for capacity improvement

During normal process conditions, the temperature within the furnace enables a total transformation of metakaolin to the "spinel phase" at 925 °C (Equation (2.3)). The "spinel phase" is converted into mullite at a greater temperature, 1050 °C (Equation (2.4)). Therefore, the quantity of mullite is inversely proportional to that of the "spinel phase" as the reaction marches. Thus, the mullite content can be defined as an indirect indicator of the quantity of the final product. In other words, if the final product holds a substantial quantity of mullite, then the temperature inside the furnace was larger than the temperature range of the "spinel phase" reaction. Therefore, monitoring the temperature during mullite formation offers a way of enhancing the calcination, mostly by raising the feed rate and lowering the temperature (which reduces mullite formation), which to creates a product with optimal quality.

5.4.1 Mullite content soft sensor based on mass and energy balances

A measurement of mullite content is not available online. Therefore, in this work, a soft-sensor based on energy balances was created to calculate the quantity of mullite in the product. The energy balances were defined based on the heat transfer flow through the furnace. The equations describing the energy balances are as follows:

$$\frac{\partial Q_{tot}}{\partial t} = Q_{comb} - Q_{loss} - Q_{gas} - Q_{air} - (Q_{solid} + Q_{mul}) = 0 \qquad (5.7)$$

$$Q_{solid} = Q_{water} + Q_{kao} + Q_{dehyd} + Q_{meta} + Q_{spin} + Q_{prod} \qquad (5.8)$$

where $\frac{\partial Q_{tot}}{\partial t}$ is the rate of heat transfer, Q_{comb} is the total heat generated by the methane combustion, and Q_{loss} is the heat loss to the environment. Q_{gas} denotes the enthalpy of the energy acquired by the gas phase, the enthalpy difference in the central shaft cooling air is represented as Q_{air}, the change of energy in the solid phase is represented as Q_{solid}, and the

total energy of mullite formation is denoted as Q_{mul}. Furthermore, Q_{solid} is described in (Equation (5.8)), where Q_{water} is the heat to evaporate free water, Q_{kao} denotes the enthalpy to heat kaolin to 450 °C, Q_{dehyd} represents the heat of the dehydroxylation endothermic reaction, Q_{meta} symbolizes the enthalpy to heat metakaolin to 1000 °C, and Q_{spin} denotes the energy discharged during the "spinel phase" reaction. Finally, Q_{prod} represents the energy discharged to lower the temperature of the final product to 700 °C.

Assuming that all the variables of the Equation (5.7) are measurable and process conditions are in steady-state, then the total enthalpy of mullite formation (Q_{mul}) is defined as follows:

$$Q_{mul} = Q_{comb} - Q_{loss} - Q_{gas} - Q_{air} - Q_{solid} \tag{5.9}$$

Subsequently, the mullite mass can be calculated as follows:

$$m_{mul} = \frac{Q_{mul}}{H_{mul}} \tag{5.10}$$

where m_{mul} is the mullite mass, and H_{mul} is the formation enthalpy of mullite.

A soft sensor was developed to estimate the mullite content in the product using first principle thermochemical equations and balances. A sampling campaign performed in June 2017 provided the data to validate the estimations of the soft sensor. The data includes the process measurements as well as X-ray diffraction (XRD) analyses results for the mullite content in the product. The process data were used in the soft sensor to estimate the mullite content, which was compared to chemical analyses, as shown in Figure 5.5. The mullite content calculated using the soft sensor showed fairly good precision compared with the XRD results.

.

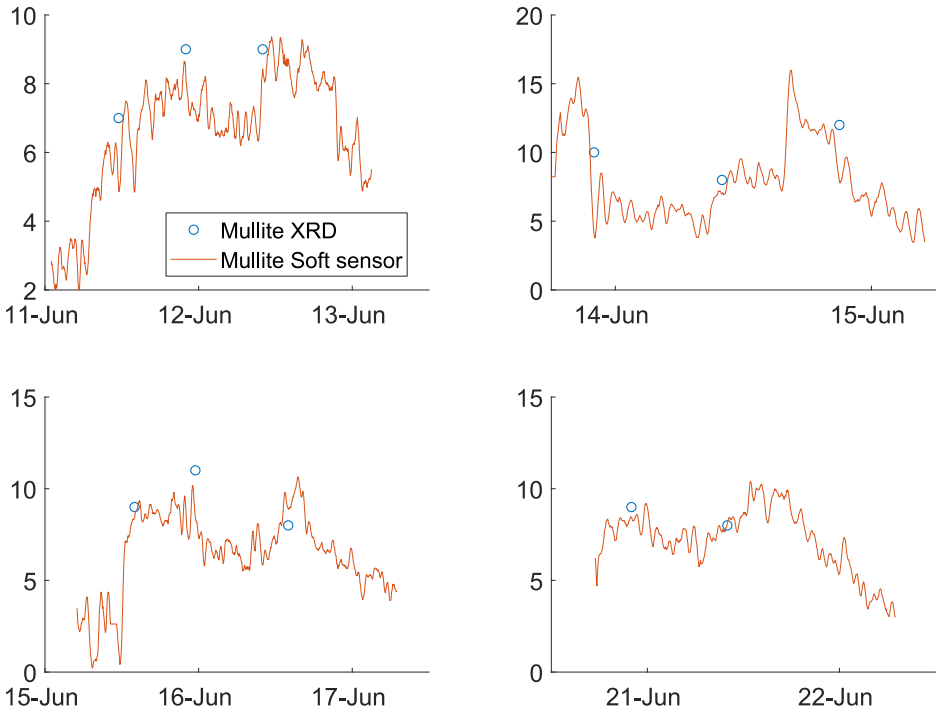

Figure 5.5 Mullite content, XRD vs the soft sensor estimation (Gómez Fuentes and Jämsä-Jounela, 2018a).

5.4.2 Mullite content soft sensor based on an artificial neural network

A neural network soft sensor, based on a multi-layer architecture, was developed to calculate the mullite quantity in the final product. The five input variables included the kiln feed, hearth 4 temperature, hearth 4 gas flow, hearth 6 temperature and hearth 6 gas flow, and. In a typical multi input/single output (MISO) neural network model, the training set can be denoted by $D = \{Y, X_i \mid i = 1,2,\ldots,m\}$, where Y is the output vector and X_i is the ith input vector expressed as $Xi = [x_{1i}, x_{2i}, \ldots, x_{ni}]$ (m represents the number of input variables and n symbolizes the number of training samples).

Then, the test data set can be denoted by $X \in R^{n \times m}$. To avoid the effect of multiple dimensions from the process variables, it is necessary to standardize the data for mathematical convenience. The standardization equation is defined as follows:

$$X_b = \frac{X - \mu}{\sigma} \tag{5.11}$$

where X_b represents the vector containing the standardized input data, and μ and σ represent the mean and standard deviations of X respectively. The mean squared error (MSE) is considered the neural network performance function to train the soft sensor estimator:

$$MSE = \sum_{k=1}^{n} \frac{\left(\hat{Y}_k - Y_k\right)^2}{n} \tag{5.12}$$

where $\hat{Y}$ is the estimated output of the soft sensor, Y is the vector of the observed data, and n denotes the number of data points.

The neural network implemented to estimate the mullite content contains four layers: three hidden layers and one output layer. In the soft sensor model, the output from the k^{th} node in the hidden layer is obtained by Equation (5.13).

$$o_j = f\left(\sum_{i=1}^{p} w_{ij} X_i - b_j\right) \tag{5.13}$$

where p symbolizes the number of input nodes, f denotes the activation function of the node, w_{ij} represents the connection weight from the ith input node to the jth hidden node, and b_j signifies the node's activation threshold. The function f defines the activation function of the hidden layer nodes, which in this case comprises a sigmoid function. Equation (5.13) is calculated for all the hidden layers, where the output is introduced to each subsequent hidden layer. Then, the data resulting from the output layer are obtained according to Equation (5.14).

$$\hat{y}_k = f\left(\sum_{l=1}^{q} w_{lk} o_l - b_k\right) \tag{5.14}$$

where q is the number of nodes in the final hidden layer, w_{lk} is the weight related to the connection of the l^{th} hidden node and the k^{th} output node, and b_k is the output node activation threshold.

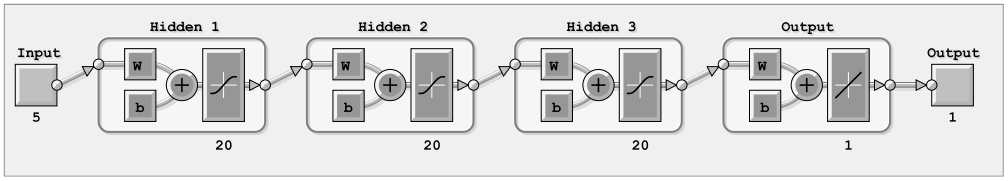

Figure 5.6 Four-layer feedforward neural network architecture.

The final design of the network included three hidden layers, each with 20 nodes, and a single node output layer as depicted in Figure 5.6. During the training of the model, the efficiency of different training algorithms was contrasted to choose the best result. The training algorithms included are as follows: the Levenberg–Marquardt (LM), Bayesian regularization (BR), and Broyden–Fletcher–Goldfarb–Shanno (BGFS) quasi-Newton backpropagation. In the creation of the model, the same data from June 2017 were used and randomly divided into three sets: training (70%), validation (15%), and testing (15%). Finally, the model was limited to a maximum of 1000 epochs, and training was performed using the neural network toolbox in MATLAB 2018b.

From Table 5.1, the performance comparison of the training algorithms shows that the LM and BGFS provided similar results with an MSE of less than 0.4 and a correlation coefficient R^2 of approximately 0.70, taking less than 2 minutes to train. The performance of the BR algorithm was quite superior compared to the other two, with an MSE of 0.2126. The only disadvantage of the BR algorithm was that the training time was almost 12 minutes. Although it took longer in comparison to the other algorithms, the BR algorithm was considered the best option for the final model training due to its performance.

Table 5.1 Performance comparison of the training algorithms for the mullite content soft sensor

Training algorithm	MSE	R^2	Training time, min
LM	0.3660	0.6993	0.55
BR	0.2126	0.8936	11.55
BGFS	0.3927	0.6647	1.41

The results of the soft sensor model using the BR algorithm are presented in Figure 5.7. A regression correlation coefficient of 0.8936 was obtained by the mullite content modeling. In general, the model prediction was fairly acceptable but could be further improved, e.g., by testing different architectures and including more process variables. Furthermore, additional process data would be useful for improving the reliability of the soft sensor model.

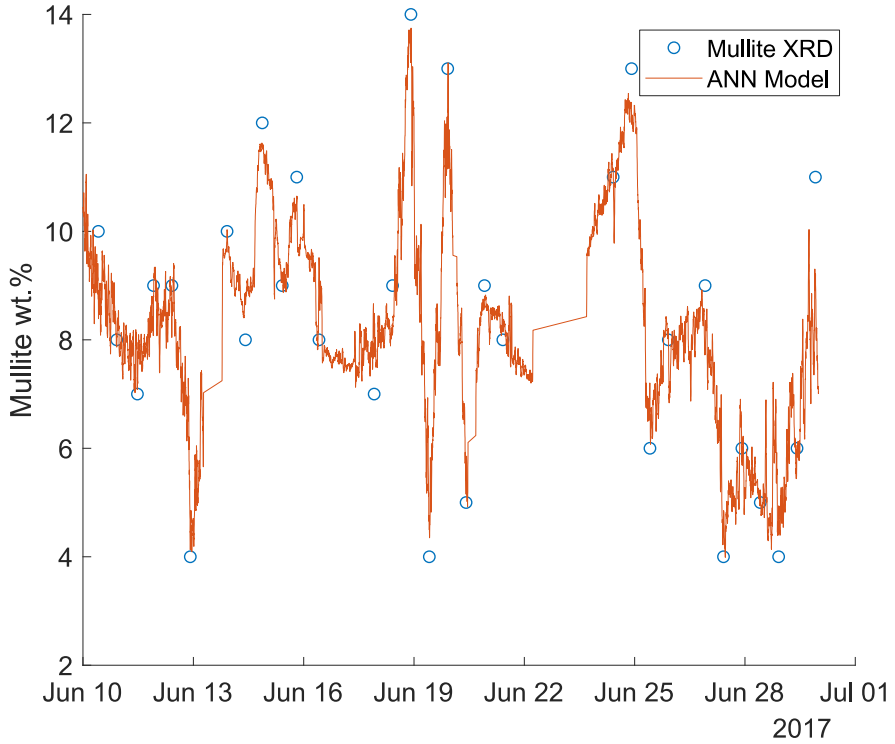

Figure 5.7 Comparison of mullite content: XRD vs. the ANN soft sensor.

5.5 Soft sensor 3: Soluble alumina soft sensor based on an artificial neural network

The main indicator in the industry for the quality control of some calcined kaolin products is the quantity of soluble alumina (Al_2O_3). This indicator is adopted to estimate the intermediary stages between the transformations of metakaolin and mullite (Equations (2.2) and (2.4)). However, the determination of soluble alumina requires extended amount of time using laboratory techniques, which is counterproductive to the requirements of a continuous production process. A feedforward multi-layer perceptron neural network was considered as the basis for developing a soft sensor that models the soluble alumina in the final product. The utilized input variables were the kiln feed, hearth 4 temperature, hearth 4 gas flow, hearth 6 temperature, and hearth 6 gas flow. The neural network architecture and tuning criteria including the selection of the training algorithm, and the training, validation, and testing data sets were selected equally, as described in Section 5.4.2.

Table 5.2 Performance comparison of the training algorithms for the soluble alumina soft sensor

Training algorithm	MSE	R^2	Training time, min
LM	0.1497	0.8998	1.41
BR	0.1128	0.9540	13.70
BGFS	0.2052	0.8316	1.66

Table 5.2 presents a performance comparison of the training algorithms, with every algorithm providing similar MSE results of less than 0.21 and a correlation coefficient R^2 of approximately 0.90, taking less than 2 minutes to train for the LM and BGFS algorithms. The results of the BR algorithm are remarkable, with an MSE of 0.1128. As before, the BR algorithm training took longer than the other two algorithms, requiring almost 14 minutes. In this case, the BR algorithm may be the optimal choice because of its minimal prediction error.

Figure 5.8 depicts the results of the soluble alumina soft sensor model trained with the BR algorithm, compared with the soluble alumina

measurement using inductively coupled plasma atomic emission spectroscopy (ICP-AES). The soft sensor presents a regression correlation coefficient of 0.9540, indicating that the ANN soft sensor is a reliable choice for estimating soluble alumina in real time. The inclusion of more process variables and the evaluation of various architecture structures provide an opportunity to improve the soft sensor estimations. Furthermore, the addition of extended data sets would enhance the accuracy of the soft sensor model.

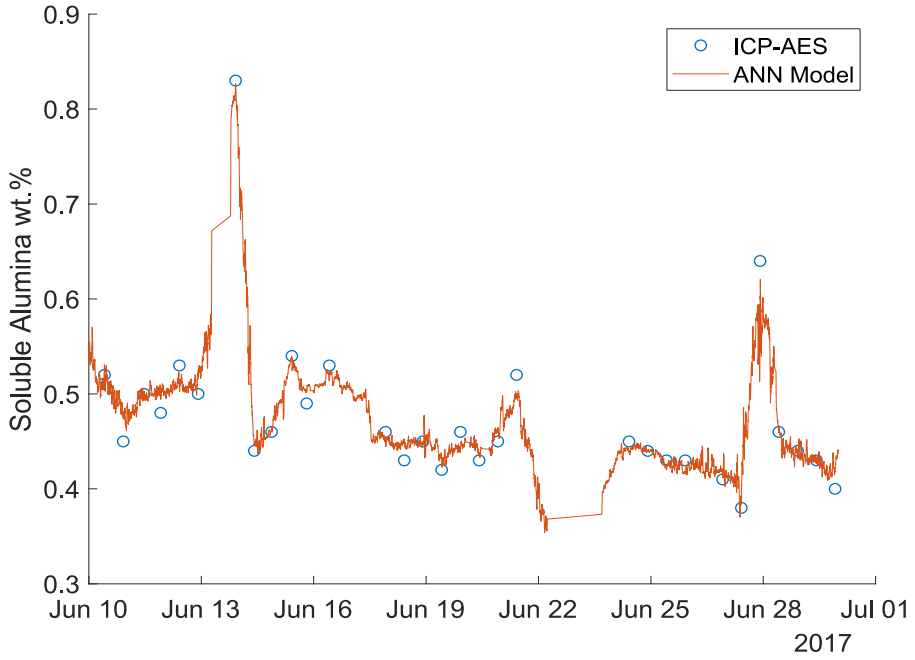

Figure 5.8 Comparison of soluble alumina: ICP-AES vs. ANN soft sensor (Gómez Fuentes *et al.*, 2019).

5.6 Burner-to-burner interaction effect on the basic temperature control

Industry faces challenges to reduce the nitrogen oxide (NOx) emissions in multi-burner furnaces. Therefore, enhanced burner designs have been applied to tackle this issue. In general, these designs implement a kind of furnace gas recirculation that lowers the flame temperature, therefore minimizing the NOx emissions. However, to reduce the flame temperature, a decrease in the concentration of air is required which generates elongated flames. The flames in recently developed multi-burner furnaces with enlarged flame length might lead to a phenomenon defined as burner-to-burner (BtoB) interaction (Fleifil *et al.*, 2006).

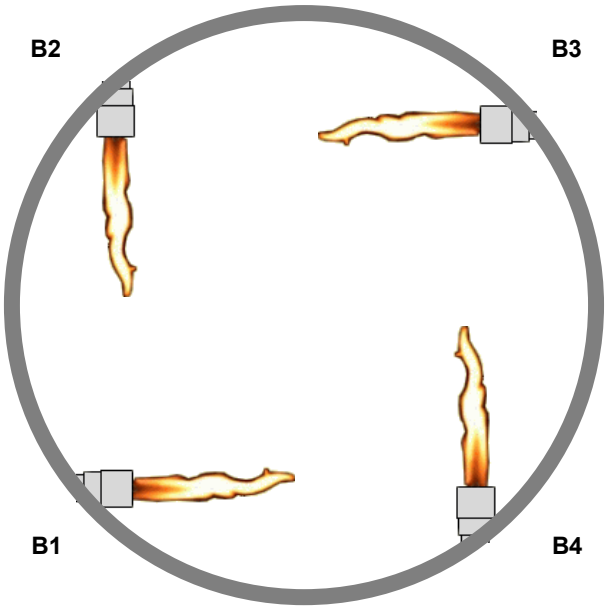

Figure 5.9 Configuration of the burners in the multiple hearth furnace.

The configuration of the burners inside the MHF provides a sharp view of the interactions occurring in the furnace. The burners are positioned in four equidistant points over the perimeter of the hearth. Each burner is positioned in one of the points and is directed to the closest burner, thus Burner 1 (B1) points to Burner 4 (B4), B4 points to Burner 3 (B3), etc., as depicted in Figure 5.9. The temperature control implemented in the hearths 4 and 6 comprises individually operating PI controllers for each burner. It is possible that a larger capacity operation may create difficulties to control the temperature in the MHF. These difficulties are most probably associated to the BtoB phenomenon, which generates nonlinearities and instabilities in the temperature control.

The current temperature control scheme implemented in the MHF displays shortcomings when a BtoB phenomenon ensues during the process operation, generating unwanted interactions and inhibiting the stable control of the gas phase temperature. In this work, the BtoB phenomenon was simulated and is illustrated in Figure 5.10. In the initial 170 minutes of the simulation, the controller attempted to regulate the temperature to 1000 °C with the corresponding manipulated gas flows. After 170 minutes, the controller attempted to regulate the temperature to 960°C with the corresponding manipulated variables. In the initial part (1000 °C setpoint), only one control loop worked while the other loops

reach a maximum gas flow. The second part of the simulation presents that only one temperature controller regulated the temperature partially, with a working control loop switch at simulation times of 220 and 290 minutes.

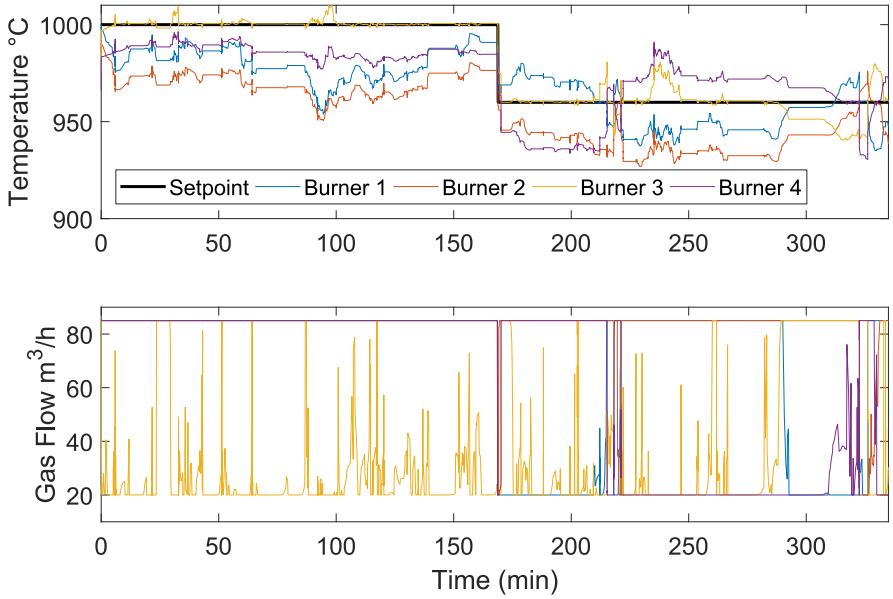

Figure 5.10 Simulation results of the temperature setpoint change for the hearth 4 current temperature control.

A more efficient control scheme is needed to enhance the stability of the temperature and prevent the effects of the BtoB interaction in the hearth 4. Some alternatives are existing to enhance the temperature control in the hearth 4. A mean temperature control scheme can be adopted as a practical answer to the phenomenon.

Summary

This chapter has exposed the analysis of the MHF's dynamic behavior and has provided understanding of the feed material and product mineralogy as well as the operating conditions and physicochemical phenomena taking place in the furnace. It has also introduced three soft sensors to determine different mineralogical information occurring inside the process, such as the "spinel phase" reaction rate, mullite content and soluble alumina. The soft sensors that have been developed will be incorporated into the control strategy of the MHF in the next chapter.

6. Mineralogy-driven control strategy for the multiple hearth furnace

In this chapter the details of the mineralogy-driven control strategy for the MHF are defined. Furthermore, the simulation results of the enhanced control strategy are presented and discussed. First, an overview of the simulation environment is presented. Second, the results of the basic temperature control simulation are shown. Next, the feedforward control simulation results are depicted and finally, the results of the optimizing control are reported and discussed.

6.1 The enhanced control strategy for the MHF

The enhanced control strategy proposed in this research aims to select the best operating conditions to optimize the production capacity and energy efficiency, while ensuring the required product quality. The process control system comprises the optimizing, stabilizing, and basic levels.

The plant personnel determine the final product specifications with regard to the current feed mineralogy. The product quality requirements e.g., the soluble alumina content and brightness, are defined next to the selected product specifications. The look-up table provides the setpoints for the gas temperatures in the hearths 4 and 6 based on the current production capacity, iron content and brightness in the feed. As described in Section 5.2, the look-up table is based on the classification of the feed type and process conditions, and made by using the SOM technique (Jämsä-Jounela *et al.*, 2018). Furthermore, the temperature setpoints are fine-tuned on a regular basis e.g., once a day, based on laboratory

measurements of the product characteristics; this is done to maintain the product quality within the specifications.

To reach the maximum production rate, specified by the mullite content soft sensor, the multi-objective optimization problem is solved to raise the plant capacity and simultaneously minimize the total energy consumption of the furnace ($F_{H4} + F_{H6}$) by adjusting the temperature setpoint (T_6) in order to maintain the required mullite content.

$$\begin{matrix} max\ F_K \\ min\ (F_{H4} + F_{H6}) \end{matrix} \tag{6.1}$$

with respect to constraints:

$$\begin{aligned} f_{T4}(F_{H4}, F_{H6}, r, F_K) &= T_4, \\ f_{T6}(F_{H4}, F_{H6}, r, F_K) &= T_6, \\ m(F_{H4}, F_{H6}, T_{H1}, F_K) &\leq 4wt.\%, \\ S(F_{H4}, F_{H6}, r, F_K) &\leq 0.50wt.\%, \\ \mathrm{T}_{H6} &\geq T_{H6}^{min}(F, r), \\ T_{H4}^{min} < T_{H4} &< T_{H4}^{max}, \\ Vio &\geq Vio^* \end{aligned}$$

where F_K, F_{H4}, and F_{H6} represent the feed rate and gas flows to the hearths 4 and 6, respectively, r denotes the current value of the reaction soft sensor, T_{H1}, T_{H4} and T_{H6} are the temperatures in the hearths 1, 4, and 6, respectively and m is the mullite content of the product and its threshold. S represents the soluble alumina content and its threshold (if applicable). Finally, Vio symbolizes the brightness (measured as the percentage of light reflected in the violet spectrum) and its threshold. The control strategy is presented in Figure 6.1, which first highlights the selection of the initial temperature setpoints for the furnace from the look-up table, based on the running capacity of the furnace, the iron content and the brightness of the feeding material and product. Additionally, the figure highlights the integration of the mullite content (for capacity maximization) and soluble alumina (quality control) soft sensors as constraints into the enhanced control strategy for the MHF.

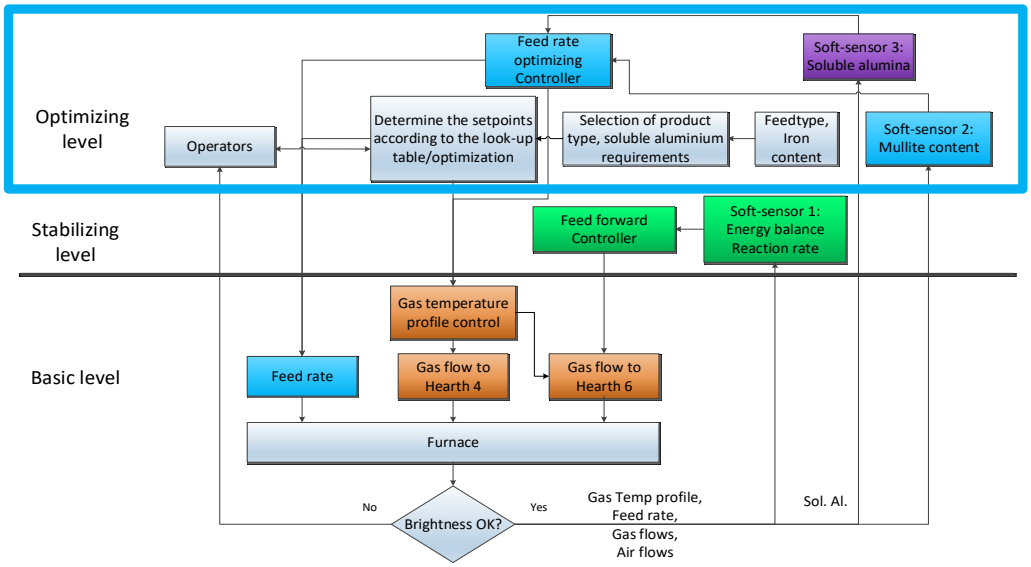

Figure 6.1 Enhanced control strategy highlighting the selection of the initial setpoints based on the look-up tables.

Next, Figure 6.2 and Figure 6.3 highlight the integration of the reaction rate soft sensor, described in Section 5.3, into the enhanced control strategy as part of the stabilizing control. The stabilizing level aims to attenuate the variations in the calcination reaction, which occur in the solid phase of the furnace. In other words, the gas temperature setpoints of hearth 6 have to be modified based on the calcination progress in the solid phase. Thus, if the exothermic reaction (Equation (2.3)) is initiated between the hearths 4 and 5, before the material enters the hearth 6, then the temperature setpoints must be lowered to save fuel and to prevent over calcination.

To assess the calcination progress of the kaolin, the soft sensor is used to estimate the exothermic “spinel phase” reaction rate (Equation (2.3)) in the hearths 4 and 5, and the feedforward control adjusts the temperature in the hearth 6. As a summary, a simplified block diagram of the algorithm designed for the feedforward control is presented in Figure 6.3.

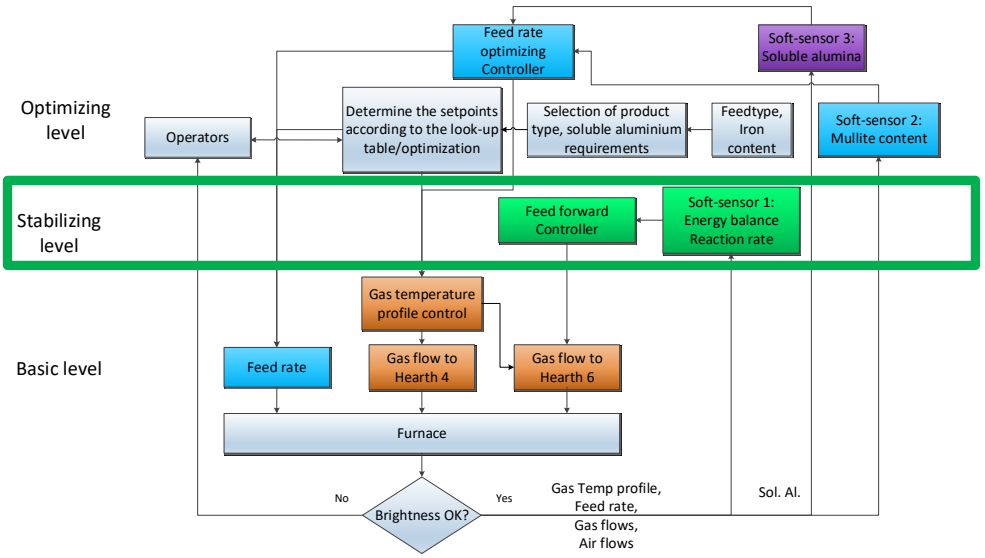

Figure 6.2 Enhanced control strategy highlighting the reaction rate soft sensor and feedforward control.

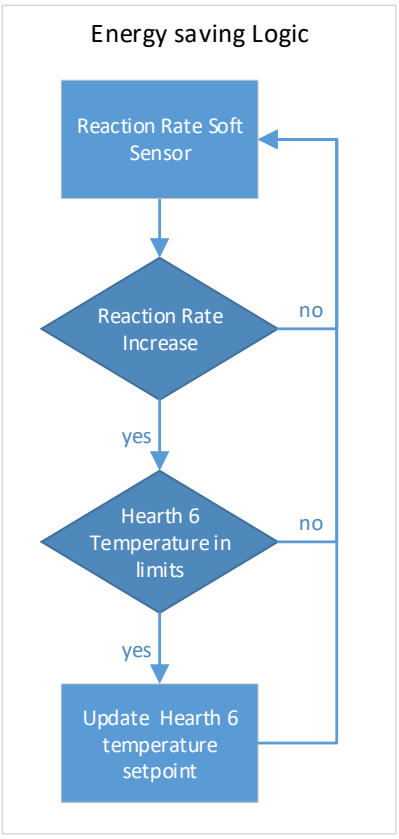

Figure 6.3 Feedforward control logic.

The basic level controls the temperature with a mean temperature control scheme (Gómez Fuentes, 2016), as highlighted in Figure 6.4. The mean temperature control aims to attenuate the effects of the burner-to-burner (BtoB) (Fleifil *et al.*, 2006) phenomenon and to homogenize the

gas phase temperature in the hearth 4 by operating based on the average temperature of the gas phase instead of manipulating each burner individually.

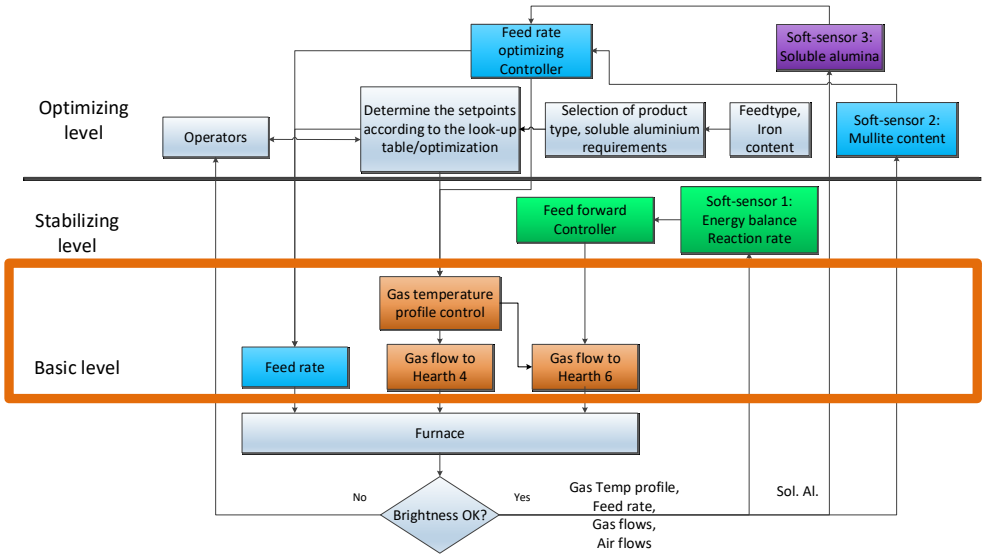

Figure 6.4 Control strategy highlighting the basic level temperature control.

A simple schematic of the mean temperature control is illustrated in Figure 6.5. The controller consists of the measurement of the temperature of the four burners and subsequently calculates the average temperature value. Based on this calculation, control regulation is implemented into the burner system by the manipulation of gas flows. Every gas flow is manipulated in an identical manner.

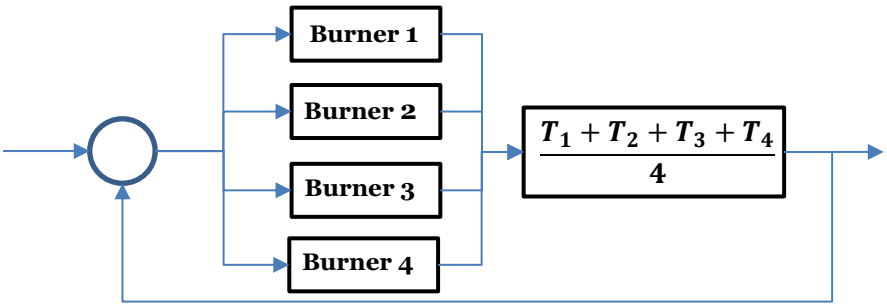

Figure 6.5 Mean temperature control scheme.

Finally, the feed material is transferred to the kiln by a weight feeder via a rotary valve. The operation of the rotary valve is controlled by the feed control via a programmable logic controller.

6.2 Simulation environment

The setup environment to model and control the MHF was developed in the MATLAB® environment. The setup consisted of the dynamic model of the MHF described in Section 4 and the following controllers: optimizing control, stabilizing control, and basic controllers. The implemented soft sensors were the mullite content soft sensor for capacity improvement and the “spinel phase” reaction rate indicator for energy use minimization. To increase the computation speed, the mechanistic model was implemented and precompiled in the C language. All other functions were implemented using the functions of MATLAB® library. The simulation environment included an Euler solver with a step size of 20 seconds. An overview of the simulation environment is illustrated in Figure 6.6. The noise present in the gas flows and temperatures were calculated from the process data provided from May to October 2013. The focus of the testing is the incorporation of the soft sensors to the control strategy, which are the novel components in the control strategy. However, the limited accessibility to online quality measurements limits the testing of the control strategy in closed-loop and needs additional online testing at the plant.

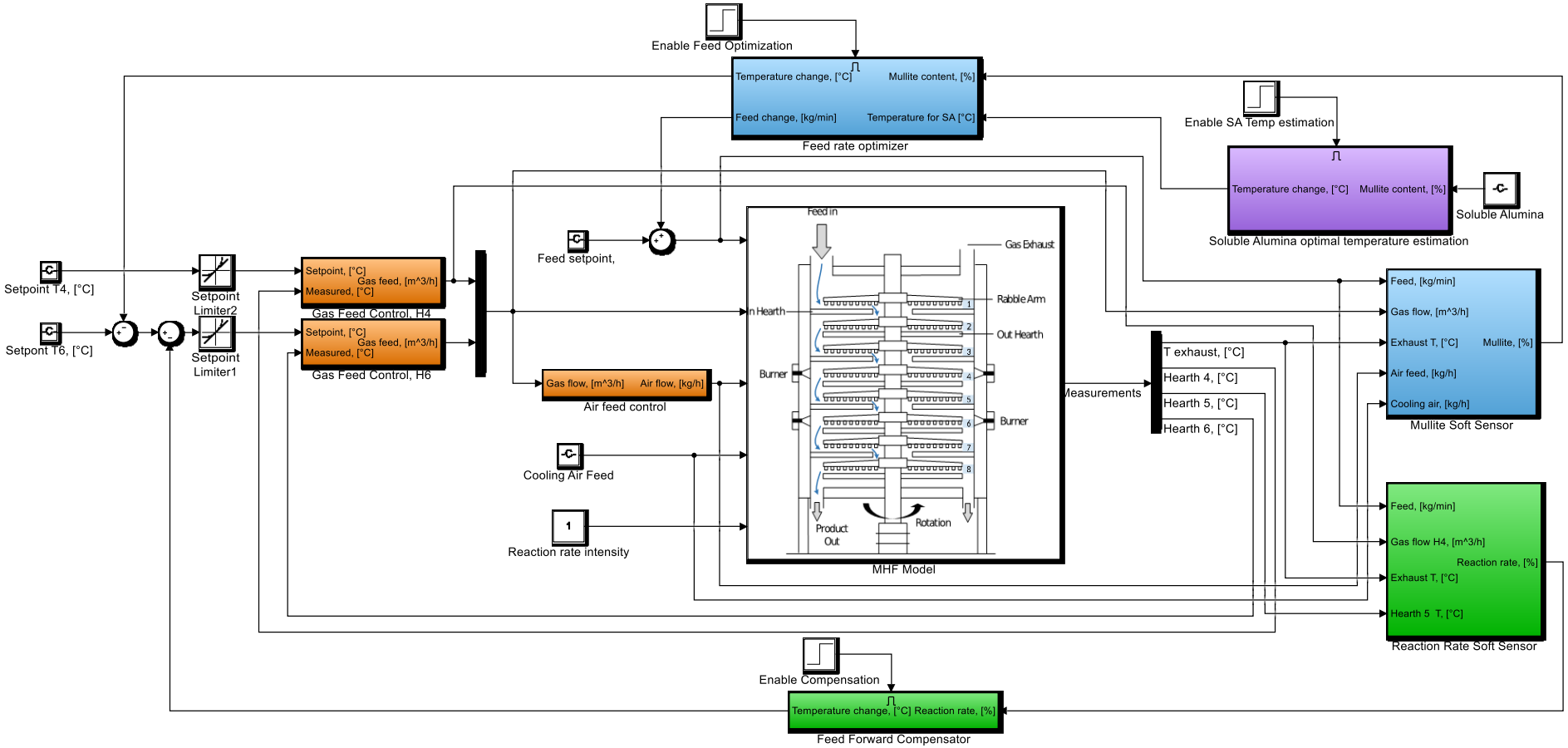

Figure 6.6 Simulation environment of the control strategy. Blocks responsible for the basic control level are denoted in orange. The green blocks are related to the stabilizing level. The optimizing level is presented in blue.

6.3 Simulation results of the basic temperature controller for the hearth 4

The hearth 4 of the MHF displays the BtoB phenomenon, which was discussed in Section 5.6. A recommended solution for the situation occurring in the hearth 4, is the implementation of a mean temperature controller (Gómez Fuentes, 2016). In the furnace, the current basic temperature control cannot regulate the temperature to 1000 °C due to the BtoB phenomenon, which was also discussed in Section 5.6. By using the total gas flow as an MV, the simulation results of the mean control are obtained, as illustrated in Figure 6.7. The setpoint of the mean temperature for the initial half of the simulation is 1000 °C; in the final half, the mean temperature setpoint is adjusted to 960 °C. The controlled variable follows the setpoint very accurately during the simulation. The top image of Figure 6.7 illustrates the progress of the temperatures of all burners during the simulation. Finally, the bottom graph of Figure 6.7 displays how one gas flow of four is performing to attain the desired control.

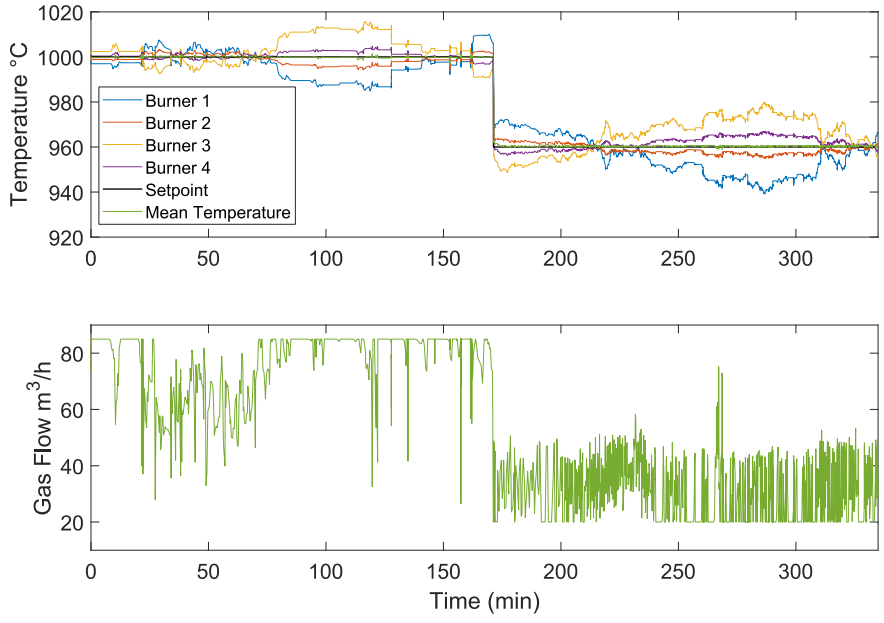

Figure 6.7 Simulation results of the temperature setpoint change for the hearth 4 mean temperature control.

The results of Figure 6.7 differ notably with the simulation results displayed in Figure 5.10 of Section 5.6. The mean temperature control

delivers a steadier temperature in the hearth 4 contrasted with the current control scheme and also reduces the effects of the BtoB phenomenon.

6.4 Simulation of feedforward control based on the reaction rate soft sensor

As discussed in Section 5.3, the reaction rate soft sensor can be implemented in combination with a feedforward control scheme aiming to minimize the energy use of the furnace.

The feedforward controller obtains the measurement of the reaction rate from the soft sensor as a conversion percentage from metakaolin to the "spinel phase" computed for the top part of the furnace (hearths 1–4).

Under normal operation, the spinel formation reaction happens in the hearth 6. Therefore, if a change in the reaction location occurs, then it would be indicated when the soft sensor measurements are higher than 40%. The feedforward control is enabled when the conversion increases to 40% or above, and the control is maintained active for 240 minutes in this simulation study. This control interval was adopted based on the maximum extent of the exothermic reaction, which was previously discussed in Section 5.3.

Figure 6.8 presents a comparison between the current control strategy and the designed feedforward control. The variables in the figure are as follows: reaction rate, total gas flow, the hearth 6 gas temperature, and the hearth 6 gas temperature setpoint. At a simulation time of 150 minutes, the rise of the disturbance on the reaction rate can be clearly observed, which increased from approximately 25% to 40% until the end of the simulation. In contrast, the reaction conversion decreased when the feedforward control was enabled, and the value was restored to approximately 20%. The current control (without feedforward) did not show changes from its setpoint of 1080 °C, being unable to respond to the increase in the reaction rate. In comparison, the feedforward control

showed a control action at a simulation time of 170 minutes in due to the rise in conversion above 40%, thus decreasing the temperature setpoint to 1062 °C. In the current control simulation, the gas consumption exhibited a reduction of 1.6% after the disturbances affected the process, whereas the feedforward control indicated that energy savings could be near 3.6% (Jämsä-Jounela *et al.*, 2018).

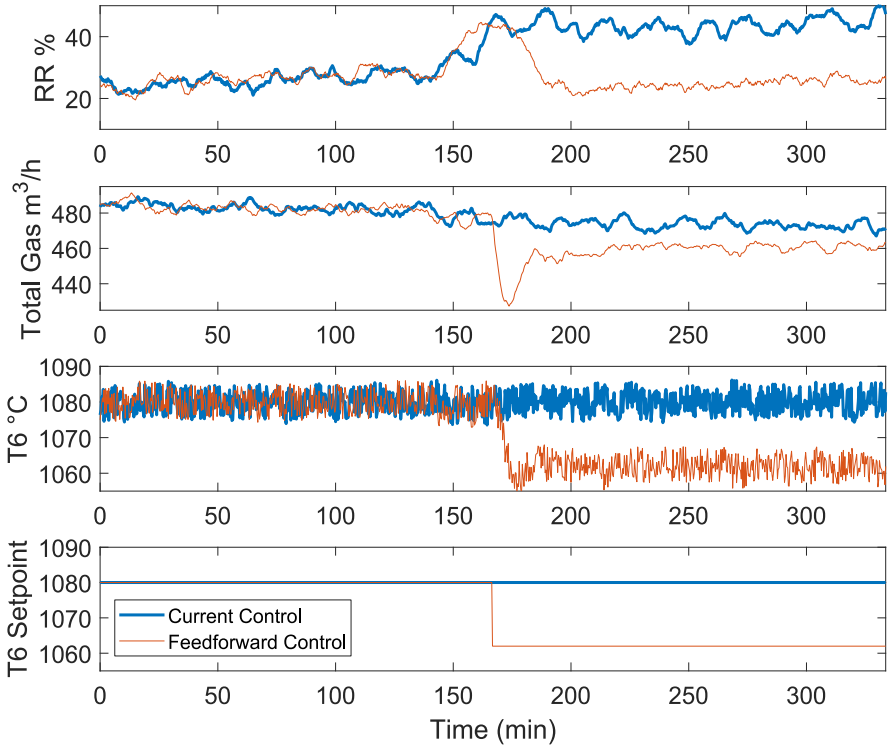

Figure 6.8 Comparison of the plant current control strategy (blue) vs. the feedforward control (orange).

6.5 Simulation of feed rate optimization based on the mullite content soft sensor

To evaluate the strategy presented in Chapter 6, the control scheme was implemented in the simulation environment. Initially, the furnace was operated at the designated operating conditions presented as follows: the feed rate was 83.33%, the hearth 6 temperature was 1100 °C, and mullite content was 16%. The mullite soft-sensor output used a moving average filter with a time window of 30 minutes. The aim was to maximize the capacity of the furnace and to maintain the mullite content at approximately 4% by reducing the temperature setpoint in the hearth 6. The control interval in the optimization level was defined as 6 hours based on the time the model requires to reach the steady-state, while the

feed rate change was set to a maximum of 5% during that time. Using the filtered mullite content measurement, the strategy calculates the optimal setpoint for the capacity and the temperature in the hearth 6 (Jämsä-Jounela *et al.*, 2018).

Figure 6.9 illustrates that the capacity optimization strategy maximized the feed rate in this simulation study, from 83.33% to 95.83%, and the hearth 6 setpoint temperature was dropped by 43 °C during the simulation. The top of Figure 6.9 indicates that there is a small variance between the MHF dynamic model output, and the soft-sensor estimate. However, the difference was assumed to be moderately minor and can be understood due to the steady-state nature of the soft-sensor calculations.

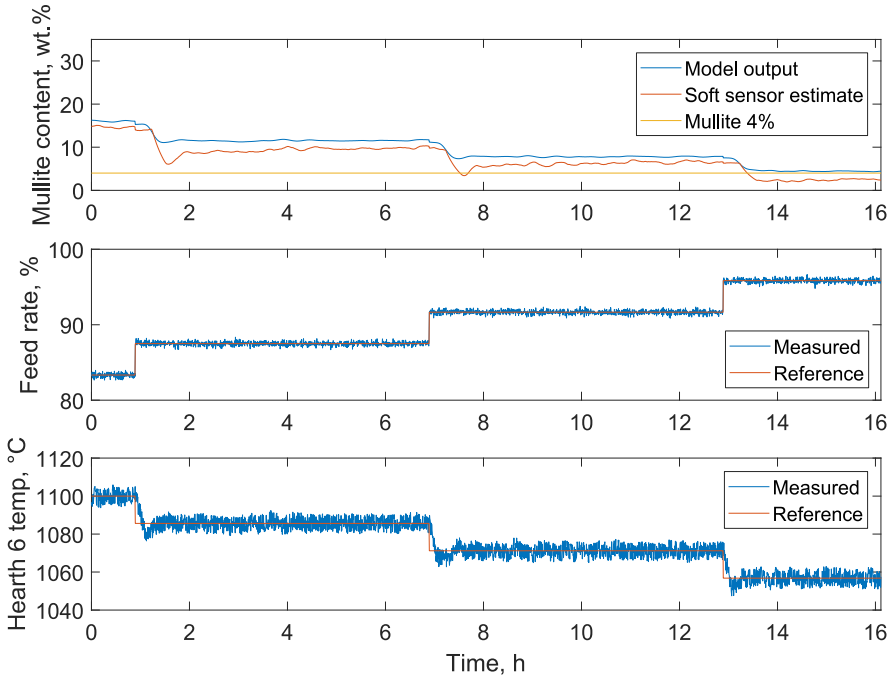

Figure 6.9 Simulation of capacity optimization.

Figure 6.10 presents a more comprehensive image of the furnace temperature profiles for the solid and gas phases. During the simulation, the spinel formation reaction is repositioned to following volumes in the hearth 6 as time progressed. This produced a delay in the mullite formation reaction which decreased its quantity in the final product. Furthermore, the proposed strategy inhibits the unnecessary heating of the material. The dashed lines show the temperature range for the spinel formation reaction according to Equation (2.3). Moreover, the results

validate the process energy savings as the gas temperature are reduced in the hearths 5 and 6. In addition, the temperature of the gases varied in accordance to the specified hearth 6 setpoint. An identical behavior is observed in the hearth 5. Consequently, the capacity optimization strategy maximizes the feed rate of the plant and minimizes the energy consumed in the calciner.

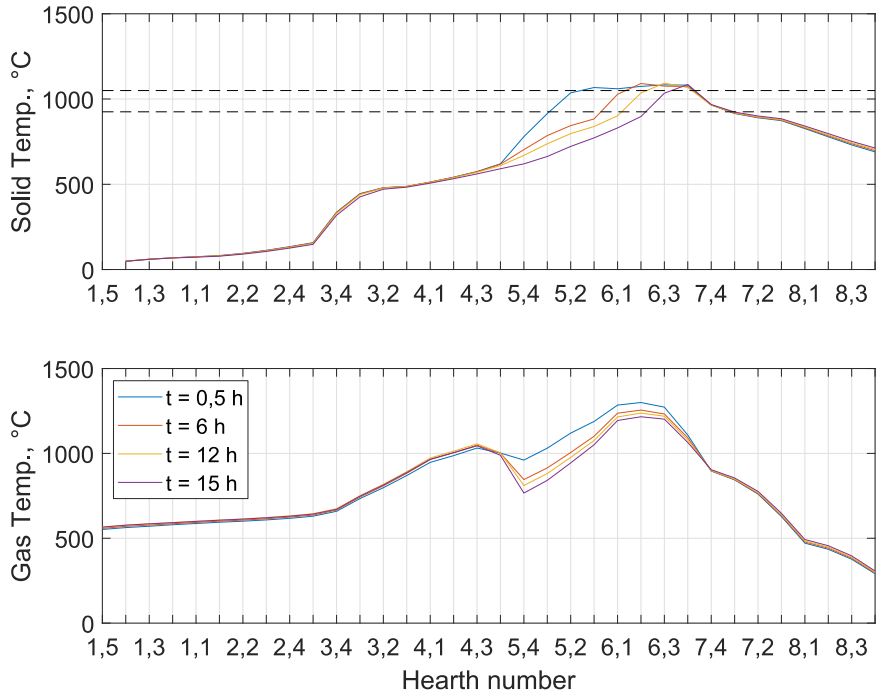

Figure 6.10 Temperature profiles of gas and solid phases in the furnace at selected time instances. The hearth number is denoted by two numbers: the first is the hearth and the second is the specific volume in that hearth.

Summary

The mineralogy-driven control strategy of the MHF has been defined in this chapter. The strategy has been focused on three objectives: (1) capacity maximization, (2) energy use minimization and (3) quality regulation. The simulation results have shown promising results, increasing the energy savings of the furnace and maximizing the capacity while maintaining the desired mullite content in the product. Based on these results, the enhanced control will be tested in the real plant, which will be discussed in the next chapter.

7. Plant testing of the soft sensors and the control strategy logic of the MHF

The control logic of the multiple hearth furnace was evaluated by industrial testing and the economic performance reported. First, the soft sensors were tested online by implementing the algorithms on a computer connected to the plant automation system. Second, a sampling and data collection campaign was performed to gather measurements from the calciner. Finally, the logic of the control concept was evaluated and validated using the data collected during the sampling campaign.

7.1 Description of the industrial testing environment

The industrial testing environment was set up to test the soft sensor software and the control strategy logic. The software was installed on a DELL laptop (Latitude E7450), which was then connected to the local area network of the plant. An Open Platform Communications (OPC) client was developed to read the real-time process data from the OPC server of the site distributed control system (DCS). The computers on the server and client side were configured according to the Distributed Component Object Model (DCOM) configuration document written by the OPC Foundation. On the other hand, the MHF soft sensor software also provided a manual data input interface to record and save the chemical testing data of the samples from the laboratory information management system (LIMS) data. The overall testing setup of the software is shown in Figure 7.1.

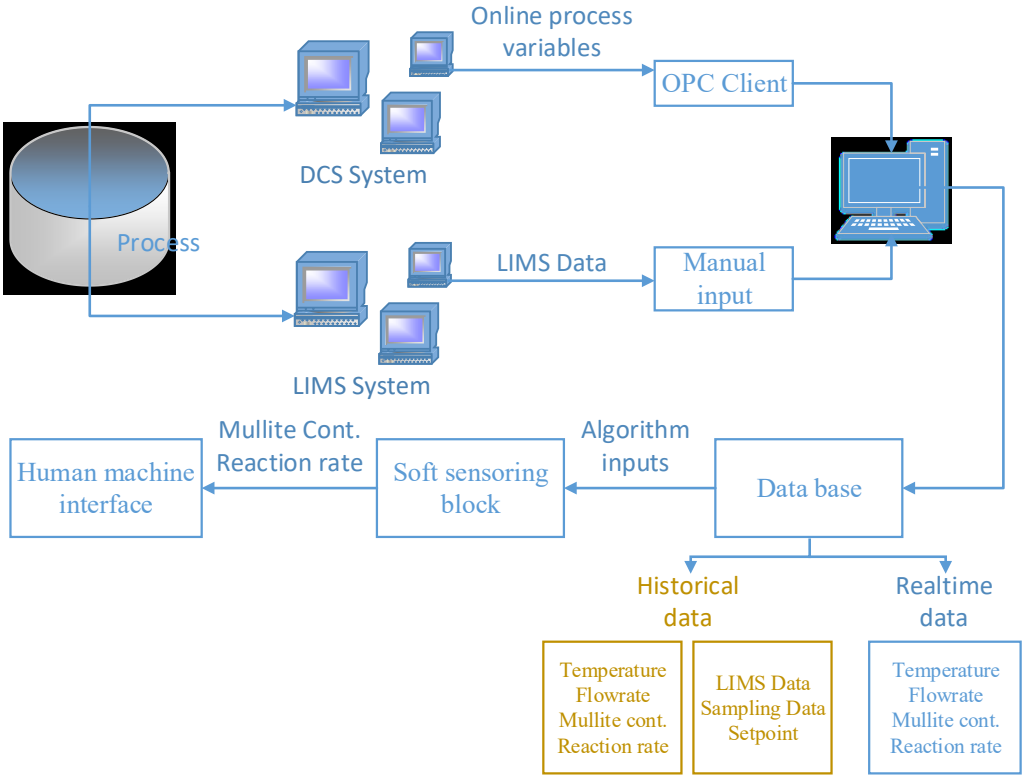

Figure 7.1 Soft sensor testing setup framework.

The soft sensor algorithms ran in the background to estimate the reaction rate and mullite content. The MHF soft sensor software was developed using Microsoft Visual Studio 2017. The main interface included the following features:

- Real-time key performance indicators: reaction rate, mullite content, burner flow rate, and feed rate.
- Temperature profile of the furnace.
- Real-time trends of the setpoints and actual values of T4 (temperature of the hearth 4), and the gas flow of burner 4.
- Real-time trends of the setpoints and actual values of T6 (temperature of hearth 6), and the gas flow of burner 6.
- Real-time trends of the feed rate, mullite content, and reaction rate.
- Three day curve of brightness (Vio) in the feed and product.

The main interface integrates the essential indexes of MHF production. The testing improved the quality and usability of the MHF soft sensor

software (Figure 7.2). Furthermore, it helped the operators to better follow the operating conditions of the MHF.

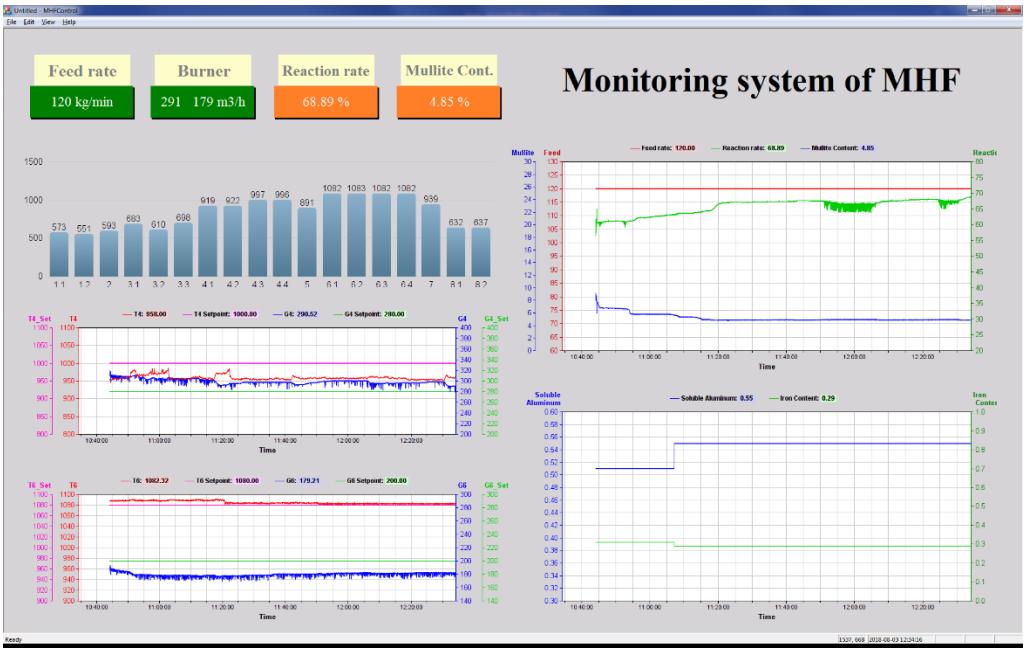

Figure 7.2 Main interface of the MHF soft sensor software.

7.2 Sampling campaign at the plant

The sampling campaign was performed from August 6th to 10th, 2018 at the factory to support the development of the MHF control strategy. The samples from the feed material and the calcined product of the MHF were collected for four days, for every hour from 10:00 to 16:00 h.

The assays needed for the input of the furnace (feed material) were the brightness, iron content, particle size, and moisture. Furthermore, the analyses for the output of the furnace comprised the brightness, particle size, and moisture. The analyses for the final product comprised the brightness, particle size, mullite, and soluble alumina. The samples were taken hourly, by considering the process delays for the feed, furnace, and product. The performed analyses on the samples and equipment are presented in Table 7.1, including the X-ray fluorescence (XRF) for determining the iron content; X-ray diffraction to quantify the mullite content; and inductively coupled plasma atomic emission spectroscopy to measure the soluble alumina.

Table 7.1 Analysis techniques and equipment.

Parameter	Technique	Equipment used
Particle size	Sedigraphy	Sedigraph III Plus
Iron content	XRF	X–Supreme 8000
Brightness	Spectrometer	Datacolor ELREPHO
Mullite	XRD	Panalytical Expert Pro XRD Spectrometer
Soluble Alumina	IMERYS internal method	ICP-AES

7.3 Testing results of the soft sensors and the control strategy

The aim of this section is to study the soft sensors' operation in real-time, as well as the control strategy logic based on the process data and sampling campaign results of the plant. The logic is analyzed following the dynamic behavior of the furnace. Finally, a discussion of the possible improvements of the enhanced control logic to the process is presented.

7.3.1 Soft sensors

During the testing period of the soft sensors, the plant's dynamic behavior was followed using online process measurements and the soft sensor software. Data from August 8th to 10th 2018, were used to illustrate the results of the reaction rate, mullite content, and soluble alumina soft sensors.

Figure 7.3 shows the calculations of the soft sensors and laboratory results of the samples obtained during the sampling campaign on August 8th, 2018. The reaction rate oscillated between 10 and 30% until 14:00 hours, when it rose to approximately 40%. The mullite content laboratory results showed a significant variation during the day with a minimum of 4% and a maximum of 13%. From the same figure, it can be seen that the soft sensor for mullite content followed the general trend exhibited by the corresponding laboratory results. The soluble alumina content was generally low with assays of ≤0.3 wt.% observed during the day. Finally, the product brightness was relatively low, but displayed an increasing trend in the range of 88.7–89.

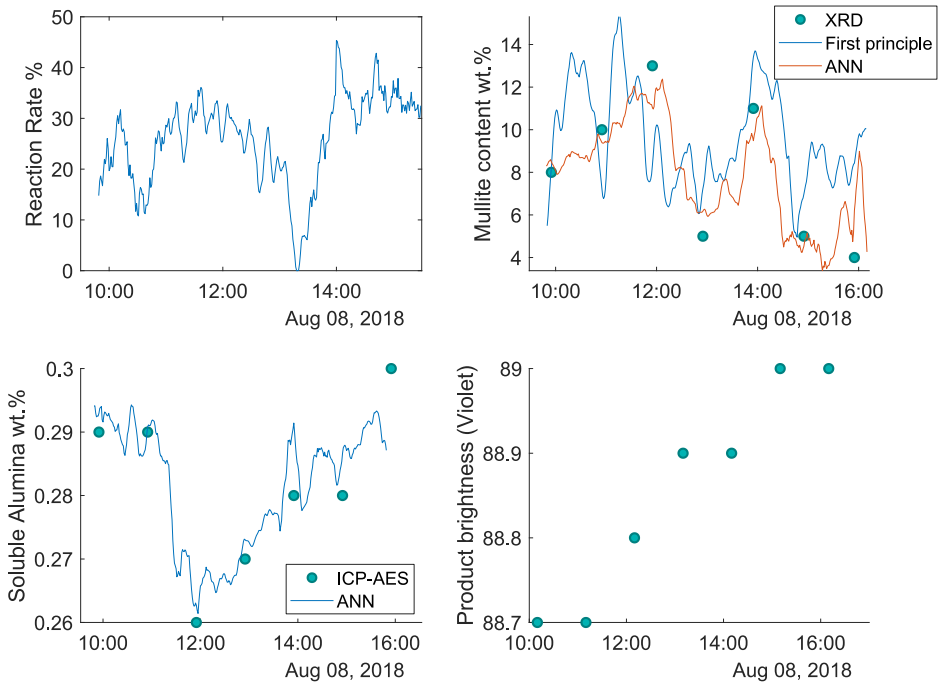

Figure 7.3 Soft sensors and lab results during the testing campaign on August 8th, 2018 (Gómez Fuentes *et al.*, 2019).

In contrast, Figure 7.4 presents the results of the soft sensors and analytical laboratory assays of the samples obtained during the sampling campaign on August 9th, 2018. It can be observed that the reaction rate oscillated between 30% and 40% with a maximum attainment of 51%. The laboratory results for the mullite content exhibited a significant variation during the day with noted minimum and maximum values of 4% and 14% respectively. The results obtained from the first principle mullite soft sensor were comparable to the analytical laboratory results, with notable deviations due to the spinel formation reaction occurring earlier than expected. The deviations were particularly high when the reaction rate reached its peak value. The ANN mullite soft sensor showed greater accuracy compared to the first principle soft sensor. The content of the soluble alumina was relatively similar to that of the previous day with values in the 0.27–0.32wt.% range observed with the ANN soft sensor exhibiting excellent estimation reliability. The product brightness had an average value of 88.9 and maximum value of 89.

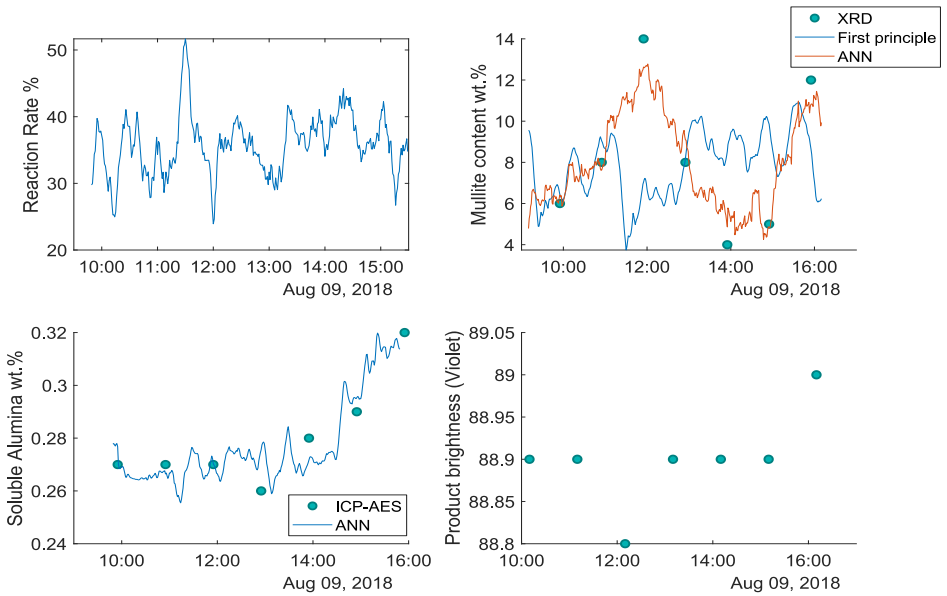

Figure 7.4 Soft sensors and lab results during the testing campaign on August 9th, 2018.

As illustrated in Figure 7.5, the reaction rate oscillated between 15% and approximately 40% with values greater than 30% for the last 2 hours of the day. According to the XRD results, the mullite content varied between 4% and 14%, which was similar to the previous day. The performance of the first principle mullite soft sensor was moderately accurate, while the ANN soft sensor performed excellently. The behavior of the soluble alumina content was comparably similar to that of the previous days, with measured values in the range of 0.26–0.32wt.%. The ANN soft sensor performed fairly well. Finally, the product brightness for this day had a mean value of 89 with a maximum value of 89.2, the highest observed in the testing period.

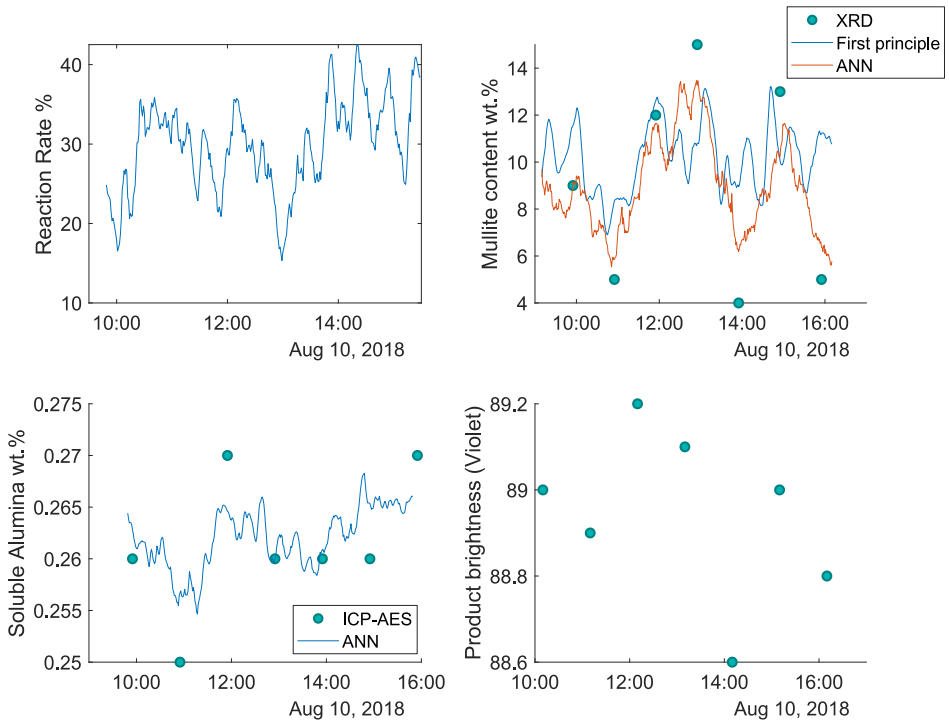

Figure 7.5 Soft sensors and lab results during the testing campaign on August 10th, 2018.

7.3.2 Control logic

The control logic presented in Chapter 6 was evaluated using the process data from August 8th to 10th 2018. On August 8th, the reaction rate presented a low value in general with fluctuations originating from the limitations of the temperature control in the hearth 4 due to the BtoB phenomenon, as shown in Figure 7.3. The mullite content showed a high value (above 5 wt.%) during most of the day, implying that the temperature in the furnace was higher than necessary, also indicated by the low soluble alumina content (below 0.50 wt.%). In this situation, the enhanced control strategy could drive the process to a more efficient operating condition by increasing the capacity at the beginning of the day (10:00 h) while maintaining the same energy consumption. This new operating condition would reduce the mullite content significantly in the product, while maintaining the required specifications of brightness and soluble alumina. The following day (August 9th), the reaction rate presented a few fluctuations due to the temperature control in the hearth 4, as depicted in Figure 7.4. Similar to the previous day, the mullite content showed a high value (above 5 wt.%) during most of the day with some periods of low content, as the temperature in the furnace was above

the necessary value. Although the process was running at maximum capacity, by following the enhanced control strategy logic and decreasing the overall temperature, the mullite formation could be reduced and the energy efficiency improved. On the final day (August 10th), the reaction rate was below 40% and the mullite content presented large fluctuations due to the high-temperature furnace operation, as illustrated in Figure 7.5. Similar to the previous case (August 9th), the process could be significantly improved based on the control logic by minimizing the mullite content and reducing the furnace temperature, while attaining the desired quality constraints. Essentially, the general operation of the furnace would be improved by implementing the new control concept, thus maximizing the capacity and reducing the energy consumption.

Summary

An industrial testing for validation of the enhanced control strategy has been documented in this chapter. The soft sensors have been implemented and tested online, and the control strategy's possible process improvements have been studied using the collected plant data. The results have been positive, showing good opportunities in the real plant implementation. The next chapter will introduce the concept of model predictive control and the implementation of this advanced control strategy to the MHF.

8. Studies on Model Predictive Control for the multiple hearth furnace

This Chapter studies the applicability of Linear MPC for the MHF control strategy presented in Chapter 6. The aim is to decrease the temperature interactions in the control between the burner zones of the furnace. First, an introduction to Model Predictive Control is presented. Next, the design of the MPC framework for the MHF in kaolin calcination is described. Furthermore, the linear model of the MHF for MPC is defined and the simulation environment described. Next, this chapter presents the simulation results, which are analyzed and discussed. Additionally, an analysis of the comparison between Linear MPC and PI control scheme for temperature control is discussed. Finally, an outline of the future work to implement Nonlinear MPC and Economic MPC into the MHF is presented.

8.1 Introduction to MPC

Model Predictive control is an advanced process control strategy, which uses a model to foresee the future response of a process and introduce the suitable corrective control actions that lead the process to the desired state. In general, the aim of MPC is to direct the selected output variables to their respective reference points, while violations of the input and output restrictions are prevented (Richalet, 1993). In addition, MPC focuses on preventing the unnecessary variation of the input variables and to control the maximum number of process variables as possible even when a sensor is not accessible (Rawlings and Mayne, 2009).

MPC algorithms may vary from one another but comprise the following common essentials aspects (Camacho and Bordons, 1999): a prediction

model, an objective function and the algorithms to find the control law. Opting for different choices of these aspects, enables the design of different MPC implementations.

8.1.1 Process and Disturbance Models

The most important element of MPC is the process model, which defines the connection between the input and the output variables of a process. In addition, a disturbance model can be included to implement a state estimator or to introduce a plant model mismatch. Numerous MPC designs employ various types of process models (Huang and Kadali, 2008); the most frequently used are as follows.

- Impulse response model
- Step response model
- Transfer function model
- State-Space model

8.1.1.1 State-Space model

The following equations describe the linear state-space model:

$$x_{t+1} = Ax_t + Bu_t \quad (8.1)$$

$$y_t = Cx_t + Du_t \quad (8.2)$$

The state-space models include the following advantages:

- Multivariable processes are defined in an identical way as single input/single output (SISO) dynamics.
- Modern analysis methods and control theory, including the Kalman filter, may be applied effortlessly to state-space models.

One disadvantages of state-space models is that processes with limited number of states may not be described adequately by a state-space model.

8.1.1.2 Time series model for the disturbance

A commonly employed disturbance model is the autoregressive integrated moving average (ARIMA) model, where the disturbance, is described by the following equation (Camacho and Bordons, 1995):

$$d_t = \frac{C(z^{-1})}{\Delta D(z^{-1})} e_t \qquad (8.3)$$

where d_t is the disturbance, the symbol Δ denotes $1-z^{-1}$, e_t is the white noise, and C and D are polynomials usually designated to be 1.

8.1.2 Multiple-step prediction

In MPC, the process model is adopted as the predictor of the future plant behavior, and afterward the control law is formulated using the predictor. Based on multiple-step predictions, the future input movements of the process are designated to direct the process outputs to the desired values. In the following equations, the multiple-step prediction is presented in more details.

The considered model for prediction is simple, which is a moderate alteration of the conventional ARX model. The model includes the term Δu_t instead of u_t:

$$y_t = -ay_{t-1} + b\Delta u_{t-1} + e_t \qquad (8.4)$$

The one-step prediction is formulated by taking the model equation at time instant $t+1$

$$y_{t+1} = -ay_t + b\Delta u_t + e_{t+1} \qquad (8.5)$$

If the white noise is omitted, then presenting the previous equation in prediction terms gives the following result:

$$\hat{y}(t+1|t) = -ay_t + b\Delta u_t \qquad (8.6)$$

Where $\hat{y}(t+1|t)$ is the expected value of y_{t+1} with available information at instant t.

Next, to find the two-step prediction, the modeling equation is calculated at the time instant $t+2$:

$$y_{t+2} = -ay_{t+1} + b\Delta u_{t+1} + e_{t+2} \qquad (8.7)$$

Substituting Equation *(8.5)* in *(8.7)*:

$$\begin{aligned} y_{t+2} &= -a(-ay_t + b\Delta u_t + e_{t+1}) + b\Delta u_{t+1} + e_{t+2} \qquad (8.8) \\ &= a^2 y_t + b\Delta u_{t+1} - ab\Delta u_t - e_{t+1} + e_{t+2} \end{aligned}$$

Then, the two-step prediction is found by omitting the unknown future noise values:

$$\hat{y}(t+2|t) = a^2 y_t + b\Delta u_{t+1} - ab\Delta u_t \tag{8.9}$$

Finally, combining Equations (8.*6*) and (8.*9*), the one-step and two-steps prediction is found based on the previous input-output and the future input data:

$$\begin{pmatrix}\hat{y}(t+1|t)\\ \hat{y}(t+2|t)\end{pmatrix} = \begin{pmatrix}-a\\ a^2\end{pmatrix} y_t + \begin{pmatrix}b & 0\\ -ab & b\end{pmatrix}\begin{pmatrix}\Delta u_t\\ \Delta u_{t+1}\end{pmatrix} \tag{8.10}$$

The derivation of predictions over further steps may be found in a analogous way, which is defined in the next Section 8.1.2.1. Likewise, the same idea of substitution can be used on other models to find the multiple-step predictions.

8.1.2.1 Prediction with the state-space models

State-space models allow multiple-step predictions by reintroducing recurrently the one-step prediction equation (Rossiter, 2004):

$$\begin{aligned} x_{t+1} &= Ax_t + Bu_t \\ y_{t+1} &= Cx_{t+1} \end{aligned} \tag{8.11}$$

For $t+2$:

$$\begin{aligned} x_{t+2} &= Ax_{t+1} + Bu_{t+1} \\ y_{t+2} &= Cx_{t+2} \end{aligned} \tag{8.12}$$

Substituting Equation (8.*11*) into (8.*12*):

$$\begin{aligned} x_{t+2} &= A^2 x_t + ABu_t + Bu_{t+1} \\ y_{t+2} &= Cx_{t+2} \end{aligned} \tag{8.13}$$

Then reiterating the substitution for $t+3$:

$$\begin{aligned} x_{t+3} &= A^2[Ax_t + Bu_t] + ABu_{t+1} + Bu_{t+2} \\ y_{t+3} &= Cx_{t+3} \end{aligned} \tag{8.14}$$

Next, for the k-step prediction:

$$\begin{aligned} \hat{x}(t+k|t) &= A^k x_t + A^{k-1}Bu_t + A^{k-2}Bu_{t+1} + \cdots + Bu_{t+k-1} \\ \hat{y}(t+k|t) &= C[A^k x_t + A^{k-1}Bu_t + A^{k-2}Bu_{t+1} + \cdots + Bu_{t+k-1}] \end{aligned} \tag{8.15}$$

The combination of the prediction equations may be written in matrix form for the prediction horizon N:

$$\underbrace{\begin{bmatrix}\hat{x}_{t+1}\\ \hat{x}_{t+2}\\ \hat{x}_{t+3}\\ \vdots\\ \hat{x}_{t+N}\end{bmatrix}}_{\substack{x\\ \rightarrow t+1}} = \underbrace{\begin{bmatrix}A\\ A^2\\ A^3\\ \vdots\\ A^N\end{bmatrix}}_{F_x} x_t + \underbrace{\begin{bmatrix}B & 0 & 0 & \cdots\\ AB & B & 0 & \cdots\\ A^2B & AB & B & \cdots\\ \vdots & \vdots & \vdots & \vdots\\ A^{N-1}B & A^{N-2}B & A^{N-1}B & \cdots\end{bmatrix}}_{H_x} \underbrace{\begin{bmatrix}u_t\\ u_{t+1}\\ u_{t+2}\\ \vdots\\ u_{t+N-1}\end{bmatrix}}_{\substack{u\\ \rightarrow t}} \tag{8.16}$$

$$\underbrace{\begin{bmatrix}\hat{y}_{t+1}\\ \hat{y}_{t+2}\\ \hat{y}_{t+3}\\ \vdots\\ \hat{y}_{t+N}\end{bmatrix}}_{\substack{y\\ \rightarrow t+1}} = \underbrace{\begin{bmatrix}CA\\ CA^2\\ CA^3\\ \vdots\\ CA^N\end{bmatrix}}_{F} x_t + \underbrace{\begin{bmatrix}CB & 0 & 0 & \cdots\\ CAB & CB & 0 & \cdots\\ CA^2B & CAB & CB & \cdots\\ \vdots & \vdots & \vdots & \vdots\\ CA^{N-1}B & CA^{N-2}B & CA^{N-3}B & \cdots\end{bmatrix}}_{H} \underset{\rightarrow t}{u} \qquad (8.17)$$

Finally, the prediction for the state-space model of Equation (8.*11)* is defined as:

$$\begin{aligned} \underset{\rightarrow t+1}{x} &= F_x x_t + H_x \underset{\rightarrow t}{u}\\ \underset{\rightarrow t+1}{y} &= F x_t + H \underset{\rightarrow t}{u} \end{aligned} \qquad (8.18)$$

8.1.2.2 The free and forced response

The *free* and *forced* response concepts are normally employed in diverse MPC algorithms. The main objective is to present the control sequence as the summation of two signals:

$$u_t = u_f(t) + u_c(t)$$

where $u_f(t)$ is a signal consistent with the previous inputs and is kept constant (identical to the preceding value) in the future:

$$u_f(t-k) = u(t-k) \text{ for } k = 1,2,\ldots$$

$$u_f(t+k) = u(t-k) \text{ for } k = 0,1,2,\ldots$$

For $u_c(t)$, the previous values are made equal to zero, and the subsequent time instants are defined as the next control move in the future:

$$u_c(t-k) = 0 \text{ for } k = 1,2,\ldots$$

$$u_c(t+k) = u(t+k) - u(t-1) \text{ for } k = 0,1,2,\ldots$$

The *free* response $y_f(t)$, is the estimate of the process output when the manipulated variable is identical to $u_f(t)$; and the *forced* response $y_c(t)$ is the estimate of the process output when the control sequence equal to $u_c(t)$. Specifically, the *free* response defines the behavior of the process if there are no variations in the manipulated variable for the current state; while the *forced* response defines the behavior of the process due to the future control sequence.

8.1.3 Objective Function and Constraints

MPC algorithms employ various types of cost functions to get the control law (Carlson *et al.*, 1991). These algorithms utilize the objective function to guarantee that the output variables follow a specified reference setpoint in the future until the defined prediction horizon. Therefore, a general equation for the objective function is shown as follows:

$$J = \sum_{i=N_{min}}^{N_{max}} [r_{t+i} - \hat{y}(t+i|t)]^T Q_i [r_{t+i} - \hat{y}(t+i|t)] + \sum_{i=N_{min}}^{N_c} [\Delta u_{t+i-1}]^T R_i [\Delta u_{t+i-1}] \quad (8.19)$$

The parameters N_{min} and N_{max} represent the minimum and maximum prediction horizons. N_c denotes the control horizon and may vary from N_{max}. These parameters state the interval when the reference trajectory is optimal. Thus, if a high value is defined for the N_{min}, then past errors are less important. If the process features a dead time d, then N_{min} must be a greater value than $t + d$. In some cases, when the process has an inverse response, this behavior may be neglected from the objective function. Q_i and R_i symbolize the weighting matrices.

The reference trajectory (r_t) is the wanted direction that the process must follow. Although it is favored that the process output will attain the setpoint with no errors, there could be variances with the final process output due to time delays, model mismatch or some hard constraints. Generally, the reference trajectory is a smooth curve commencing from the current value of the output is used to approach the setpoint.

Typically, processes are limited to physical and other types of constraints. For example, actuators require specific limitations that avert them from moving beyond their physical limits. Other constraints are enforced due to safety and economic reasons. For instance, a chemical reaction may be benefited at high temperatures, but the reactor may have a certain threshold which should not be exceeded, due to safety reasons

and material tolerance. In practice, MPC integrates constraints, which has proven to be successful in industry. A general definition of constraints is presented as follows:

$$\begin{aligned} u_{min} \leq \quad & u_t \quad \leq u_{max} \quad && \forall t \\ du_{min} \leq u_t - u_{t-1} & \leq du_{max} && \forall t \\ y_{min} \leq \quad & y_t \quad \leq y_{max} && \forall t \end{aligned} \tag{8.20}$$

The inclusion of constraints to the optimization problem complicates the solution procedure. However, this allows MPC to control the process while following the restrictions existing on a specific application.

8.1.4 Control Law

The process inputs or control actions Δu_{t+i}, are obtained by solving the optimization problem. In order to reach this goal, the output prediction $\hat{y}(t+1|t)$ is estimated, for instance as defined in Equation (8.*10)*, and then utilized to evaluate the objective value according to Equation (8.*19)*. Then, a derivative of the cost function is calculated with respect to Δu_t, Δu_{t+1},..., Δu_{t+N_c-1}. Finally, the solution of the optimization problem is obtained by setting the derivatives to zero. By following this algorithm, it is possible to find an analytical solution.

If some constraints exist on the process variables u_t, Δu_t, or $\hat{y}(t+1|t)$, then analytical solutions are not possible to obtain, and a numerical minimization method is needed. It is essential to consider that all these computations occur within the sampling time interval of the controller.

8.2 Linear MPC formulation for the MHF

This subsection presents the formulation of the Linear MPC for the MHF. First, the definition of the transfer function model for the MHF is described, followed by, the simulation environment and the MPC framework for the MHF. Furthermore, this subsection illustrates the results of the simulation. Finally, the Linear MPC and the PI control scheme are compared, and the results are discussed.

8.2.1 Description of the transfer function model for the MHF

To design the MPC controller, a linear time-invariant transfer function model of the process is identified from step tests from the nonlinear model (Eskelinen *et al.*, 2015) described earlier in Chapter 4. MATLAB's Identification Toolbox facilitated the process of identifying the transfer function model. The input variables for the model identification are the furnace feed rate and the gas flows to the hearths 4 and 6. The gas temperatures of the hearths 4 and 6 were selected as the output variables to design a simple model for the MPC framework which preserves the dynamic behavior of MHF. The identification variables were standardized using the Equation (5.11) to eliminate dimensionality effects while maintaining the dynamic response of the process. The response of the gas temperature to the step changes is illustrated in Figure 8.1 and the sequence of step changes to the feed rate and gas flows is presented in Figure 8.2.

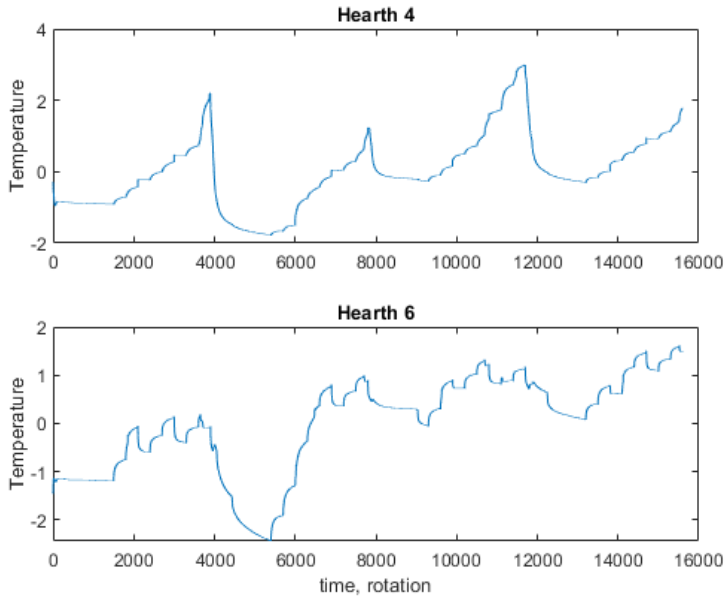

Figure 8.1 Responses of the Temperature in the hearth 4 and 6 to input changes in feed rate and gas flows.

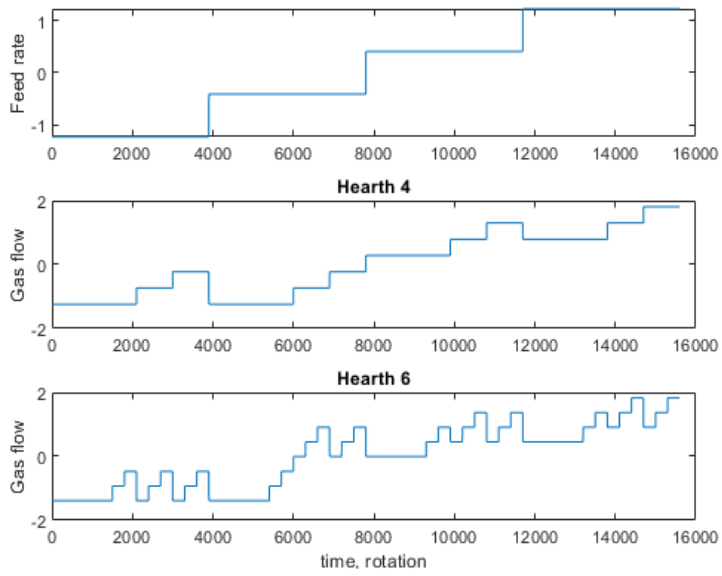

Figure 8.2 Step input sequence.

The identification data was separated in training and validation sets of 75% and 25% respectively and the result shows a correlation coefficient R^2 of 0.9534. The structure of the identified model is presented as the following transfer function:

$$y_{cv}(s) = G_p u_{mv}(s) + G_d u_d(s) \qquad (8.21)$$

where, with respect to the Laplace domain, y_{cv} represents the controlled variables, gas temperatures of the hearths 4 and 6 ($[T_{H4}(s),\ T_{H6}(s)]$); u_{mv} represents the manipulated variables, gas flows of the hearths 4 and 6 $[F_{H4}(s), F_{H6}(s)]$. The feed rate $u_d = F_K$ represents the measured disturbance variable. The plant and disturbance models in the Laplace domain are:

$$G_p(s) = \begin{bmatrix} \frac{1.522}{101.2s+1} & \frac{0.5125}{79.26s+1} \\ \frac{0.6928}{116.1s+1} & \frac{0.9869}{74.63s+1} \end{bmatrix}; G_d(s) = \begin{bmatrix} \frac{-1.28e^{-30s}}{121.8s+1} \\ \frac{-0.7519e^{-62s}}{171.7s+1} \end{bmatrix} \qquad (8.22)$$

Note, the time delay between F_{H4} and T_{H6} or F_{H6} and T_{H4} is regarded as negligible due to the fast dynamics of the gas phase (Eskelinen *et al.*, 2015).

8.2.2 Description of the simulation environment for the MPC framework

The simulation environment developed in this section is designed in MathWorks™ MATLAB®. This software contains a fourth-generation programming language, which comprises matrix calculations, execution of algorithms, interconnection with other programs, and visualization of diverse data, among others. MATLAB is largely used in research and academic institutions, as well as in industry, due to its fast processing, ease of access, and reliability.

The overview of the simulation environment is shown in Figure 8.3. The model presented in Equation *(8.22)* is used to simulate the actual process behavior. The model receives the gas flow rates to the hearths 4 and 6 from the MPC controllers and the feed rate is input externally as the measured disturbance. The temperature profile estimated by the model and the gas flow rates to the hearths 4 and 6 are passed to the Kalman filter to approximate the current state of the furnace. The linear model is utilized in the MPC optimization for the prediction of the furnace response.

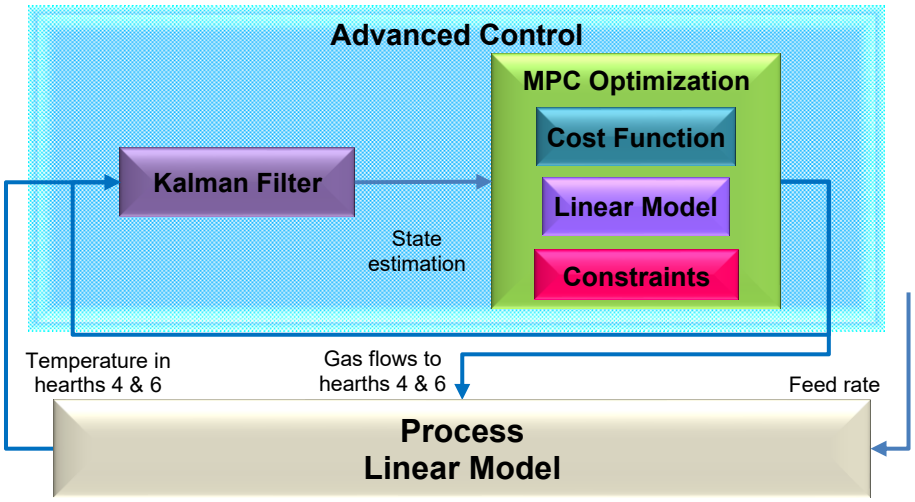

Figure 8.3. Simulation environment for the MPC framework.

The optimization problem is solved, by forecasting the states using the linear model and computing the optimal gas flows for the hearths 4 and 6, through the solution of the optimization problem in Equation (8.*23*):

$$\min_{u_{mv}} J = \sum_{i=1}^{N_p} \left\| y_t^{sp} - y_t^{cv} \right\|_Q + \sum_{i=1}^{N_c} \| \Delta u_t^{mv} \|_R$$

$$\begin{cases} x_{t+1} = Ax_t + B_1 u_t^{mv} + B_2 u_t^d \\ y_t = Cx_t + D_1 u_t^{mv} + D_2 u_t^d \end{cases} \qquad (8.23)$$

$$F_{H4} \in [137, 270] mol/min$$

$$F_{H6} \in [65, 170]\ mol/min$$

$$\Delta F_{H4}, \Delta F_{H6} \in [-3.49, 3.49]\ mol/min$$

where y_t^{sp} is the controlled variable set-point trajectory, N_p is the prediction horizon, N_c is the control horizon. The prediction horizon was chosen such that it ranges past the residence time of the furnace, i.e., $N_p = 45$ minutes. A suitable balance between controller aggression and computational effort was obtained by tuning the control horizon to $N_c = 24$ minutes. $u_t^{mv} = [F_{H4}, F_{H6}]$ represents the manipulated variables (gas flows to hearths 4 and 6), $y_t^{cv} = [T_{H4}, T_{H6}]$ represents the controlled variables (temperatures of hearths 4 and 6), $u_t^d = F_k$ is the measured input disturbance (feed rate), $\Delta u_t^{mv} = [\Delta F_{H4}, \Delta F_{H6}]$ is the rate of change for the manipulated variables. The linear model is represented in the state-space form to facilitate the implementation of the MPC paradigm. Additionally, the values of the process constraints are shown in Equation *(8.23)*.

Matrices Q and R in Equation *(8.23)* represent the weighting matrices for the output and input variables respectively. The output weighting matrix $Q = diag[q_1, q_2]$ is a diagonal matrix calculated to place greater emphasis on the regulation of T_{H6} than on T_{H4}. The reason is that the temperature in the hearth 6 has a greater impact on the quality of the final product (amount of unwanted mullite) than the temperature in the hearth 4. A 20% difference from the setpoint in T_{H4} should contribute the same error to the cost function as a 10% deviation from the setpoint in T_{H6}. The input weighting matrix $R = diag[r_1, r_2]$ is a diagonal matrix calculated to allow identical use of both inputs. A 10% change in half the ranges of F_{H4} and F_{H6} should give an equivalent contribution to the cost function. Furthermore, the contribution of R to the cost function is scaled

to produce a percentage (10%) of the error in J compared to Q (le Roux *et al.*, 2016). Therefore:

$$q_1\left(0.2T_{H4_{SP}}\right)^2 = q_2\left(0.1T_{H6_{SP}}\right)^2 = 0.1r_1\left(\frac{0.1F_{H4_{rng}}}{2}\right)^2 = 0.1r_2\left(\frac{0.1F_{H6_{rng}}}{2}\right)^2 \quad (8.24)$$

To guarantee integral action by the controller, the state vector for the state-space model in Equation *(8.23)* is estimated using a Kalman filter (Simon, 2006).

After solving the optimization problem, the manipulated variables are directed to the process to achieve the desired temperature setpoint. The following steps are executed at each sampling time of the simulation cycle:

1. Estimate the current state of the process (x).
2. Solve the MPC optimization problem defined by Equation (8.*23)*.
3. Apply the optimal value of the manipulated variables (u_{mv}) obtained from the MPC to the process model.
4. Simulate the process model for one sampling time.

8.2.3 Simulation results

This subsection presents a series of simulations to test response of the MPC with the MHF linear model. The tests include changes to temperature setpoints in the hearths 4 and 6, and variations in capacity levels. The positive and negative changes in the temperature of the hearths were 5 °C, and the capacity change was 3.49%. These values are within nominal setpoint variations during the normal operation of the furnace.

8.2.3.1 Setpoint changes to the temperatures in the hearths 4 and 6

Figure 8.4 and Figure 8.5 illustrate the simulation results of the MPC, with a temperature (hearth 4) setpoint increase by 5 °C after 3000 seconds. The initial temperature setpoint values are 990 and 1085 °C for the hearth 4 and 6 respectively, and the feed rate was kept at a value of

83.33%. The MPC shows excellent performance in maintaining the controlled variables near the setpoint values of the temperatures in the hearths 4 and 6. It is noticeable that the MPC controller begins to adjust the gas flows near simulation time of 1000 seconds due to the ability to track the setpoint change that occurs at 3000 seconds.

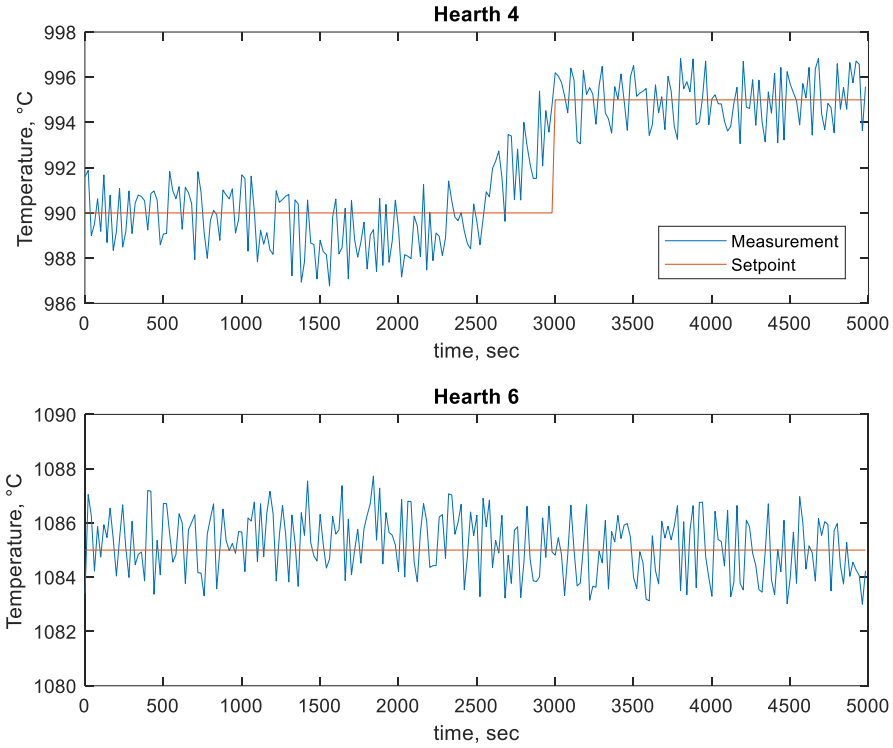

Figure 8.4 Setpoint change (+5°C) to the hearth 4, Controlled Variables.

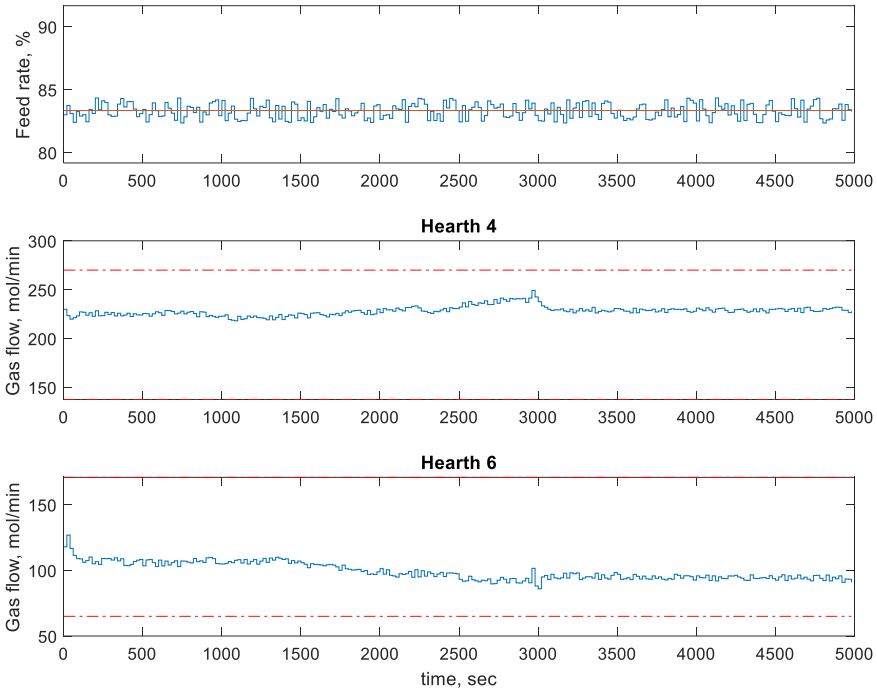

Figure 8.5 Setpoint change (+5°C) to the hearth 4, Feed rate and gas flows.

Figure 8.6 and Figure 8.7 depict the simulation results of the MPC, when the hearth 4 temperature setpoint was decreased by 5°C after 3000 seconds. The initial temperature setpoint values were 990 and 1085 °C for the hearths 4 and 6 respectively and the feed rate was maintained at a value of 83.33%. The MPC exhibits remarkable execution in regulating the controlled variables to the setpoint values of the temperatures in the hearths 4 and 6. Similarly to the previous case, the MPC controller begins to adjust the gas flows anticipating the setpoint that occurs at 3000 seconds.

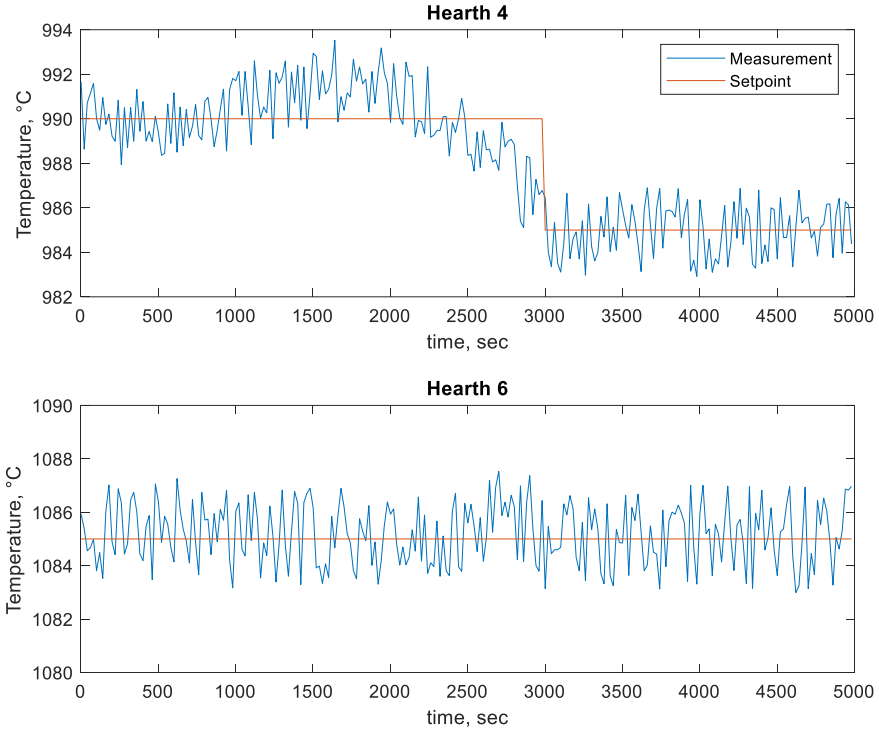

Figure 8.6 Setpoint change (-5 °C) to the hearth 4, Controlled Variables.

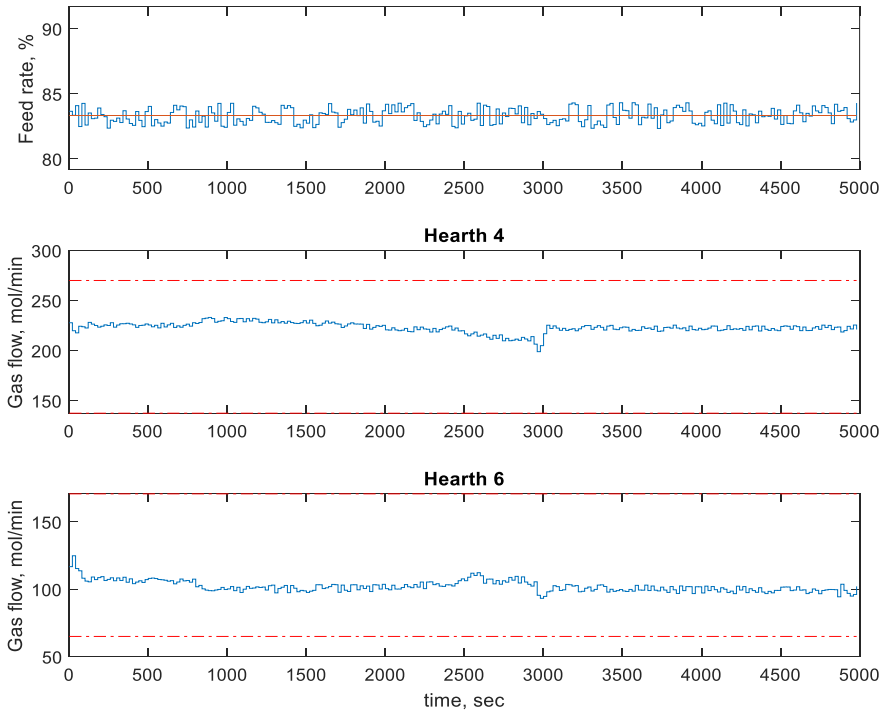

Figure 8.7 Setpoint change (-5 °C) to the hearth 4, Feed rate and gas flows.

The next case, presented in Figure 8.8 and Figure 8.9, shows the increase in the hearth 6 temperature setpoint by 5 °C after 3000 seconds. The simulation results of the MPC comprise the initial temperature setpoint values of 990 and 1085 °C for the hearth 4 and 6 respectively and the feed rate was kept at a value of 83.33%. The MPC displays excellent control in maintaining the variables to the setpoint values of the temperatures in the hearths 4 and 6. As in previous cases, the MPC controller anticipates the setpoint change that occurs at 3000 seconds and adjusts the gas flows accordingly.

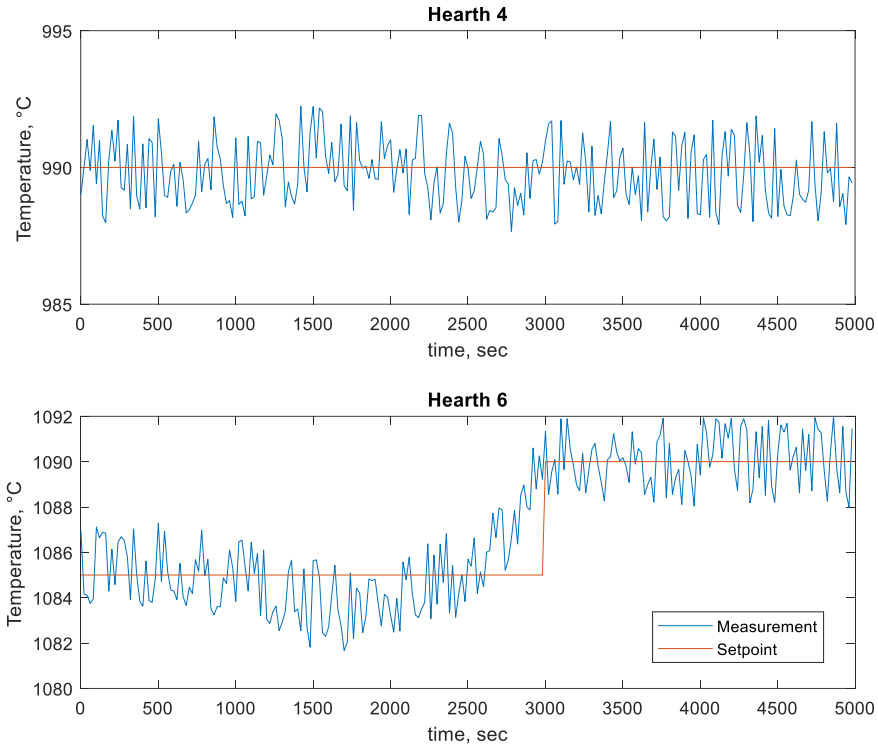

Figure 8.8 Setpoint change (+5 °C) to the hearth 6, Controlled Variables.

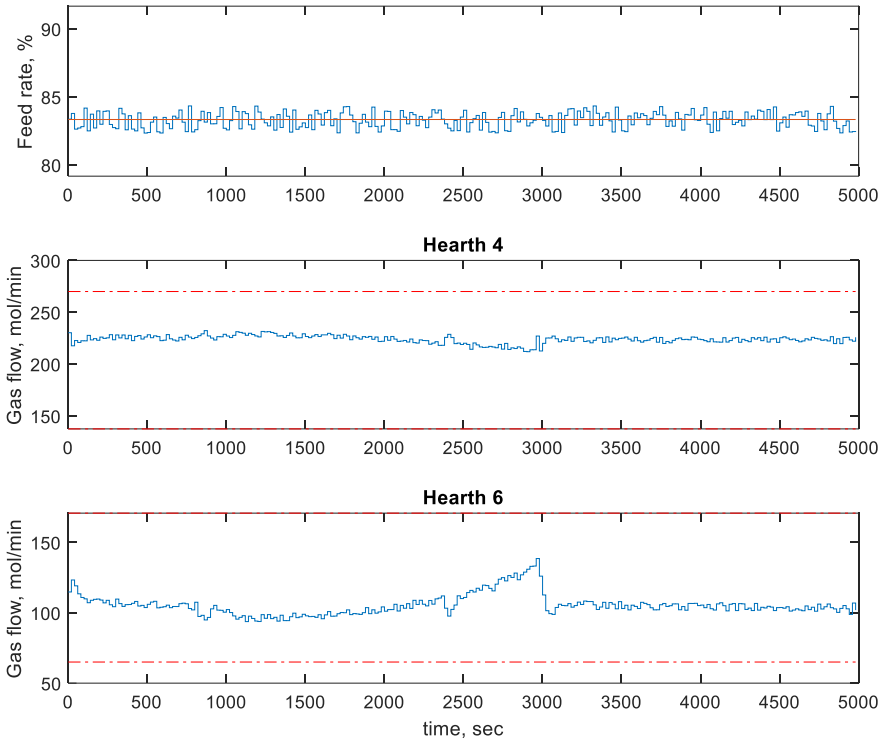

Figure 8.9 Setpoint change (+5 °C) to the hearth 6, Feed rate and gas flows.

Figure 8.10 and Figure 8.11 show the simulation results of the MPC, when the hearth 6 temperature setpoint was decreased by 5 °C after 3000 seconds. The feed rate was maintained at a value of 83.33% and the initial temperature setpoint values were 990 and 1085 °C for the hearth 4 and 6 respectively. The MPC displays significant results in regulating the controlled variables to the setpoint values of the temperatures in the hearths 4 and 6. The MPC controller begins to adjust the gas flows anticipating the setpoint that occurs at 3000 seconds.

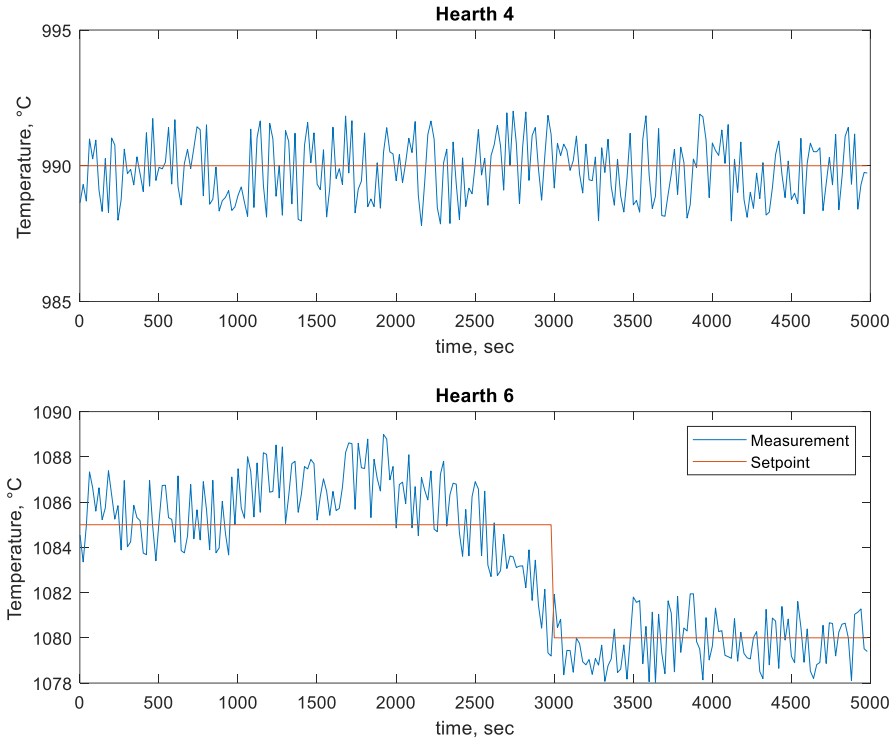

Figure 8.10 Setpoint change (-5 °C) to the hearth 6, Controlled Variables.

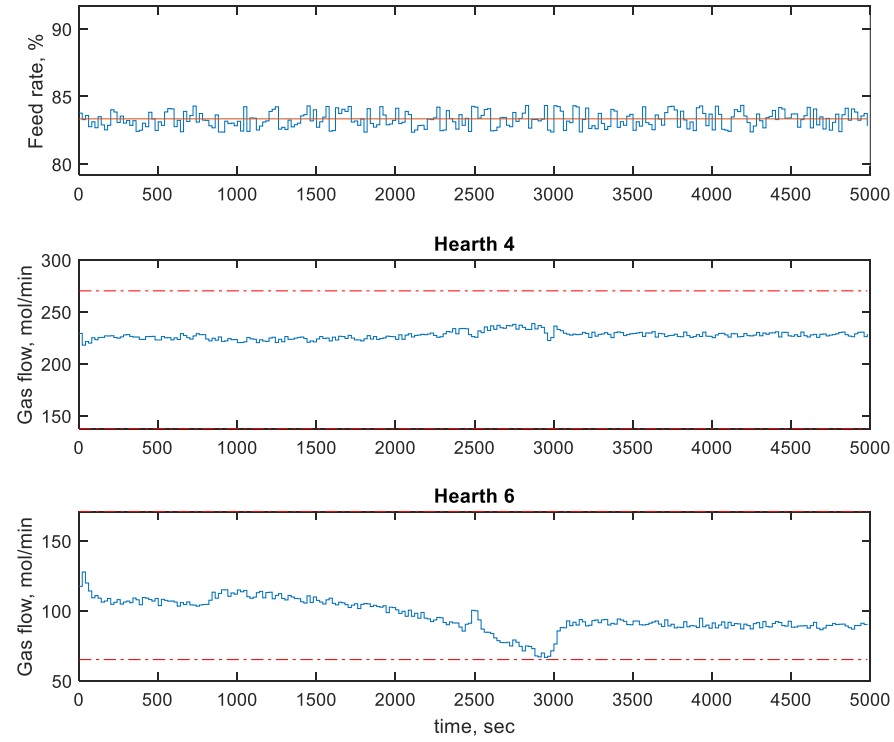

Figure 8.11 Setpoint change (-5 °C) to the hearth 6, Feed rate and gas flows.

8.2.3.2 Effect of the capacity variation on the control

Figure 8.12 and Figure 8.13 display the effect, on the temperature control, of the feed rate increase by 4.16% at 2000 seconds. The effect of the feed rate increase on the controlled temperatures is minimized fairly well by the MPC strategy. Even though the feed rate change is an unexpected event, the MPC performs remarkably well in regulating the temperatures. A similar result is observed in Figure 8.14 and Figure 8.15, which present the case when the feed rate is decreased by 4.16% at 2000 seconds.

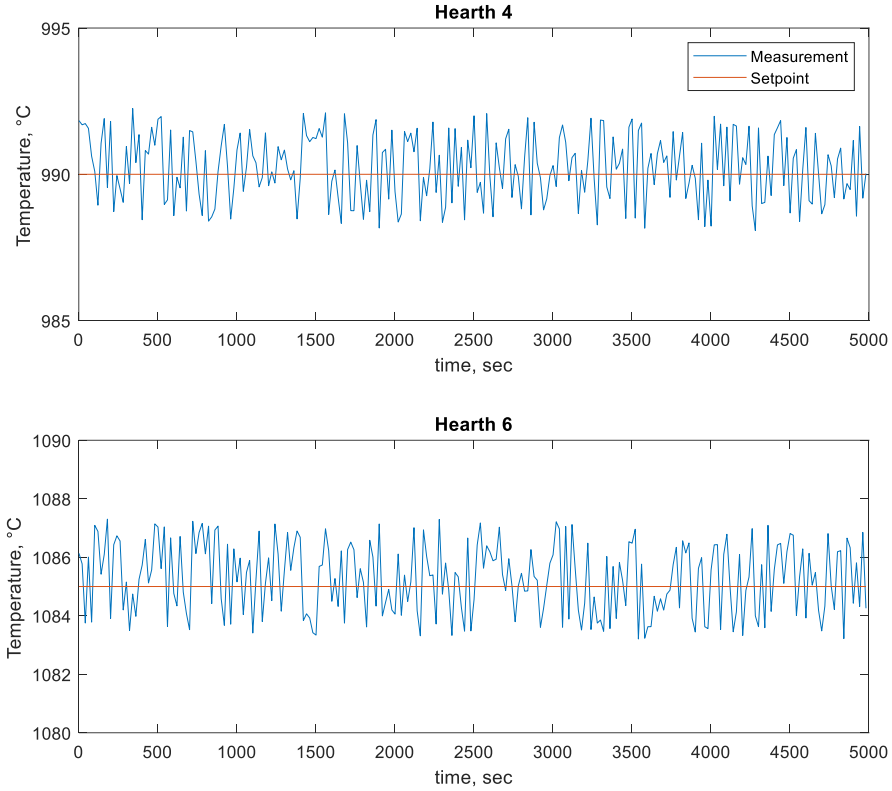

Figure 8.12 Feed rate increase (+4.16%), Controlled Variables.

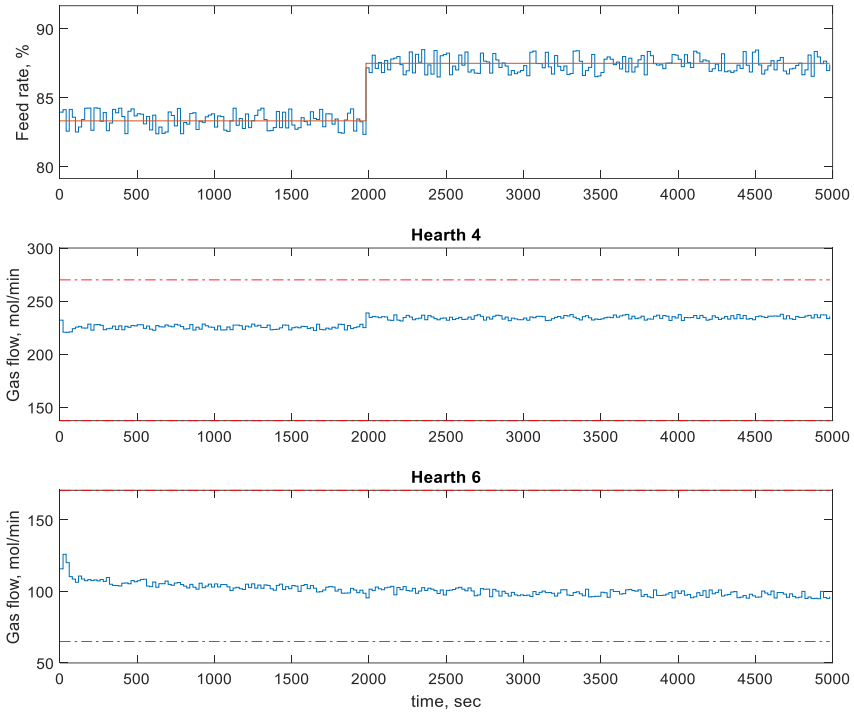

Figure 8.13 Feed rate increase (+4.16%), Feed rate and gas flows.

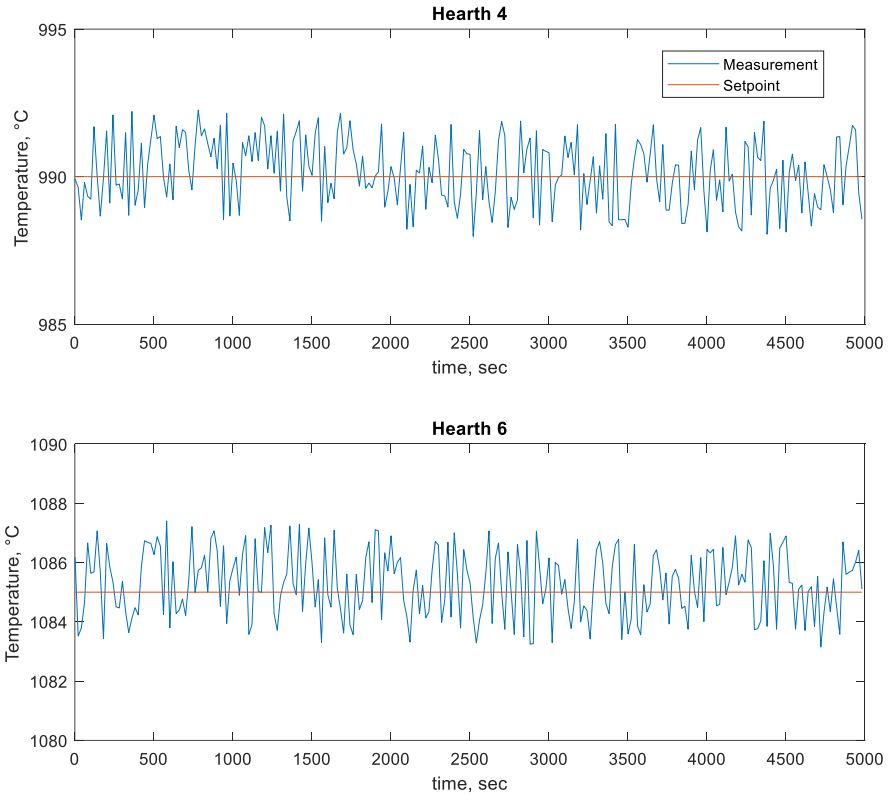

Figure 8.14 Feed rate decrease (-4.16%), Controlled Variables.

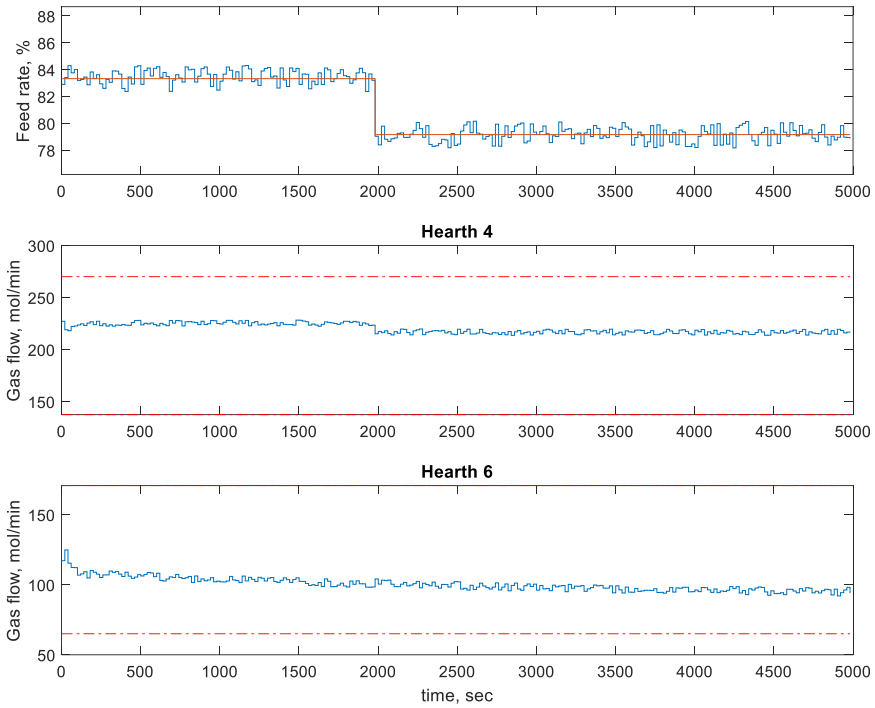

Figure 8.15 Feed rate decrease (-4.16%), Feed rate and gas flows.

8.2.4 Comparison of MPC vs PI control of the furnace temperature

This subsection presents a comparison between the MPC based on the linear model (Equation *(8.22)*) of the MHF and a PI control scheme for the same model to control the furnace temperatures in the hearths 4 and 6. The PI controller was designed and tuned using the Ziegler-Nichols method (Ziegler and Nichols, 1993). The Ziegler-Nichols method offers a simple and classical tuning approach for the comparison of the control schemes; other tuning methods could be considered in future research. The control strategies are compared to each other on the basis of the mean squared error (Equation (5.12)) around the setpoints and measured controlled variables. Figure 8.16 illustrates the PI control scheme designed for the MHF.

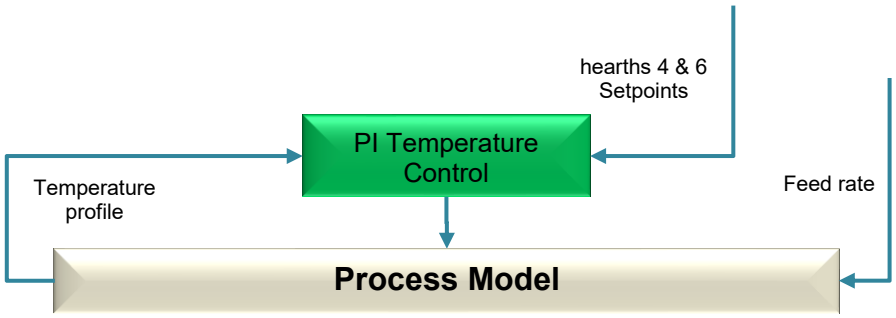

Figure 8.16 PI control scheme for the MHF.

Figure 8.17 and Figure 8.18 display the comparison between the MPC and PI strategies for a setpoint increase of 5 °C in the hearth 4 at 3000 seconds. The initial temperatures of the hearths 4 and 6 are 990 and 1085 °C respectively. The PI control presents stable control as it regulates fairly well the temperatures of the hearths 4 and 6. The MPC strategy also presents good temperature regulation but, as expected, the MPC anticipates the change in the temperature setpoint and adjust the gas flows accordingly. Due to the absence of a model in the PI scheme, the control presents interactions on the temperature control in the hearth 6, as seen in the bottom of Figure 8.17 between 3000 and 4000 seconds. This phenomenon is observed more clearly in Figure 8.18 where the gas flow of the hearth 6 is practically unaltered, provoking the interaction in the temperatures. Since MPC features a model of the process, the interactions are considered when regulating the temperatures and thus minimizing its effects.

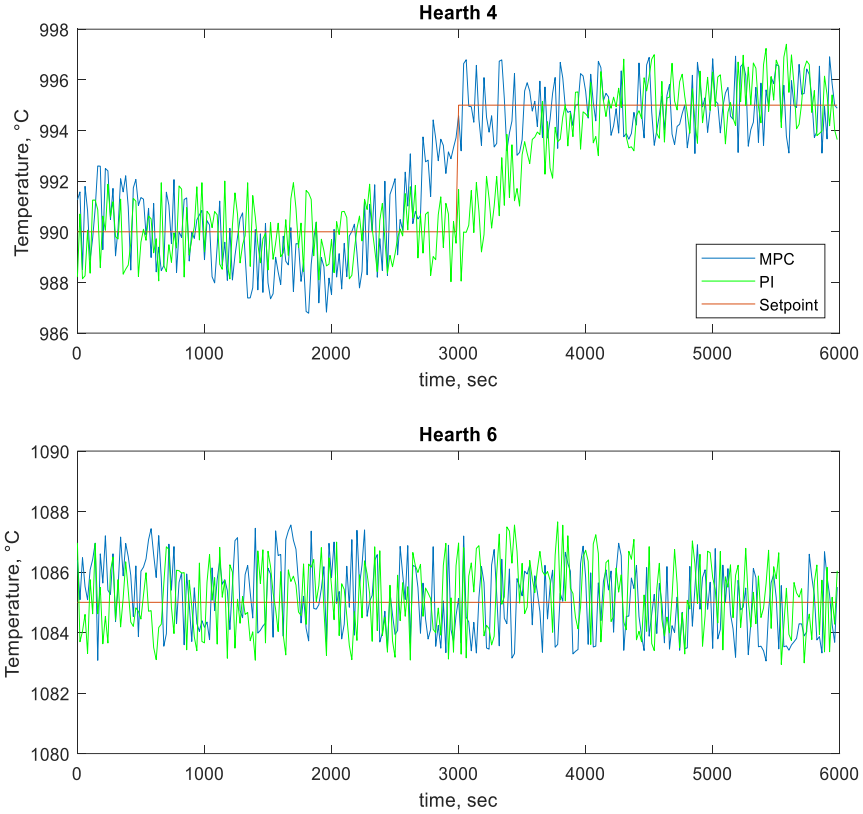

Figure 8.17 Comparison of MPC vs PI control, Controlled Variables.

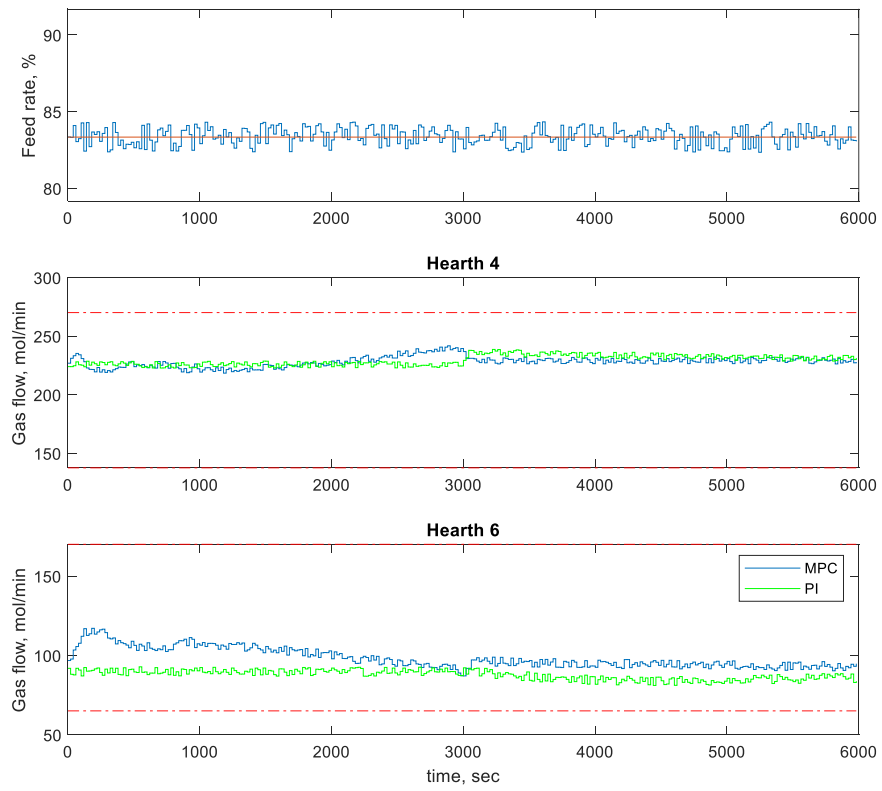

Figure 8.18 Comparison of MPC vs PI control, Feed rate and gas flows.

Table 8.1 shows the MSE performance comparison between the MPC and PI control strategies for an increase in the setpoint temperature of the hearth 4 by 5 °C at 3000 seconds. Overall, the MPC displays superior performance, as it dynamically minimizes the error between the controlled variable and the setpoint.

Table 8.1 Performance comparison of the MPC vs PI scheme.

Control Strategy	MSE Hearth 4 temperature	MSE Hearth 6 temperature
MPC	0.9795	0.0730
PI	1.3855	0.1214

8.3 Future Research: NMPC and EMPC strategies for the MHF control

This subsection presents the schemes of NMPC and EMPC strategies for the MHF. The aim is to design control strategies that automate the kaolin calcination process, considering the mineralogy information from the soft sensors as constraints, while dynamically maximizing capacity, minimizing energy consumption, and maintaining quality. First, the simplified nonlinear model of the MHF is described. Next, the definition of Nonlinear MPC is given, followed by, the design of the Nonlinear MPC strategy for the MHF. Finally, the concept of Economic MPC is introduced and the design of the EMPC for the MHF presented.

8.3.1 Simplified model of the MHF

For future implementation of a nonlinear model of the furnace to NMPC or EMPC, a simplified model based on the mechanistic model described in Chapter 4 was developed. A simplification of the mechanistic model is constructed based on its dynamic behavior and its nonlinearities separately. Separating the model into a nonlinear static block and a linear dynamic block, makes it is possible to build a model that preserves the performance of the original while simplifying the calculations. A Hammerstein model comprises the linear dynamic block being preceded by a static input nonlinearity while the opposite case,

where the static nonlinear block is placed after a linear dynamic block, the model is defined as a Wiener model (Zhu, 2001).

The simplified model is formulated as a Hammerstein-Wiener model (HWM). The HWM divides the dynamic process in blocks that comprise the dynamics in linear form and the nonlinearities in static for. The linear block, which holds the dynamics of the process, is preceded and followed by a static nonlinear block.

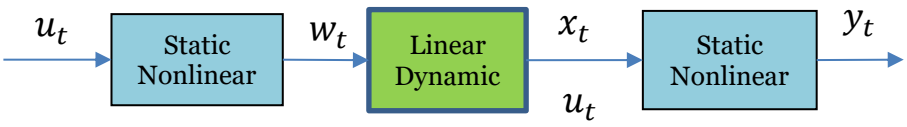

Figure 8.19. Structure of Hammerstein-Wiener model (Zhu, 2001).

Figure 8.19 displays the structure of the HWM which represents the dynamic process by means of input and output static nonlinear blocks surrounding the dynamic linear block. As discussed in Eskelinen et al., (2015), the dynamics of the MHF include a very fast component, which is related to the gas phase, and a slower component, linked to the solid state. For the NMPC/EMPC design the temperature of the solid must be defined dynamically while the gas temperature profile may be modeled with algebraic equations.

The simplified model is defined as the following Hammerstein-Wiener nonlinear dynamic model (Gómez Fuentes and Jämsä-Jounela, 2018b):

$$\begin{aligned} x_{t+1} &= \alpha x_t + (1-\alpha)F(u_t) \\ y_t &= G(u_t, x_t) \end{aligned} \qquad (8.25)$$

Where u_t represents the input variables to the process (kaolin feed, gas flows to the hearths 4 and 6), x_t denotes the solid temperature in each volume of the furnace and the interior wall temperatures in the hearths, α is a parameter characteristic of the HWM, which is found through identification using the identification toolbox included in MATLAB®. $F(u_t)$ and $G(u_t, x_t)$ are static nonlinear functions based on the mechanistic model response and energy balances respectively.

A look-up table has been constructed, by simulating the mechanistic model with various process inputs, to define the first function $F(u_t)$,

which describes the steady-state values of the process. The values found are interpolated as follows:

$$F(u_t) = \sum_{i=1}^{5}\sum_{j=1}^{5}\sum_{k=1}^{5} b_{i,j,k}\, h_i^x(F_K) h_j^y(F_{H4}) h_k^z(F_{H6}) \qquad (8.26)$$

where $b_{i,j,k}$ represents the values from the look-up table, and h_i^x, h_j^y and h_k^z denotes the piecewise linear basis functions that have been used for the interpolation.

The second function $G(u_t, x_t)$ describes the steady-state values of the gas temperature near the walls in the hearths (the temperature profile), which was implemented by calculating the energy balance for the gas phase.

8.3.2 Setup of the MHF simulation environment for NMPC/EMPC implementation

The overview of the simulation environment for the NMPC/EMPC framework is illustrated in Figure 8.3. The mechanistic model defined in Chapter 4 functions as the real process. The mechanistic model obtains the feed rate from the NMPC/EMPC and the gas flow rates to the hearths 4 and 6 from the basic temperature PI controller. The gas flow rates to the hearths 4 and 6, and the temperature profile estimated by the model are sent to the state estimator, which calculates the current state of the furnace. Finally, the simplified model is used as the prediction model in the MPC/EMPC optimization.

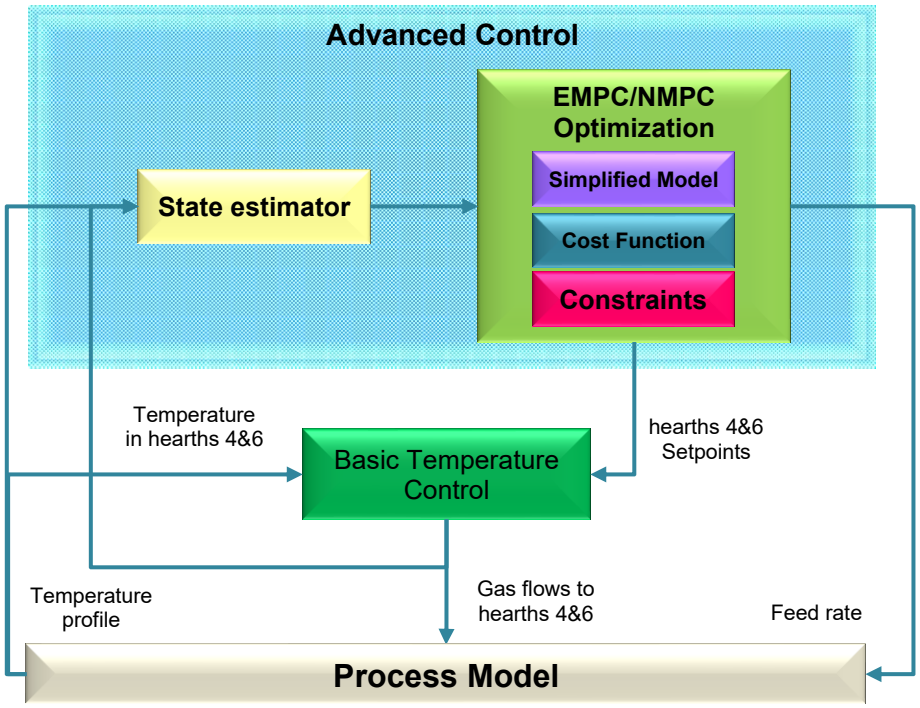

Figure 8.20. Simulation setup of NMPC/EMPC for the MHF.

8.3.3 Nonlinear Model Predictive Control

In this subsection set theory notation is applied to define the Nonlinear MPC. This notation is widely used in the topic of advanced control strategies.

Considering the discrete nonlinear process of the form:

$$x_{t+1} = f(x_t, u_t), \qquad x_0 = x(0) \tag{8.27}$$

where $f: \mathbb{X} \times \mathbb{U} \to \mathbb{R}^n$, $x_t \in \mathbb{X} \subseteq \mathbb{R}^n$, and $u_t \in \mathbb{U} \subseteq \mathbb{R}^m$ are the process state and control input respectively, for time $t \in \mathbb{I}_{\geq 0} = [0,1,2 \dots]$, and initial condition $x_0 \in \mathbb{X}$. The constraints for the process may be formulated as:

$$(x_t, u_t) \in \mathbb{Z} \subseteq \mathbb{X} \times \mathbb{U} \tag{8.28}$$

For all $t \in \mathbb{I}_{\geq 0}$; represent by $\mathbb{Z}_{\mathbb{X}}$ the projection of $\mathbb{Z}$ on $\mathbb{X}$, in other words: $\mathbb{Z}_{\mathbb{X}} := \{x \in \mathbb{X}: \exists u \in \mathbb{U} \text{ s.t. } (x,u) \in Z\}$. Then, S is considered as the set of all achievable state/input equilibrium sets of Equation (8.*27*):

$$S := \{(x,u) \in \mathbb{Z}: x = f(x,u)\}, \tag{8.29}$$

S is considered to be non-empty. The control for the process in Equation (8.*27*) must be stabilized at a setpoint x^*, which is a point of the process,

where it remains in equilibrium, and the matching control input is u^*, this means that $(x^*, u^*) \in S$. The next assumptions are considered: the set $\mathbb{U}$ is compact, the function f is continuous, and the set $\mathbb{Z} \subseteq \mathbb{X} \times \mathbb{U}$ is closed.

Next, the optimization problem is resolved, to define the receding horizon control law at every instant $t \in \mathbb{I}_{\geq 0}$, while the state x_t is measured.

$$\begin{aligned} &\min_{u_t} J_N(x_t, u_t) \\ &\hat{x}(t+1|t) = f(x_t, u_t), \quad t \in \mathbb{I}_{[0,N-1]} \\ &x_0 = x(0) \\ &(x_t, u_t) \in \mathbb{Z}, \quad t \in \mathbb{I}_{[0,N-1]} \\ &x_N = x(N) \in \mathbb{X}^f \end{aligned} \tag{8.30}$$

where:

$$J_N(x_t, u_t) \coloneqq \sum_{i=0}^{N-1} \ell(x_t, u_t) + V^f(x_N) \tag{8.31}$$

The closed terminal region is identified as $\mathbb{X}^f \subseteq \mathbb{X}$, the stage cost function is denoted as $\ell: \mathbb{X} \times \mathbb{U} \to \mathbb{R}$, and the terminal cost function is symbolized as $V^f: \mathbb{X}^f \to \mathbb{R}$. These functions are considered to be continuous.

Defining the values that minimize the cost function:

$$\underset{\to 0}{u^0} \coloneqq [u^0(0|t), \dots, u^0(N-1|t)] \tag{8.32}$$

with the matching state sequence:

$$\underset{\to 0}{x^0} \coloneqq [x^0(0|t), \dots, x^0(N-1|t)] \tag{8.33}$$

and the matching optimal value function:

$$J_N^0(x_t) \coloneqq J_N\left(x_t, \underset{\to 0}{u^0}\right) \tag{8.34}$$

Now the MPC may be resolved with the following algorithm:

1- Consider the process of Equation *(8.27)*
2- Estimate the state x_t at each time $t \in \mathbb{I}_{\geq 0}$
3- Resolve problem of Equation *(8.30)*
4- Implement control input $u_t \coloneqq u^0(0|t)$

The outcomes of the algorithm in the closed loop process are as follows:

$$x_{t+1} = f\big(x_t, u^0(0|t)\big), \quad x_0 = x(0) \qquad (8.35)$$

With the purpose of ensuring that x^* is a steady equilibrium point for the process in Equation *(8.35)*, a certain condition should be forced on the stage and terminal cost functions (ℓ, V^f), and terminal region $\mathbb{X}^f$ (Rawlings and Mayne, 2009).

The stage cost function ℓ fulfills $\ell(x^*, u^*) = 0$, and there is a function $\alpha_1 \in \mathcal{K}_\infty$ so that $\ell(x_t, u_t) \geq \alpha_1(|x - x^*|)$ for all $(x_t, u_t) \in \mathbb{Z}$, while the terminal cost function V^f fulfills $V^f(x^*) = 0$ and $V^f(x) \geq 0, \quad \forall x \in \mathbb{X}^f$.

The terminal region $\mathbb{X}^f \subseteq \mathbb{X}$ is closed and $x^* \in \mathbb{X}^f$. Furthermore, there is a local secondary control law so that $u_t = \kappa^f(x)$ and for all $x \in \mathbb{X}^f$ the following is fulfilled:

i) $(x, \kappa^f(x)) \in \mathbb{Z}$

ii) $f(x, \kappa^f(x)) \in \mathbb{X}^f$

iii) $V^f(f(x, \kappa^f(x))) - V^f(x) \leq -\ell(x, \kappa^f(x)) + \ell(x^*, u^*)$

The previous considerations indicate that when the local auxiliary controller is applied to the process in Equation *(8.27)*, (i) input and state constraints are satisfied inside the terminal region and (ii) the terminal region is constant. Condition (iii) indicates that V^f performs as a Lyapunov function incorporated into the terminal region (for this case V^f is nonnegative with respect to x^*). These considerations are assumed to be standard for stabilizing in MPC with a terminal cost/ terminal region formulation (Rawlings and Mayne, 2009).

Defining $\mathbb{X}_N$ as the set of all states $x \in \mathbb{X}$, so that the process in Equation *(8.27)*, has a solution. Next, assuming that all considerations hold, then the process is feasible for all $t \in \mathbb{I}_{\geq 0}$. In addition, for the closed loop process, the input constraints and the pointwise-in-time state are fulfilled for all $t \in \mathbb{I}_{\geq 0}$, and x^* is a balance point asymptotically stable with region of attraction $\mathbb{X}_N$ (Rawlings and Mayne, 2009).

8.3.3.1 NMPC framework for the MHF

The designed NMPC control focuses on optimizing the temperature profile in the furnace through the determination of the optimal feed rate and providing the setpoints to the basic temperature controllers in the hearths 4 and 6, as shown in Figure 8.21. The main feedbacks from the process to the controller are the gas consumption in the hearths 4 and 6 and the gas temperature measured in other hearths.

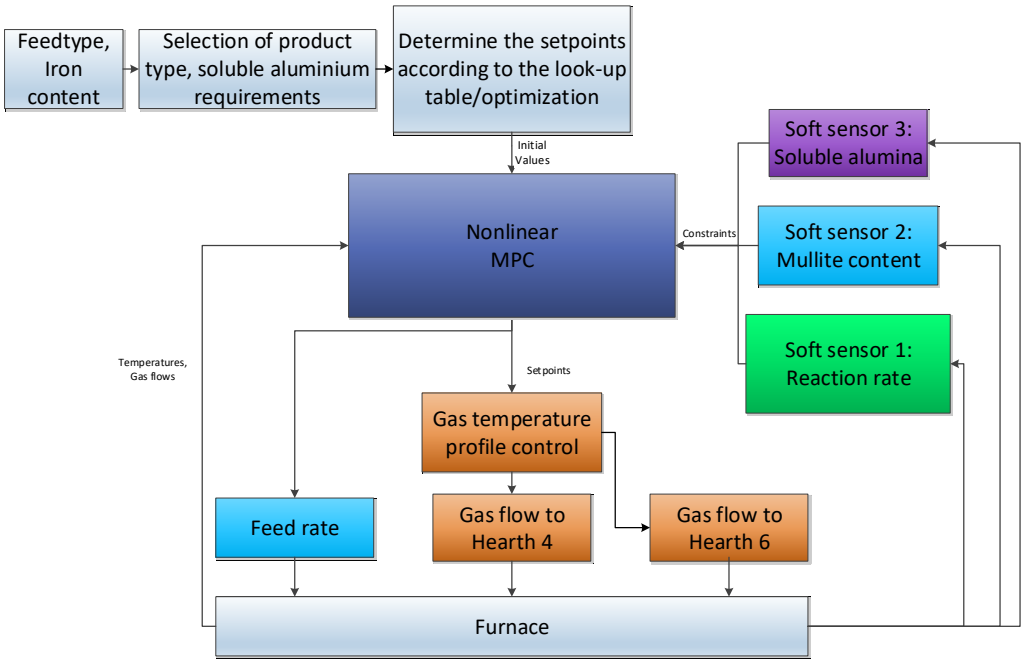

Figure 8.21 NMPC framework for the MHF.

The optimization problem is solved, by predicting the states using the simplified model and obtaining the optimal temperature setpoints. The cost function includes terms for minimizing the tracking error, rate of change of the manipulated variables as well as minimizing the use of energy. Additionally, the cost function features a term for maximizing the capacity of the furnace. The optimization problem is presented in Equation *(8.36)*:

$$\min_{u_{mv}} J = \sum_{i=1}^{N_p} \left\| y_t^{sp} - y_t^{cv} \right\|_Q + \sum_{i=1}^{N_c} \|\Delta u_t^{mv}\|_R + \sum_{i=1}^{N_c} \|u_t^{mv}\|_V - \sum_{i=1}^{N_c} \|F_K\|_W$$

$$\begin{cases} x_{t+1} = \alpha x_t + (1-\alpha) F(u_t) \\ y_t = G(u_t, x_t) \end{cases}$$
$$F_K \in [79.17, 100]\%$$
$$F_{H4} \in [137, 270] mol/min$$
$$F_{H6} \in [65, 170]\ mol/min$$
$$\Delta F_K \in [-4.16, 4.16]\%$$
$$\Delta F_{H4}, \Delta F_{H6} \in [-3.49, 3.49] mol/min$$
$$m(F_{H4}, F_{H6}, T_{H1}, F) \leq\ 4\ wt.\%,$$
$$S(F_{H4}, F_{H6}, T_{H4}, T_{H6}, F_K) \leq 0.50\ wt.\%,$$
$$\mathrm{T}_{H6} \geq T_{H6}^{min}(F_K, r),$$
$$T_{H4}^{min} < T_{H4} < T_{H4}^{max},$$
$$Vio \geq Vio^*$$

(8.36)

where y_t^{sp} is the controlled variable set-point trajectory, N_p is the prediction horizon, N_c is the control horizon. $u_t^{mv} = [F_{H4}, F_{H6}]$ represents the manipulated variables (gas flows to hearths 4 and 6), $y_t^{cv} = [T_{H4}, T_{H6}]$ represents the controlled variables, F_k is the feed rate, $[\Delta F_K, \Delta F_{H4}, \Delta F_{H6}]$ is the rate of change for the manipulated variables. The simplified model (Section 8.3.1) is represented in the state-space form to facilitate the implementation of the NMPC paradigm. r denotes the current value of the reaction soft sensor, T_{H1}, T_{H4} and T_{H6} are the temperatures in the hearths 1, 4, and 6, respectively and m is the mullite content of the product and its threshold. S represents the soluble alumina content and its threshold (if applicable). Vio symbolizes the brightness (measured as the percentage of light reflected in the violet spectrum) and its threshold. Matrices Q, R, V and W in Equation *(8.36)* represent the weighting matrices for the output and input variables respectively. Finally, the values of the process constraints are shown in Equation *(8.36)*.

8.3.4 Economic Model Predictive Control

In the past 30 years MPC has become more widespread in industry and academic research. The coupling of MPC with Real-Time Optimization (RTO) ,as depicted on the left side of Figure 8.22, has become a traditional control method in industries (Ellis and Christofides, 2013b). The RTO, which calculates the economically optimal setpoint for the process, is usually obtained in a period of hours at a specific steady-state

(Backx *et al.*, 2000). The setpoint is directed to the second layer, in this example the MPC, and the controller regulates the process to the setpoint given by the RTO. The disadvantage of this two-layer design is that the RTO concentrates on the steady-state optimization, which may not be the economically best strategy. This is due to the possible existence of an unreachable setpoint given by the economic optimization (Rawlings *et al.*, 2008).

It was revealed that economic optimization may be significantly enhanced if the cost function were to be combined directly into the MPC (Rawlings *et al.*, 2012; Rawlings and Amrit, 2009). Economic Model Predictive Control is a modification of MPC, which utilizes a general cost function to dynamically optimize the economic objective of the process (Heidarinejad *et al.*, 2012). In this situation, no reference or target steady-state is given to the EMPC, and the objective function is not compulsorily positive definite as usually established for the standard MPC (Ellis and Christofides, 2013a). The control framework based on EMPC is depicted on the right side of Figure 8.22.

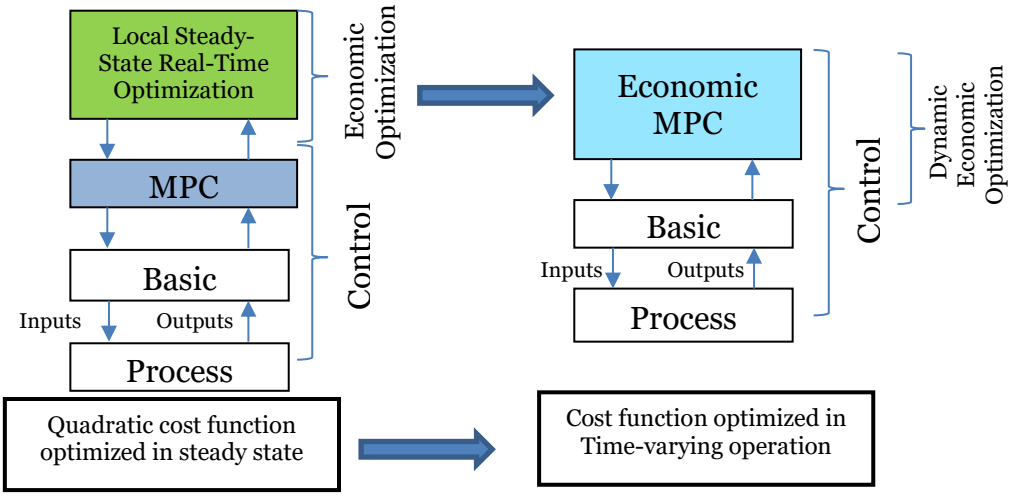

Figure 8.22 Differences between MPC with RTO and EMPC (Ellis *et al.*, 2014).

Presently, EMPC has now become a widely accepted method with an extended range of implementations (Angeli *et al.*, 2011). Analogous to the MPC optimization, the EMPC objective is formulated as follows:

$$J_N(x_t, u_t) \coloneqq \sum_{i=0}^{N-1} \ell(x_t, u_t) \tag{8.37}$$

where the stage cost function $\ell(x_t, u_t)$ is expressed as an arbitrary cost function that approximates the process economics (Amrit *et al.*, 2013). Similarly to traditional MPC, the stage cost function is normally convex for linear systems and commonly non-convex for nonlinear systems.

Contrarily to traditional MPC, the stage cost function $\ell(x_t, u_t)$ from Equation *(8.37)* may not reach its minimum at a specific equilibrium state. Specifically, the optimal steady-state stage cost for MPC is not essentially smaller contrasted with the stage cost in EMPC. Therefore, limit cycles may occur in EMPC because they are economically advantageous, which can only arise for a nonconvex economic objective or a nonlinear process dynamic. Therefore, it is beneficial to achieve the asymptotic average limit presented as follows:

$$\lim_{T \to +\infty} \sup \frac{\sum_{t=1}^{T} \ell(x_t, u_t)}{T} \leq \ell(x_S, u_S) \tag{8.38}$$

In order to guarantee the normal EMPC performance, the Equation *(8.32)* is used as the control series for each time step and computed for MPC, as stated before. Then, it is considered the admissible set $\mathbb{Z}_N$ of $\left(x_0, \underset{\to 0}{u}\right)$ sets that fulfills the constraints presented as follows:

$$\mathbb{Z}_N \coloneqq \begin{Bmatrix} \left(x_0, \underset{\to 0}{u}\right) | \exists x_1, \dots, x_N : x_{t+1} = f(x_t, u_t), \\ (x_t, u_t) \in \mathbb{Z}, t \in \mathbb{I}_{[1,N-1]} \\ x_0 = x(0), x_s = x_N \end{Bmatrix}, \tag{8.39}$$

and its projection $\mathcal{X}_N$ on $\mathbb{X}$ that is specified as:

$$\mathcal{X}_N \coloneqq \left\{ x \in \mathbb{X} \,\middle|\, \exists \underset{\to 0}{u} : \left(x, \underset{\to 0}{u}\right) \in \mathbb{Z}_N \right\}. \tag{8.40}$$

According to Angeli et al., (2012), for every $x \in \mathcal{X}_N$, there is at least one control series that guides the state to x_S at time N without leaving $\mathcal{X}_N$ and the closed-loop process in Equation *(8.27)* with $\underset{\to 0}{u}^0$ includes an asymptotic average performance i.e., as a minimum, as adequate as the best acceptable steady-state.

Even with the asymptotic average performance being assured, the EMPC with the objective described by Equation *(8.37)* does not assure stability in a closed loop. In traditional MPC, the optimal cost of $J_N(x_t)$, defined before as $J_N^0(x_t)$ in Equation *(8.34)* is utilized as a Lyapunov function for the closed loop process, which is invariably decreasing for various closed loop solutions, i.e., $J_N^0(x_{t+1}) \leq J_N^0(x_t)$. However, for EMPC, this situation does not automatically occur due to the possible limit cycles, even if the process is stable. The explanation is that for the case of non-convex cost functions and nonlinear processes, it is not certain that x_S is the optimal steady-state.

However, convergence to a steady-state can be guaranteed for an EMPC with the terminal constraint based on a Lyapunov function, if the strong duality assumption is fulfilled (Diehl *et al.*, 2011). This means that the following solution x_s, u_s of the steady-state optimization problem

$$\begin{aligned} &\min_{x,u} l(x,u) \\ &x = f(x,u) \\ &g(x,u) \leq 0 \end{aligned} \tag{8.41}$$

is the unique minimizer of the expression presented as follows, for some Lagrange multiplier λ_s:

$$\min_{x,u} l(x,u) + \big(x - f(x,u)\big)' \lambda_s. \tag{8.42}$$

Then, the strong duality condition in Equations *(8.41)*, *(8.42)* was softened to the dissipativity assumption (Angeli *et al.*, 2012).

The process of Equation *(8.27)* is considered dissipative with respect to the supply rate $s(x_t, u_t): \mathbb{X} \times \mathbb{U} \to \mathbb{R}$, If a there is a function $\lambda: \mathbb{X} \to \mathbb{R}$ such that:

$$\lambda\big(f(x_t,u_t)\big) - \lambda(x_t) \leq s(x_t,u_t), \forall (x_t,u_t) \in \mathbb{Z} \tag{8.43}$$

In addition, if there is a positive definite function $\rho: \mathbb{X} \to \mathbb{R}_{\geq 0}$ such that:

$$\lambda\big(f(x_t,u_t)\big) - \lambda(x_t) \leq -\rho(x_t) + s(x_t,u_t), \tag{8.44}$$

then the process is strictly dissipative (Angeli *et al.*, 2012).

There are numerous expressions to reach closed-loop stability if the dissipativity assumptions are satisfied, together with the terminal constraints and terminal costs.

For the economic problem, x_S is an asymptotically stable state with attraction region $\mathcal{X}_N$, if it is strictly dissipative for the supply rate in Equations *(8.43)*, *(8.44)*. This can be demonstrated by formulating a secondary augmented problem with a rotated stage cost, then finding that the feasible sets, $\mathcal{X}_N$, coincide. Finally, this shows that the objective functions of the original and rotated formulations are altered only by a constant, deducing that both solutions are identical (Angeli *et al.*, 2012).

Closed-loop stability could also be reachable by using an adequate terminal cost with an inequality terminal constraint, as opposed to an equality constraint. This proof also comprises a rotated stage cost, which is assumed as a Lyapunov function, and considering the strict dissipativity property (Angeli *et al.*, 2012).

8.3.4.1 EMPC framework for the MHF

The designed EMPC control is aimed at finding the optimal economic performance of the furnace through dynamically maximizing the profit while considering the process constraints of the MHF. The EMPC provides the feed rate and defines the setpoints to the basic temperature controllers in the hearths 4 and 6, as shown in Figure 8.23. The main feedbacks from the process to the controller are the gas consumption in the hearths 4 and 6 and the gas temperature measured in other hearths.

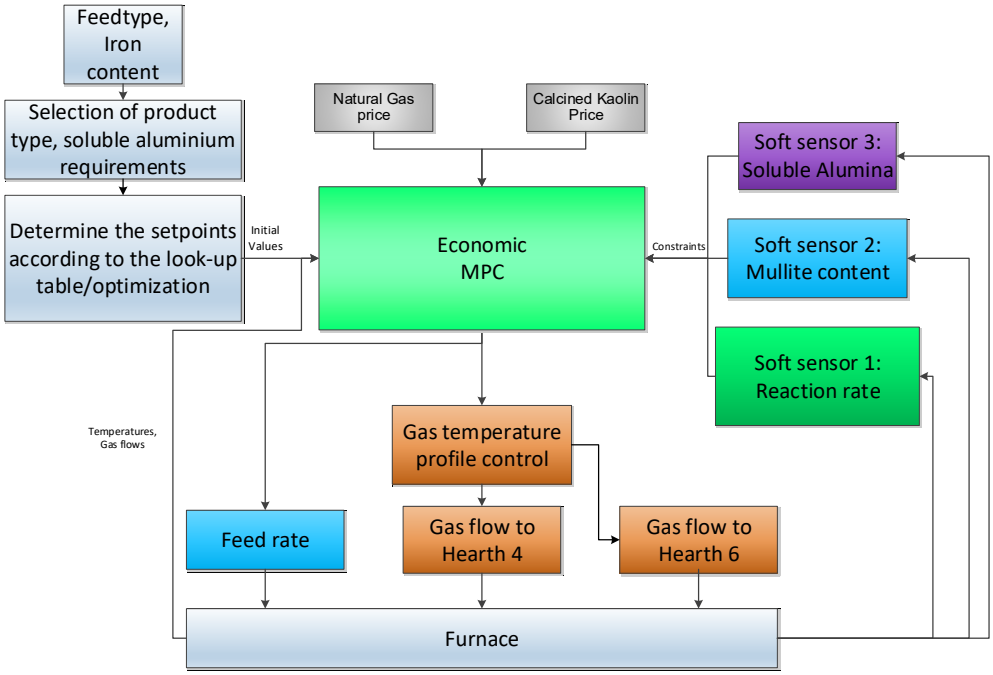

Figure 8.23 EMPC framework for the MHF.

The economic objective of the process is to maximize production of the calcined kaolin while minimizing energy consumption. The flow rate of the calcined kaolin (F_C), containing the product of interest, is obtained using the mass balance presented as follows:

$$F_C = (1 - c_{H2O}) * (1 - c_{fm}) * F_K \qquad (8.45)$$

From Eskelinen (2014), it is known that when the kaolin goes into the process, it expels approximately 14% of its weight via evaporation and dehydroxylation (c_{H2O}), as described in Equations (2.1) and (2.2). In addition, the calcined product holds nearly 0.5% of free moisture (c_{fm}) when it exits the process.

The second interest, as mentioned earlier, is to minimize the energy use of the furnace. In the multiple hearth furnace, the main energy source is methane gas, which is combusted to rise temperature, and to achieve the required levels to initiate the various chemical reactions that occur inside the furnace.

The methane entering the process is combusted in the hearths 4 and 6, then the respective gas flows for the hearths 4 and 6 are F_{H4} and F_{H6} are used to obtain total gas flow entering the process:

$$F_g = F_{H4} + F_{H6} \qquad (8.46)$$

To formulate the cost function, it is important to consider the prices of the variables related to the process economics. Hence, the cost function is defined as an equation that includes the main economic interests of the process (profit).

$$J_{MHF} = \sum_{t=0}^{N} p_C F_C - p_g F_g \qquad (8.47)$$

Where p_C and p_g are the prices of calcined kaolin and methane gas respectively. J_{MHF} represents the Economic Performance Index of the MHF for a particular interval of time $[0, N]$.

The solution to the optimization problem is found by forecasting the process states via the simplified model and calculating the optimal temperature setpoints. The optimization problem comprises constraints for minimizing the tracking errors and the rate of change of the manipulated variables. In addition, the optimization formulation includes a term for maximizing the capacity of the furnace. The optimization problem is described in Equation *(8.48)*:

$$\max_{u_t} J_{MHF} = \sum_{t=0}^{N} p_C F_C - p_g F_g$$

$$\begin{cases} x_{t+1} = \alpha x_t + (1-\alpha) F(u_t) \\ y_t = G(u_t, x_t) \end{cases}$$
$$F_K \in [79.17, 100]\%$$
$$F_{H4} \in [137, 270] mol/min$$
$$F_{H6} \in [65, 170]\ mol/min$$
$$\Delta F_K \in [-4.16, 4.16]\%$$
$$\Delta F_{H4}, \Delta F_{H6} \in [-3.49, 3.49] mol/min$$
$$m(F_{H4}, F_{H6}, T_{H1}, F) \leq\ 4\ wt.\%,$$
$$S(F_{H4}, F_{H6}, r, F_K) \leq 0.50\ wt.\%,$$
$$\mathrm{T}_{H6} \geq T_{H6}^{min}(F_K, r),$$
$$T_{H4}^{min} < T_{H4} < T_{H4}^{max},$$
$$Vio \geq Vio^{*} \qquad (8.48)$$

where $u_t = [F_K, F_{H4}, F_{H6}]$ represents the manipulated variables (feed rate and gas flows to hearths 4 and 6), $[\Delta F_K, \Delta F_{H4}, \Delta F_{H6}]$ is the rate of change for the manipulated variables. The simplified model (Section 8.3.1) is represented in the state-space form to facilitate the implementation of the EMPC paradigm. r denotes the current value of the reaction soft

sensor, T_{H1}, T_{H4} and T_{H6} are the temperatures in the hearths 1, 4, and 6, respectively and m is the mullite content of the product and its threshold. S represents the soluble alumina content and its threshold (if applicable). Vio symbolizes the brightness and its threshold. Finally, the values of the process constraints are shown in Equation *(8.48)*.

Summary

The development and simulation details of the linear MPC strategy for the MHF have been presented in this chapter. The MPC strategy has shown superior results compared with the PI-based control scheme for the temperature control of the furnace. An outline of future work to implement Nonlinear MPC and Economic MPC into the MHF has been presented in the final part of this chapter. The following chapter will outline the final conclusions obtained in this thesis.

9. Conclusions

This thesis focused on the design of a mineralogy-driven control strategy for the industrial MHF in kaolin calcination aiming to maximize the capacity and minimize energy consumption while maintaining the quality of the product. The control strategy was enhanced with the design of the mullite content (for capacity maximization), soluble alumina (for quality control), and reaction rate (for energy use minimization) soft sensors. The strategy was implemented for the mullite and reaction rate soft sensors, and then tested in the simulation environment based on the industrial data. Additionally, a testing and data collection campaign were planned and performed at the factory. The impact of the strategy results on the MHF process operation was analyzed and discussed. Finally, The MPC framework for the MHF in kaolin calcination was designed, implemented and tested in the simulation environment and further developments were outlined.

The analysis of the MHF dynamic behavior offered a deeper understanding about the operating conditions and physicochemical phenomena taking place in the MHF. First, the SOM method was used to determine the optimal temperature setpoints of the MHF based on the key process and mineralogy variables of the feed material and product. The SOM proved to be an excellent tool, which facilitated the recognition of the different calcined kaolin products and aided in the construction of look-up tables for the MHF optimal temperature setpoints. Next, analyzing the process data allowed to identify occurrences when the "spinel phase" shifted to the top part of the furnace (hearth 4 and 5). The relocation of the reaction affected the final product quality due to

unnecessary extra heat given to the furnace. Based on this analysis, a first principle “spinel phase” reaction rate soft sensor was designed to determine the progress of the reaction in the top part of the furnace with the aim of maximizing the energy savings. Then, it was determined that mullite content in the product can be defined as an indirect indicator of the quality of the final product and that online mullite content data could be used for capacity maximization. So, a mullite content soft sensor was developed based on first principles and next based on artificial intelligence. The estimated mullite content results were highly accurate with respect to the laboratory results. Additional mullite content data may prove valuable to improve the accuracy of the soft sensors. Next, the soluble alumina soft sensor is recognized as the standard indicator in the industry for the quality control of certain types of calcined kaolin. A soft sensor based on artificial intelligence was devised to estimate the soluble alumina content in the product. The results were highly satisfactory and could be improved with the inclusion of additional soluble alumina laboratory data.

The design of the enhanced control strategy presented in this research included 3 levels: optimizing, stabilizing and basic. Each level focused on a specific aspect to improve the performance of the furnace. The optimizing control featured the constructed look-up tables, which provide the initial temperature setpoints for the MHF based on the mineralogy information given by the feed material, and the mullite content soft sensor, which sets the constraints to maximize the capacity. Additionally, the soluble alumina soft sensor sets the constraints to maintain the quality of the product. The stabilizing level featured the integration of the reaction rate soft sensors and a feedforward controller to minimize the energy consumption of the MHF by preventing over calcination of the product. Finally, the basic level featured a mean temperature control to reduce the effects of the BtoB interaction occurring on the hearth 4.

The simulation environment designed for testing the performance of the enhanced control strategy included the dynamic model of the MHF,

which was validated in previous research. The mean temperature controller was tested, and the results showed improved performance compared with the current control scheme. The design of the mean temperature control was simple and was intended to be a straightforward practical solution to the BtoB phenomena and more research should be made to obtain better results. The stabilizing control showed great ability to minimize the reaction rate disturbance and significantly increased the energy savings of the furnace. Finally, the optimizing control for the MHF was simulated and tested, with results showing the excellent control to maximize the capacity while upholding the desired mullite content levels in the product.

The control logic of the multiple hearth furnace was evaluated in this work by industrial testing. Initially, the soft sensors were tested online in the plant automation system. The testing helped to improve the quality and usability of the MHF soft sensor software, and it assisted the operators to easily track the operating conditions of the MHF. The soft sensor software could be an excellent tool for obtaining additional information given by the process otherwise not available online. Next, a sampling and data collection campaign was performed over a period of 5 days to collect data from the calciner. The results showed the performance of the soft sensors to estimate the process variables compared with the laboratory data. In general, the soft sensors presented fairly good results to estimate the reaction rate, mullite content and soluble alumina. During the sampling campaign, a limited number of samples were collected, and the overall performance of the soft sensors could be further improved with an extended sampling campaign. Finally, the evaluation of the control concept logic outlined the possibilities to improve the performance of the process. Some instances exhibited the possibility to improve the capacity and quality of the product, which created the opportunity to implement the enhanced control strategy and then optimize the production of the furnace.

Finally, the applicability of Linear MPC for the MHF control strategy was studied. The MPC aimed to decrease the interactions in the temperature control between the burner zones of the hearth 4. The design of the Linear MPC framework for the MHF in kaolin calcination was described as well as the linear model of the MHF for MPC. The model was identified as a transfer function model and showed fairly good performance compared with the mechanistic model. A series of simulation tests were performed to study the behavior of the MPC control for the MHF. Next, the MPC control was compared with a temperature control PI scheme. The comparison results showed that the MPC was a superior alternative due to the integration of the process model and the ability to foresee and track the temperature setpoints. Finally, an outline of the future implementations of NMPC and EMPC into the MHF was presented. The advanced MPC implementations featured a simplified nonlinear model of the MHF based on a Hammerstein-Wiener model structure. These advanced MPC implementations offer excellent opportunities to further optimize the economic performance of the furnace, especially the EMPC framework, which shows great promise to achieve this objective due to its capability to dynamically optimize the economic objective of the process.

References

Allison, B. and Ball, J. (2004) Cascaded model predictive control of a rotary lime kiln, *Pulp and Paper Canada*, 105 (1), pp. 51–55.

Amrit, R., Rawlings, J. B. and Biegler, L. T. (2013) Optimizing process economics online using model predictive control, *Computers & Chemical Engineering*, 58, pp. 334–343. DOI:10.1016/j.compchemeng.2013.07.015.

Angeli, D., Amrit, R. and Rawlings, J. B. (2011) Enforcing convergence in nonlinear economic MPC, in: *IEEE Conference on Decision and Control and European Control Conference*. IEEE, pp. 3387–3391.

Angeli, D., Amrit, R. and Rawlings, J. B. (2012) On Average Performance and Stability of Economic Model Predictive Control, *IEEE Transactions on Automatic Control*, 57 (7), pp. 1615–1626. DOI:10.1109/tac.2011.2179349.

Backx, T., Bosgra, O. and Marquardt, W. (2000) Integration of Model Predictive Control and Optimization of Processes: Enabling Technology for Market Driven Process Operation, *IFAC Proceedings Volumes*, 33 (10), pp. 249–260. DOI:10.1016/s1474-6670(17)38550-6.

Bemporad, A. and Morari, M. (1999) Control of systems integrating logic, dynamics, and constraints, *Automatica*, 35 (3), pp. 407–427. DOI:10.1016/s0005-1098(98)00178-2.

Camacho, E. F. and Bordons, C. (1995) Model Predictive Control in the Process Industry, Advances in Industrial Control. 1st ed. London: Springer-Verlag, p. 239.

Camacho, E. F. and Bordons, C. (1999) Model Predictive Control. 1st ed. London: Springer London, p. 280.

Carlson, D. A., Haurie, A. B. and Leizarowitz, A. (1991) Infinite Horizon Optimal Control. 1st ed. Berlin: Springer Berlin Heidelberg, p. 332.

Chandrasekhar, S. and Ramaswamy, S. (2002) Influence of mineral impurities on the properties of kaolin and its thermally treated products, *Applied Clay Science*, 21 (3–4), pp. 133–142. DOI:10.1016/s0169-1317(01)00083-7.

Ciftci, S. and Kim, N. K. (1999) Control Schemes for an Industrial Rotary Calciner with a Heat Shield around the Combustion Zone, *Industrial & Engineering Chemistry Research*, 38 (3), pp. 1007–1023. DOI:10.1021/ie980229b.

Diehl, M., Amrit, R. and Rawlings, J. B. (2011) A Lyapunov Function for Economic Optimizing Model Predictive Control, *IEEE Transactions on Automatic Control*, 56 (3), pp. 703–707. DOI:10.1109/tac.2010.2101291.

Ellis, M. and Christofides, P. D. (2013a) Economic model predictive control with time-varying objective function for nonlinear process systems, *AIChE Journal*, 60 (2), pp. 507–519. DOI:10.1002/aic.14274.

Ellis, M. and Christofides, P. D. (2013b) Unifying dynamic economic optimization and model predictive control for optimal process operation, in: *2013 American Control Conference*. Washington: IEEE, pp. 3135–3140.

Ellis, M., Durand, H. and Christofides, P. D. (2014) A tutorial review of economic model predictive control methods, *Journal of Process Control*, 24 (8), pp. 1156–1178. DOI:10.1016/j.jprocont.2014.03.010.

Eskelinen, A. (2014) *Dynamic Modelling of a multiple hearth furnace*. Master thesis, Aalto University, Espoo.

Eskelinen, A., Zakharov, A., Hearle, J. and Jämsä-Jounela, S.-L. (2016) Dynamic modelling of a multiple hearth furnace for kaolin calcination with a sensitivity analysis with respect to reaction rates, *IFAC-PapersOnLine*, 49 (20), pp. 196–201. DOI:10.1016/j.ifacol.2016.10.120.

Eskelinen, A., Zakharov, A., Jämsä-Jounela, S.-L. and Hearle, J. (2015) Dynamic modeling of a multiple hearth furnace for kaolin calcination, *AIChE Journal*, 61 (11), pp. 3683–3698. DOI:10.1002/aic.14903.

Feher, J. D. and Erickson, K. T. (1993) Solving the Model Predictive Control Problem with Soft Constraints, in: *1993 American Control Conference*. San Francisco: IEEE, pp. 377–378.

Fleifil, M., Lorra, M., Baukal, C. E., Lewallen, J. A. and Wright, D. E. (2006) Thermal technology: Process burner spacing, *Petroleum Technology Quarterly*, Q (2), pp. 1–5.

Geyrhofer, W., Voglauer, B. and Joergl, H. P. (2003) Control of a roasting process for the recovery of vanadium, in: *Proceedings of 2003 IEEE Conference on Control Applications, 2003. CCA 2003.* Istanbul: IEEE, pp. 614–617.

Gómez Fuentes, J. V. (2016) *Simulation environment for advanced control development of a multiple hearth furnace*. Master thesis, Aalto University, Espoo. Available from : http://urn.fi/URN:NBN:fi:aalto-201605262236

Gómez Fuentes, J. V. and Jämsä-Jounela, S.-L. (2018a) Control Strategy For A Multiple Hearth Furnace, *IFAC-PapersOnLine*, 51 (21), pp. 189–194. DOI:10.1016/j.ifacol.2018.09.416.

Gómez Fuentes, J. V. and Jämsä-Jounela, S.-L. (2018b) Simplified Mechanistic Model of the Multiple Hearth Furnace for Control Development, *SNE Simulation Notes Europe*, 28 (3), pp. 97–100. DOI:10.11128/sne.28.sn.10426.

Gómez Fuentes, J. V., Jamsa-Jounela, S.-L., Moseley, D. and Skuse, T. (2019) Control strategy of a Multiple Hearth Furnace enhanced by machine learning algorithms, in: *2019 4th Conference on Control and Fault Tolerant Systems (SysTol)*. IEEE, pp. 250–256.

Gouveia, R., Lewis, D. G., Restrepo, A., Rodrigues, L. A. and Gedraite, R. (2009) Application of Model-Predictive Control to Multi-Hearth Nickel Reduction Roasters, *IFAC Proceedings Volumes*, 42 (23), pp. 292–296. DOI:10.3182/20091014-3-cl-4011.00053.

Heidarinejad, M., Liu, J. and Christofides, P. D. (2012) State-estimation-based economic model predictive control of nonlinear systems, *Systems & Control Letters*, 61 (9), pp. 926–935. DOI:10.1016/j.sysconle.2012.06.007.

Hodouin, D. (2011) Methods for automatic control, observation, and optimization in mineral processing plants, *Journal of Process Control*, 21 (2), pp. 211–225. DOI:10.1016/j.jprocont.2010.10.016.

Huang, B. and Kadali, R. (2008) Dynamic Modeling, Predictive Control and Performance Monitoring: A Data-driven Subspace Approach. 1st ed. London: Springer London, p. 227.

Huang, G.-B., Zhu, Q.-Y. and Siew, C.-K. (2006) Extreme learning machine: Theory and applications, *Neurocomputing*, 70 (1–3), pp. 489–501. DOI:10.1016/j.neucom.2005.12.126.

Jämsä-Jounela, S.-L., Laine, S. and Ruokonen, E. (1998) Ore Type based Expert Systems in Mineral Processing Plants, *Particle & Particle Systems Characterization*, 15 (4), pp. 200–207. DOI:10.1002/(SICI)1521-4117(199808)15:4<200::AID-PPSC200>3.0.CO;2-3.

Jämsä-Jounela, S. L., Gómez Fuentes, J. V., Hearle, J., Moseley, D. and Smirnov, A. (2018) Control strategy for a multiple hearth furnace in kaolin production, *Control Engineering Practice*, 81, pp. 18–27. DOI:10.1016/j.conengprac.2018.08.020.

Järvensivu, M., Saari, K. and Jämsä-Jounela, S.-L. (2001) Intelligent control system of an industrial lime kiln process, *Control Engineering Practice*, 9 (6), pp. 589–606. DOI:10.1016/S0967-0661(01)00017-X.

Jenkins, B. and Mullinger, P. (2008) Industrial and Process Furnaces: Principles, Design and Operations. 1st ed. Burlington: Elsevier, p. 505.

Juuso, E. K. and Leiviskä, K. (1992) Adaptive Expert Systems for Metallurgical Processes, *IFAC Proceedings Volumes*, 25 (17), pp. 119–124. DOI:10.1016/b978-0-08-041704-2.50027-3.

Karray, F. O. and De Silva, C. W. (2004) Soft Computing and Intelligent Systems Design, Theory, Tools and Applications. 1st ed. Edinburg Gate: Pearson Education Limited, p. 560.

Kim, N. K. and Srivastava, R. (1990) Simulation and control of an industrial calciner, *Industrial & Engineering Chemistry Research*, 29 (1), pp. 71–81. DOI:10.1021/ie00097a011.

Kohonen, T. (1982) Self-organized formation of topologically correct feature maps, *Biological Cybernetics*, 43 (1), pp. 59–69. DOI:10.1007/bf00337288.

Laine, S., Lappalainen, H. and Jämsä-Jounela, S.-L. (1995) On-line determination of ore type using cluster analysis and neural networks, *Minerals Engineering*, 8 (6), pp. 637–648. DOI:10.1016/0892-6875(95)00026-m.

le Roux, J. D., Olivier, L. E., Naidoo, M. A., Padhi, R. and Craig, I. K. (2016) Throughput and product quality control for a grinding mill circuit using non-linear MPC, *Journal of Process Control*, 42, pp. 35–50. DOI:10.1016/j.jprocont.2016.04.007.

Leiviskä, K. (2001) Soft Computing Applications in Mineral and Metal Industries, in: Leiviskä, K. (ed.) *Industrial Applications of Soft Computing*. Berlin: Physica-Verlag HD, pp. 23–34.

Murray, H. H. (2005) Clays, in: *Ullmann's Encyclopedia of Industrial Chemistry*. Weinheim: Wiley-VCH Verlag GmbH & Co, pp. 203–235.

Murray, H. H. and Kogel, J. E. (2005) Engineered clay products for the paper industry, *Applied Clay Science*, 29 (3–4), pp. 199–206. DOI:10.1016/j.clay.2004.12.005.

Olivier, L. E. and Craig, I. K. (2017) Lights-out process control — Analysis and framework, in: *2017 IEEE AFRICON*. IEEE, pp. 398–403.

Ptáček, P., Kubátová, D., Havlica, J., Brandštetr, J., Šoukal, F. and Opravil, T. (2010a) Isothermal kinetic analysis of the thermal decomposition of kaolinite: The thermogravimetric study, *Thermochimica Acta*, 501 (1–2), pp. 24–29. DOI:10.1016/j.tca.2009.12.018.

Ptáček, P., Kubátová, D., Havlica, J., Brandštetr, J., Šoukal, F. and Opravil, T. (2010b) The non-isothermal kinetic analysis of the thermal decomposition of kaolinite by thermogravimetric analysis, *Powder Technology*, 204 (2–3), pp. 222–227. DOI:10.1016/j.powtec.2010.08.004.

Ptáček, P., Opravil, T., Šoukal, F., Wasserbauer, J., Másilko, J. and Baráček, J. (2013) The influence of structure order on the kinetics of dehydroxylation of kaolinite, *Journal of the European Ceramic Society*, 33 (13–14), pp. 2793–2799. DOI:10.1016/j.jeurceramsoc.2013.04.033.

Ptáček, P., Šoukal, F., Opravil, T., Havlica, J. and Brandštetr, J. (2011) The kinetic analysis of the thermal decomposition of kaolinite by DTG technique, *Powder Technology*, 208 (1), pp. 20–25. DOI:10.1016/j.powtec.2010.11.035.

Ptáček, P., Šoukal, F., Opravil, T., Nosková, M., Havlica, J. and Brandštetr, J. (2010c) The kinetics of Al–Si spinel phase crystallization from calcined kaolin, *Journal of Solid State Chemistry*, 183 (11), pp. 2565–2569. DOI:10.1016/j.jssc.2010.08.030.

Ramírez, M., Haber, R., Peña, V. and Rodríguez, I. (2004) Fuzzy control of a multiple hearth furnace, *Computers in Industry*, 54 (1), pp. 105–113. DOI:10.1016/j.compind.2003.05.001.

Rawlings, J. B. and Amrit, R. (2009) Optimizing Process Economic Performance Using Model Predictive Control, in: Magni, L., Raimondo, D., and Allgöwer, F. (eds.) *Nonlinear Model Predictive Control*. Berlin: Springer Berlin Heidelberg, pp. 119–138.

Rawlings, J. B., Angeli, D. and Bates, C. N. (2012) Fundamentals of economic model predictive control, in: *2012 IEEE 51st IEEE Conference on Decision and Control (CDC)*. Maui: IEEE, pp. 3851–3861.

Rawlings, J. B., Bonne, D., Jorgensen, J. B., Venkat, A. N. and Jorgensen, S. B. (2008) Unreachable Setpoints in Model Predictive Control, *IEEE Transactions on Automatic Control*, 53 (9), pp. 2209–2215. DOI:10.1109/TAC.2008.928125.

Rawlings, J. B. and Mayne, D. Q. (2009) Model Predictive Control: Theory and Design 1st ed. Madison: Nob Hill Publishing, p. 767.

Richalet, J. (1993) Practique de la commande predictive. 1st ed. Paris: Hermes, p. 346.

Rossiter, J. A. (2004) Model-Based Predictive Control: A Practical Approach. 1st ed. Boca Raton: CRC Press, p. 344.

Salcedo Hernandez, J., Rivas-Perez, R. and Sotomayor Moriano, J. J. (2018) Design of a Generalized Predictive Controller for Temperature Control in a Cement Rotary Kiln, *IEEE Latin America Transactions*, 16 (4), pp. 1015–1021. DOI:10.1109/TLA.2018.8362131.

Shah, C., Choudhary, P., Deo, B., Malakar, P., Sahoo, S. K., Pothal, G. and Chattopadhyay, P. (2019) Conventional and AI Models for Operational Guidance and Control of Sponge Iron Rotary Kilns at TATA Sponge, in: Bansal, J., Das, K., Nagar, A., Deep, K., and Ojha, A. (eds.) *Advances in Intelligent Systems and Computing*. 1st ed. Singapore: Springer, pp. 461–469.

Simon, D. (2006) Optimal State Estimation: Kalman, H Infinity, and Nonlinear Approaches. 1st ed. Hoboken: John Wiley & Sons, Inc., p. 552.

Stadler, K. S., Poland, J. and Gallestey, E. (2011) Model predictive control of a rotary cement kiln, *Control Engineering Practice*, 19 (1), pp. 1–9. DOI:10.1016/j.conengprac.2010.08.004.

Thomas, R. E. (2010) *High Temperature Processing of Kaolinitic Materials*. PhD. Birmingham: University of Birmingham.

Thurlow, C. (2005) China Clay from Cornwall and Devon: An Illustrated Account of the Modern China Clay Industry. 4th ed. St Austell: Cornish Hillside Publications,.

Voglauer, B., Geyrhofer, W. and Jorgl, H. P. (2004) A model based control concept with knowledge based overhead control of a roasting process, in: *Proceedings of the 2004 American Control Conference*. Boston: IEEE, pp. 3581–3586.

Voglauer, B. H. and Jörgl, P. (2004) Dynamic Model of a Roast Process for Simulation and Control, *Mathematical and Computer Modelling of Dynamical Systems*, 10 (3–4), pp. 217–230. DOI:10.1080/13873950412331335234.

World Economic Forum (2017) Digital Transformation Initiative Mining and Metals Industry. Available from: http://reports.weforum.org/digital-transformation/wp-content/blogs.dir/94/mp/files/pages/files/wef-dti-mining-and-metals-white-paper.pdf

Yliniemi, L., Koskinen, J. and Leiviskä, K. (1998) Advanced Control of a Rotary Dryer, *IFAC Proceedings Volumes*, 31 (23), pp. 119–124. DOI:10.1016/S1474-6670(17)35865-2.

Zanovello, R. and Budman, H. (1999) Model predictive control with soft constraints with application to lime kiln control, *Computers & Chemical Engineering*, 23 (6), pp. 791–806. DOI:10.1016/S0098-1354(99)00008-3.

Zhu, Y. (2001) Multivariable System Identification For Process Control. 1st ed. New York: Elsevier Science, p. 372.

Ziegler, J. G. and Nichols, N. B. (1993) Optimum Settings for Automatic Controllers, *Journal of Dynamic Systems, Measurement, and Control*, 115 (2B), pp. 220–222. DOI:10.1115/1.2899060.